Electronic Structure and Physical Properties of Heusler Compounds for Thermoelectric and Spintronic Applications

Dissertation
zur Erlangung des Grades
"Doktor der Naturwissenschaften"
am Fachbereich Chemie, Pharmazie und Geowissenschaften
der Johannes Gutenberg-Universität Mainz

vorgelegt von
Siham Ouardi
geboren in Fes (Marokko)

Mainz, 2012

Tag der mündlichen Prüfung: 19. März 2012

Die vorliegende Arbeit wurde in der Zeit von Mai 2008 bis Dezember 2011 am Institut für Anorganische und Analytische Chemie im Fachbereich Chemie, Pharmazie und Geowissenschaften der Johannes Gutenberg-Universität, Mainz angefertigt.

Mainz, Februar 2012

Hiermit versichere ich, dass ich die vorliegende Dissertation selbstständig verfasst und keine anderen als die angegebenen Hilfsmittel benutzt habe. Alle der Literatur entnommenen Stellen sind als solche gekennzeichnet.

Mainz, Februar 2012

Contents

1 Abstract

This thesis focuses on the electronic structure and physical properties of Heusler compounds for spintronic and thermoelectric applications. It is organized in three parts. The first part (chapter 3) gives an introduction into the main phenomena related to the research and the second part (chapters 4 and 5) describes the details of the calculations and experiments. The main part (chapters 6-10) reports on the results and is divided into 5 chapters. Finally the results are summarized in chapter 11.

Chapter 6 reports on the electronic and crystal structure as well as the mechanical, magnetic, and transport properties of the polycrystalline Heusler compound Co_2MnGe. The crystalline structure was examined in detail by extended X-ray absorption fine-structure spectroscopy (EXAFS) and anomalous X-ray diffraction (aXRD). The low-temperature magnetic moment agrees well with the Slater-Pauling rule and indicates a half-metallic ferromagnetic state of the compound, as is predicted by ab-initio calculations. Transport measurements and hard X-ray photoelectron spectroscopy (HAXPES) were performed to explain the electronic structure of the compound. The vibrational and mechanical properties of the compound were calculated. The observed hardness values are consistent with a covalent-like bonding of Co_2MnGe.

A major part of the thesis deals with a systematical investigation of Heusler compounds for thermoelectric applications. There are a lot of studies published about *n*-type materials, but just a few studies have been reported on thermoelectric properties of p-type Heusler compounds. Therefore, this part focuses on the search for new p-type Heusler compounds with high thermoelectric efficiency. The chapter 7 reports about the optimization of NiTiSn based Heusler compounds for thermoelectric applications. First the substitutional series of $NiTi_{1-x}M_xSn$ (where M = Sc, V and $0 < x \leq 0.2$) was synthesized and investigated theoretically and experimentally with respect to electronic structure and transport properties. HAXPES was carried out to investigate the electronic structure. The carrier concentration and temperature dependence of electrical conductivity, Seebeck coefficient, and thermal conductivity were investigated in the range from 10 K to 300 K. The experimentally determined electronic structure and transport measurements agree well with the calculations. The results show the possibility to create *n*-type and *p*-type thermoelectrics within one type of Heusler compound. Accordingly, the effect of Ti substitution by Sc on the thermoelectric properties of the Heusler compounds $NiTi_{0.3-x}Sc_xZr_{0.35}Hf_{0.35}Sn$ (where $0 < x \leq 0.05$) was studied. The thermoelectric properties were investigated by measuring the electrical conductivity, Seebeck coefficient, and thermal conductivity. The pure compound $NiTi_{0.3}Zr_{0.35}Hf_{0.35}Sn$ showed *n*-type behavior, while under Sc substitution the system switched to *p*-type behavior. A maximum Seebeck coefficient of +230 μV/K (350 K) was obtained at 4% Sc substitution, which is one of the highest values for *p*-type thermoelectric compounds based on Heusler alloys up to now. HAXPES valence band measurements show massive *in gap* states for the parent compound. This proves that the electronic states close to the Fermi energy

play a key role for the behavior of the transport properties.

Chapter 8 describes a systematical investigation of the semiconducting Heusler compound CoTiSb and the solid solution series of $CoTi_{1-x}M_xSb$ (M = Sc, V and $0 \leq x \leq 0.2$) are reported. CoTiSb was synthesized and investigated theoretically and experimentally with respect to electronic structure, optical, mechanical, and vibrational properties. The optical properties were investigated the first time for this compound in a wide spectral range from 10 meV to 6.5 eV, and compared with ab-initio calculations. The optical spectra confirm the semiconducting nature of CoTiSb. The HAXPES valence band spectra confirm that the size of the band gap is in the order of 1 eV in agreement with the ab-initio calculations. The energies of the calculated optical phonons are in good agreement with the absorption observed in the infrared reflectivity measurement. The calculated phonon dispersion as well as elastic constants verify the mechanical stability of CoTiSb in the cubic $C1_b$ system. Furthermore, solid solution series of $CoTi_{1-x}M_xSb$ (M = Sc, V and $0 \leq x \leq 0.2$) were synthesized and investigated. The transport properties were calculated by all-electron ab-initio methods and compared to the measurements. The thermoelectric properties were investigated by measuring the temperature dependence of electrical resistivity, Seebeck coefficient, and thermal conductivity. Their values are in good agreement with the calculations.

Besides their well-known wide range of properties, it was recently shown that many of the heavy Heusler semiconductors with 1:1:1 composition and $C1_b$ structure exhibit a *zero band-gap* behavior and are *topological insulators* induced by their inverted band structure. In chapter 9, the electronic structure of the Heusler compounds PtYSb, PtLaBi and PtLuSb were investigated by bulk sensitive HAXPES. The measured valence band spectra are clearly resolved and in well agreement with the first-principles calculations of the electronic structure of the compounds. The experimental results give clear evidence for the zero band gap state. The linear behavior of the measured spectra close to ϵ_F proves bulk origin of the Dirac-cone type density. Furthermore, a systematic study on the optical and transport properties of the gapless PtYSb is presented. The optical properties were investigated in a wide spectral range from 10 meV to 6.5 eV, and compared to the ab-initio calculations. The optical spectra reveal an upper limit for the band gap of about 60 meV. The temperature dependence of thermal conductivity, electrical resistivity, Seebeck coefficient and Hall mobility were investigated. PtYSb exhibits very good thermoelectric properties with a high figure of merit ($ZT = 0.2$) and a Hall mobility μ_h of 300 cm^2/Vs at 350 K.

The last part of this thesis (chapter 11) describes the linear dichroism in angular-resolved photoemission from the valence band of the Heusler compounds $NiTi_{0.9}Sc_{0.1}Sn$ and NiMnSb. Within the framework of the DFG-JST project, an in-vacuum phase-retarder was developed at BL47XU in Spring8 (Japan) for the generation of linear or circularly polarized photons with synchrotron radiation. High resolution photoelectron spectroscopy was performed with an excitation energy of $h\nu = 7.938$ keV. The linear polarization of the photons was changed using an in-vacuum diamond phase retarder. The use of hard X-rays for excitation together with the high kinetic energies of the emitted electrons affords the advantage of making all surface effects negligible. The valence band spectra exhibit the typical structure expected from first-principles calculations of

the electronic structure of these compounds. Noticeable, linear dichroism is found in the valence band of both materials and this allows for a symmetry analysis of the contributing states. The differences in the spectra are found to be caused by symmetry dependent angular asymmetry parameters, and these occur even in polycrystalline samples without preferential crystallographic orientation.

Most parts of this thesis are published in scientific journals as listed in chapter 2.

2 List of Publications

1. S. Ouardi, B. Balke, A. Gloskovskii, G. H. Fecher, C. Felser, G. Schönhense, T. Ishikawa, T. Uemura, M. Yamamoto, H. Sukegawa, W. Wang, K. Inomata, Y. Yamashita, H.Yoshikawa, S. Ueda, K. Kobayashi
Hard X-ray photoelectron spectroscopy of buried Heusler compounds
J. Phys. D: Appl. Phys. 42 (2009) 084010.

2. S. Ouardi, A. Gloskovskii, B. Balke, C. A. Jenkins, J. Barth, G. H. Fecher, C. Felser, M. Gorgoi, M. Mertin, F. Schäfers, E. Ikenaga, K. Yang, K. Kobayashi, T. Kubota, M. Oogane, and Y. Ando
Electronic properties of Co_2MnSi thin films studied by hard X-ray photoelectron spectroscopy
J. Phys. D: Appl. Phys. 42 (2009) 084011.

3. S. Ouardi, G. H. Fecher, B. Balke, X. Kozina, G. Stryganyuk, C. Felser, S. Lowitzer, D. Ködderitzsch, H. Ebert, E. Ikenaga
Electronic transport properties of electron- and hole-doped semiconducting $C1_b$ Heusler compounds: $NiTi_{1-x}M_xSn$ (M=Sc, V)
Phys. Rev. B 82 (2010) 085108.

4. S. Ouardi, G. H. Fecher, B. Balke, M. Schwall, X. Kozina, G. Stryganyuk, C. Felser, E. Ikenaga, Y. Yamashita, S. Ueda, and K. Kobayashi
Thermoelectric properties and electronic structure of substituted Heusler compounds: $NiTi_{0.3-x}Sc_xZr_{0.35}Hf_{0.35}Sn$
Appl. Phys. Lett. 97 (2010) 252113.

5. S. Ouardi, S. Shekhar, G. H. Fecher, X. Kozina, G. Stryganyuk, C. Felser, S. Ueda, and K. Kobayashi
Electronic structure of Pt based topological Heusler compounds with $C1_b$ structure and zero band gap.
Appl. Phys. Lett. 98 (2011) 211901.

6. S. Ouardi, G. H. Fecher, X. Kozina, G. Stryganyuk, B. Balke, C. Felser, E. Ikenaga, T. Sugiyama, N. Kawamura, M. Suzuki, and K. Kobayashi
Symmetry of valence states of Heusler compounds explored by linear dichroism in hard-X-ray photoelectron spectroscopy
Phys. Rev. Lett. 107 (2011) 036402.

7. S. Ouardi, G. H. Fecher, B. Balke, A. Beleanu, X. Kozina, G. Stryganyuk, C. Felser, W. Kloss, H. Schrader, F. Bernardi, J. Morais, E. Ikenaga, Y. Yamashita, S. Ueda, and K. Kobayashi
Electronic and crystallographic structure, hard X-ray photoemission, and mechanical and transport properties of the half-metallic Heusler compound Co_2MnGe
Phys. Rev. B 84 (2011) 155122.

8. S. Ouardi, G. H. Fecher, C. Felser, C. G. F. Blum, D. Bombor, C. Hess, S. Wurmehl, B. Büchner, E. Ikenaga
Transport and thermal properties of single- and polycrystalline $NiZr_{0.5}Hf_{0.5}Sn$.
Appl. Phys. Lett. 99 (2011) 152112.

9. S. Ouardi, G. H. Fecher, C. Felser, J. Hamrle, K. Postava, J. Pistora
Transport and optical properties of the gapless Heusler compound PtYSb
Appl. Phys. Lett. 99 (2011) 211904.

10. G. H. Fecher, B. Balke, S. Ouardi, C. Felser, G. Schönhense, E. Ikenaga, J.-J. Kim, S. Ueda, and K. Kobayashi
High energy, high resolution photoelectron spectroscopy of $Co_2Mn_{1-x}Fe_xSi$
J. Phys. D: Appl. Phys. 40 (2007) 1576.

11. G. H. Fecher, B. Balke, A. Gloskowskii, S. Ouardi, C. Felser, T. Ishikawa, M-Yamamoto, Y. Yamashita, H. Yoshikawa, S. Ueda and K. Kobayashi
Detection of the valence band in buried Co_2MnSi tunnel junctions by means of photoemission spectroscopy
Appl. Phys. Lett. 92 (2008) 193513.

12. X. Kozina, S. Ouardi, B. Balke, G. Stryganyuk, G. H. Fecher, C. Felser, S. Ikeda, H. Ohno, E. Ikenaga
A nondestructive analysis of the B diffusion in Ta-FeCoB-MgO-FeCoB-Ta magnetic tunnel junctions by hard X-ray photoemission
Appl. Phys. Lett. 96 (2010) 072105.

13. J. Barth, G. H. Fecher, B. Balke, S. Ouardi, T. Graf, C. Felser, A. Shkabko, A. Weidenkaff, P. Klaer, H. J. Elmers, H. Yoshikawa, S. Ueda, S. and K. Kobayashi
Itinerant half-metallic ferromagnets Co_2TiZ (Z=Si, Ge, Sn): Ab initio calculations and measurement of the electronic structure and transport properties
Phys. Rev. B 81 (2010) 064404.

14. B. Balke, S. Ouardi, T. Graf, J. Barth, C. G. F. Blum, G. H. Fecher, A. Shkabko, A. Weidenkaff, and C. Felser
Seebeck coefficients of half-metallic ferromagnets
Solid State Commun. 150 (2010) 529.

15. Y. Gelbstein, N. Tal, A. Yarmek, Y. Rosenberg, M. P. Dariel, S. Ouardi, B. Balke, C. Felser, M. Köhne, M.
Thermoelectric properties of spark plasma sintered composites based on TiNiSn half-Heusler alloys
J. Mater. Res. 26 (2011) 1919.

16. C. G. F. Blum, S. Ouardi, G. H. Fecher, B. Balke, X. Kozina, G. Stryganyuk, C. Felser, S. Ueda, and K. Kobayashi, S. Wurmehl, and B. Büchner
Exploring the details of the martensite-austenite phase transition of the shape memory Heusler compound Mn_2NiGa by hard X-ray photoelectron spectroscopy, magnetic and transport measurements
Appl. Phys. Lett. 98 (2011) 252501.

17. X. Kozina, G. H. Fecher, G. Stryganyuk, S. Ouardi, B. Balke, C. Felser, G. Schönhense, E. Ikenaga, T. Sugiyama, N. Kawamura, M. Suzuki, T. Taira, T. Uemura,M. Yamamoto, H. Sukegawa, W. Wang, and K. Inomata
Magnetic dichroism in angle-resolved hard X-ray photoemission from buried layers
Phys. Rev. B 84 (2011) 054449.

18. X. Kozina, T. Jäger, S. Ouardi, A. Gloskovskii, G. Stryganyuk, G. Jakob, T. Sugiyama, E. Ikenaga, G. H. Fecher, C. Felser,
Electronic structure and symmetry of valence states of epitaxial $NiTiSn$ and $NiZr_{0.5}Hf_{0.5}Sn$ thin films by hard X-ray photoelectron spectroscopy.
Appl. Phys. Lett. 99 (2011) 221908.

19. V. Alijani, S. Ouardi, G. H. Fecher, J. Winterlik, S. S. Naghavi, X. Kozina, G. Stryganyuk, C. Felser, E. Ikenaga, Y. Yamashita, S. Ueda, and K. Kobayashi
Electronic, structural, and magnetic properties of the half-metallic ferromagnetic quaternary Heusler compounds CoFeMnZ (Z = Al, Ga, Si, Ge)
Phys. Rev. B 84 (2011) 224416.

20. G. Stryganyuk, X. Kozina, G. H. Fecher, S. Ouardi, S. Chadov, C. Felser, G. Schönhense, A. Oelsner, P. Bernhard, E. Ikenaga, T. Sugiyama, H. Sukegawa, Z. Wen, K. Inomata, and K. Kobayashi

Spin Polarimetry and Magnetic Dichroism on a buried magnetic layer using hard X-ray Photoelectron Spectroscopy
Jpn. J. Appl. Phys. 51 (2012) 016602.

21. A. Gloskovskii, C. A. Jenkins, S. Ouardi, B. Balke, G. H. Fecher, X. F. Dai, T. Gruhn, C. Felser, B. Johnson, I. Lauermann, R. Caballero, and C. A. Kaufmann
Hard X-ray photoelectron spectroscopy of chalcopyrite solar cell components
Appl. Phys. Lett. 100 (2012) 092108.

22. A. Gloskovskii, G. Stryganyuk, S. Ouardi, G. H. Fecher, C. Felser, J. Hamrle, J. Pistora, S. Bosu, Y. Sakuraba, K. Takanashi
Structure determination of thin CoFe films by anomalous X-ray diffraction
Appl. Phys. Lett. (2012) submitted.

23. M. Schwall, L. M. Schoop, S. Ouardi, B. Balke, C. Felser, P. Klaer, H. J. Elmers
Thermomagnetic properties improved by self-organized flower-like phase separation of ferromagnetic $Co_2Dy_{0.5}Mn_{0.5}Sn$
Adv. Funct. Mater., (2012) doi: 10.1002/adfm.201102792

3 Introduction

3.1 Intermetallic Heusler compounds

Since their discovery in 1903 [1], Heusler compounds attract continuously growing interest due to their multifarious properties for spintronic [2, 3, 4], optoelectronic [5], superconductivity [6], shape memory [7] and thermoelectric [8] applications. Heusler compounds are ternary intermetallic compounds consisting usually of two transition metals (T, T') and one main group element (M). They can be divided into two groups: Compounds with the chemical formula $T_2T'M$ having four fcc sublattices, and compounds with formula $TT'M$, consisting of three fcc sublattices (See Figure 3.1).

3.1.1 $T_2T'M$ Heusler compounds with $L2_1$ structure

Ordered Heusler compounds with 2:1:1 stoichiometry ($T_2T'M$) crystallize in the cubic face centered structure with Cu_2MnAl prototype ($L2_1$, space group $F\,m\overline{3}m$ (225)) [9], where T, T' and M atoms occupy the Wyckoff positions $8c$ ($\frac{1}{4}, \frac{1}{4}, \frac{1}{4}$), $4a$ (0,0,0) and $4b$ ($\frac{1}{2}, \frac{1}{2}, \frac{1}{2}$), respectively. Figure 3.1(c) shows as example the $L2_1$ structure of Co_2MnGe and its corresponding primitive cell with four atoms (figure 3.1(d)).

Some compounds (in most cases based on Mn_2), crystallize in the $AgLi_2Sb$ prototype structure (X, space group $F\,\overline{4}3m$ (216)), so that T atoms occupy Wyckoff positions $4a$ (0,0,0) and $4c$ ($\frac{1}{4}, \frac{1}{4}, \frac{1}{4}$), where T' and M are located on the nearest neighbor $4b$ ($\frac{1}{2}, \frac{1}{2}, \frac{1}{2}$) and $4d$ ($\frac{3}{4}, \frac{3}{4}, \frac{3}{4}$) positions, respectively. However, when the atoms T' and M are randomly located, the $L2_1$ crystal structure changes to $B2$, and when T, T' and M are disordered, it changes to $A2$. Those kinds of disorder have significant influence on the properties of the compounds.

Furthermore, research on half-metallic ferromagnetic (HMF) materials based on Heusler compounds has been rapidly growing since its prediction for NiMnSb in 1983 by de Groot and co-workers [2]. Several Heusler alloys crystallizing in the space groups $L2_1$ have been verified to be half-metallic by electronic band structure calculations [10]. Kübler and co-workers demonstrated that in many Heusler alloys the minority spin density of states (DOS) exhibits a band gap at the Fermi energy while the majority spins are responsible for the metallic properties. Those compounds are considered to be useful candidates for tunneling magnetoresistance (TMR) devices, because the magnetoresistance (MR) is expected to be large if the conduction electron spin is 100% polarized. This conduction electron spin can be possibly injected into a semiconductor, when the materials are epitaxially grown on the semiconductor surface.

Nowadays, Co_2 based Heusler compounds are successfully used as ferromagnetic electrodes providing a spin polarized electrical current in TMR junctions [11, 12, 13]. To produce high performance spintronic devices with Heusler thin films as ferromagnetic electrodes, it is necessary to clarify the dependence of the magnetoresistive characteristics on the disorder and stoichiometry of the Heusler film electrode and its impact

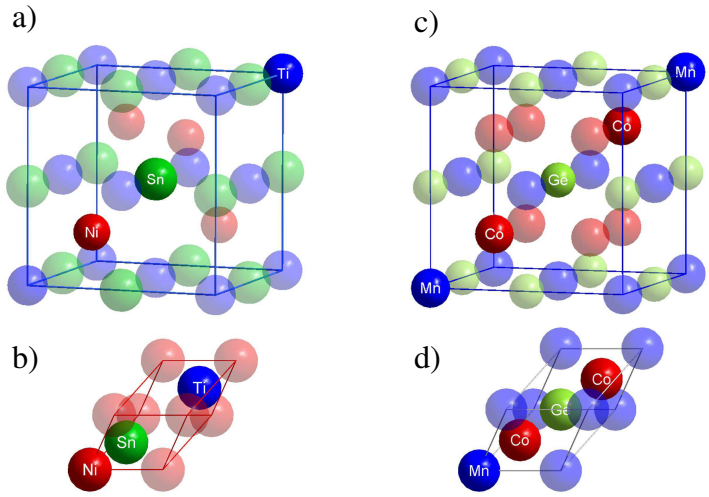

Figure 3.1: Comparison of the $C1_b$ (T_d) (a) and $L2_1$ (O_h) (c) structures of Heusler compounds and their primitive cells (b) and (d) respectively. Note the missing center of inversion in the $C1_b$ structure with T_d symmetry.

on the selection of materials for TMR devices. Structural and magnetic properties of Co_2MnSi were reported for films and single crystals [14, 15] and the compound was suggested to be suitable for magnetic tunnel junctions (MTJs) [11, 16, 17]. A high TMR ratio of 179% at room temperature (RT) and 683% at 4.2 K was revealed by Ishikawa and coworkers [11]. An appropriate alternative to Co_2MnSi is the isovalent Co_2MnGe with 29 valence electrons in the primitive cell. This ternary compound is of interest for spintronic applications because it combines high Curie temperature (905 K) [18], high magnetic moment (5 μ_B) [19], and coherent growth on top of semiconductors [20, 21].

Furthermore, partially substitution of one of the elements in the ternary Heusler $T_2T'M$ can be used to design new materials with predictable properties [3, 22], such as tuning the Fermi energy in to the middle of the minority band gap [23]. The partially substitution of the elements in $T_2T'M$ leads to substitutional quaternary alloys of the type $T_2T'_{1-x}T''_xM$ or $T_2T'M_{1-x}M'_x$. The Co_2 based Heusler alloys of those types have been previously investigated theoretically and experimentally. The quaternary alloy $Co_2Cr_{0.6}Fe_{0.4}Al$ has attracted emersed interest as potential material for magnetoelectronics, due to the large MR [24, 25]. The band structure calculations confirmed the halfmetallic state of this compound in the ordered $L2_1$ structure [3, 22, 24]. Recently, several groups developed fully epitaxial magnetic tunnel junctions (MTJs) based on $Co_2Cr_{0.6}Fe_{0.4}Al$ as a lower electrode and a MgO tunnel barrier [26, 27, 28]. However, a disorder of the structure results in a strongly reduced magnetic moment as well as a loss of the half-metallic character [29, 30].

3.1.2 $TT'M$ Heusler compounds with C1$_b$ structure

The Heusler compounds with a 1:1:1 composition crystallize in the cubic MgAgAs-type structure ($C1_b$, space group $F\,\overline{4}3m$ (216)) [31, 32]. Figure 3.1(a) and 3.1(b) shows the $C1_b$ structure of the Heusler compound NiTiSn and its primitive cell, respectively. The $C1_b$ structure can be derived from $L2_1$, when replacing one of the T atom in the tetrahedral site by a vacancy V_c (compare the primitive cells in figure 3.1(b) and 3.1(d)). Note the result for T_2M is the C_1 (CaF_2) structure when removing the T' atom.

The properties of these $TT'M$ compounds depend strongly on the valence electron concentration (VEC) or number of valence electrons (N_v) in the primitive cell, which determine the band structure and accordingly the physical properties of the compounds [33, 34]. Compounds with $N_v = 21$, or 22 like NiMnSb were suggested to be halfmetallic ferromagnets [35]. Whereas compounds with $N_v = 20$ are not stable due to the localization of the Fermi level at states of the antibonding region [34].

In particular, compounds with $N_v = 18$ exhibit a closed shell type behavior with filled bands (a_1, t_1, e, t_2) and therefore are found to be semimetals or semiconductors [33]. A schematically illustration of the band structure of semimetal and semiconductor are shown in figure 3.2(b) and 3.2(d). From experimental studies and band structure calculations it is concluded that numerous 18 VEC-Heusler systems based on *light* transition metals (likewise CoTiSb or NiTiSn) exhibit semiconducting properties, with narrow band gaps in the density of states (DOS) at the Fermi energy ϵ_F [33]. This class of compounds was reported to exhibit excellent thermoelectric properties [36]. Previous studies of the electronic structure [37] of narrow band gap Heusler compounds showed that the observed *in gap* states close to ϵ_F play a key role on the behavior of the transport properties of the compounds.

Furthermore, many of the Heusler compounds with $C1_b$ structure containing *heavy* metals (Au, Pt, Sb, or Bi) and a lanthanide element exhibit a *zero band gap* state, they are so called gapless semiconductors. That is, the band gap is closed through the touching of the valence and conduction bands at ϵ_F (See figure 3.2(c)). The *zero band gap* state may appear for indirect (equal energies of valence and conduction band for example at Γ and X) or direct band gaps [38]. According to the earlier electronic structure computations [39], several materials with a *zero direct gap* at Γ were predicted to be topological insulators. These are insulators with a bulk band gap generated by strong spinorbit coupling and topologically protected metallic surface states composed of an odd number of Dirac fermions. Based on topologically protected electronic surface states, this class of materials is supposed to open up innovative directions for future technological applications in spintronics and quantum computing. The non trivial topology of the electronic band structures is characterized by band inversion at the Γ point in the Brillouin zone [40]. The peculiarities of the topological surface states are originating from the inversion of bulk bands, therefore it is needed to explain the bulk electronic structure what was done in this work by the use of hard X-ray photoelectron spectroscopy (HAXPES) as bulk sensitive method.

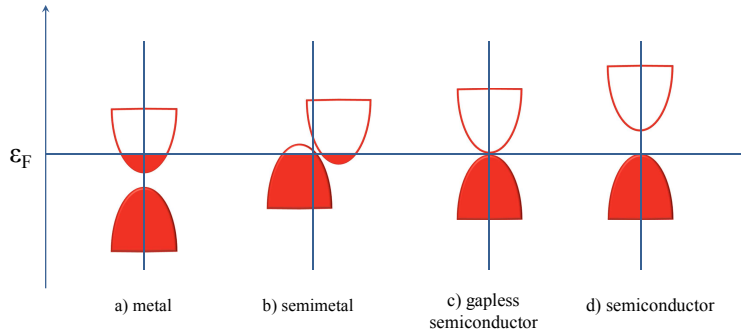

Figure 3.2: Schematic illustration of electronic structure from metal to semiconductor. (a) metal, (b) semimetal, (c) gapless semiconductor, and (d) semiconductor.

3.2 Thermoelectric properties

The limitations of energy resources like depletion of fossil fuel, whereas a demand for global energy is growing, has resulted in an extensive research on novel renewable energies. In recent years, thermoelectric (TE) material have achieved potential role in the realization of environmentally friendly technology due to conversion of the waste heat in electrical energy and reduction of the greenhouse gas emissions.

Thermoelectric effects provide a direct conversion of thermal energy (waste heat) into electrical energy. The TE materials can be implemented into refrigeration devices for cooling applications as well as into power generation devices.

3.2.1 Seebeck and Peltier effect

By applying a temperature gradient ΔT in a TE couple, consisting of n-type and p-type materials, the charge carriers diffuse from the hot (T_h) to the cold (T_c) side, producing an electric potential ΔV. This is known as the Seebeck effect (Figure 3.3 b)). The ratio of the produced voltage to the temperature difference is the thermopower or Seebeck coefficient:

$$S = \frac{\Delta V}{\Delta T} \tag{3.1}$$

In materials where dominant charge carriers are holes (p-type), the Seebeck coefficient has a positive sign, while those dominated by electrons (n-type) have negative Seebeck coefficients.

Inversely, when an electric current is passed through a TE couple, the carriers tend to

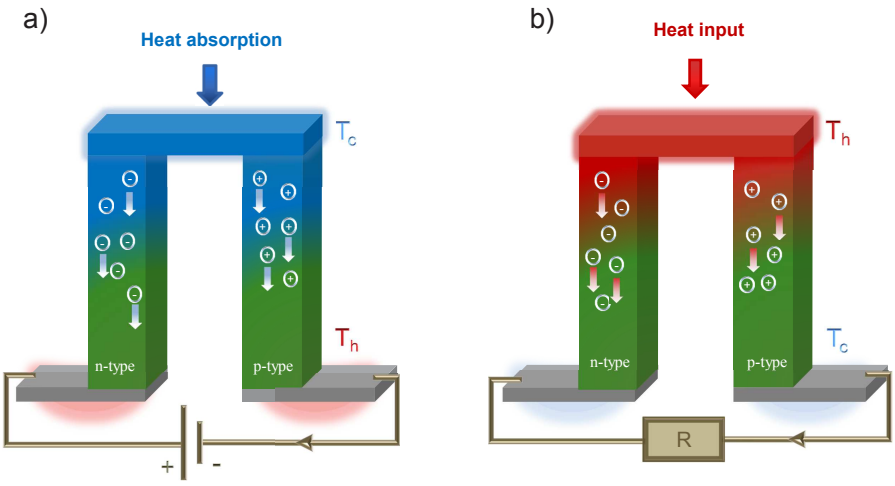

Figure 3.3: Schematic illustration of a) thermoelectric refrigerator and b) thermoelectric generator.

equilibrium by absorbing heat on the T_c-site and releasing it at the $44T_h$-site, this TE phenomenon is known as the Peltier effect (Figure 3.3 a)).

3.2.2 Thermal conductivity

The generated temperature gradient ∇T in a TE material is related to the applied heat flux Q by a thermal transport coefficient. This coefficient is the thermal conductivity κ:

$$\kappa = -\frac{\nabla T}{Q} \tag{3.2}$$

In a crystalline solid, the thermal conductivity κ can be defined as the sum of the electronic (κ_e) and the lattice (κ_L) thermal conductivities [41]:

$$\kappa = \kappa_e + \kappa_L \tag{3.3}$$

The electronic contribution κ_e depends on the carrier concentration and is directly related to the electrical conductivity σ through the Wiedemann-Franz law:

$$\kappa_e = L \times \sigma \times T \tag{3.4}$$

where L is the Lorenz number.

3.2.3 Searching for high performance thermoelectric materials

The efficiency of TE devices is determined by the thermoelectric figure of merit ZT:

$$ZT = \frac{S^2 \times \sigma}{\kappa} \times T \tag{3.5}$$

where, $PF = S^2 \times \sigma$ is the power factor.

In order to reach the best performance of thermoelectric materials, the figure of merit ZT has to be enhanced by maximizing the power factor PF and minimizing the thermal conductivity κ. However, these three parameters (S, σ, and κ) depend on each other. Therefore, the challenge to create TE materials with high ZT is to achieve simultaneously high Seebeck coefficient, high electrical conductivity and low thermal conductivity in the same device.

The efficiency of a TE device is determined by the materials used to build the device [36]. Presently, the world market for TE devices is still small, caused by their low efficiencies, which is limited by high cost (e.g.: SiGe alloys), significant toxicity (e.g.: Bismuth or Thallium chalcogenides), and stability at the operation temperatures. The $C1_b$ Heusler compounds were demonstrated to achieve an excellent potential as materials for high temperature power generation [42]. Advantages are their environmentally friendly constituents, low cost, easy synthesis, and chemical stability (high melting points) [43]. Recently, numerous Heusler alloys have been investigated focusing on their high-temperature thermoelectric properties.

Likewise the $T_2T'M$ alloys, the properties of $TT'M$ Heusler compounds can be design by partial substitution of one or more atoms. Actually, the substitution of the transition metals ($T_{1-x}T''_xT'M$ or $TT'_{1-x}T''M$) as well as of the main group element ($TT'M_{1-x}M'_x$) were investigated. Two kind of substitution can be created. The isoelectronic substitution generate a impurity scattering, due to the scattering of electrons and phonons at the substituted atoms that act as impurities even though they occupy regular lattice sites. Substitution by atoms with less, or more valence electrons, than the substituted atom results in hole, or electron doping, respectively. In order to achieve the best performance of thermoelectric modules the n- and p-type materials should be designed to exhibit similar chemical and physical properties [41, 44, 45]. The latter requirement can easily be fulfilled if using element substitution in order to tune the electronic properties to the desired values in a controlled way.

In recent years, several work has been focused on reduction of the lattice thermal conductivity κ_L by phonon scattering at grain boundaries due to grain size for nanostructuring [46], interface scattering in thin films or multilayer systems, or solid-solution alloying [8, 47, 48]. On the other hand, there is a challenge, how to increase the Seebeck coefficient S without depressing the electrical conductivity σ. Usually σ and S depend strongly on the density of states DOS close to the Fermi level (ϵ_F) [49]. Due to the low carrier concentration, S exhibits a high value in semiconductors, that have, indeed, always a low electrical conductivity σ. Those two parameters have to be optimized by design of the band-gap size of the compounds. Miyamoto and coworkers observed "in gap" states close to the (ϵ_F) for Heusler compounds, and suggested that these could be

the key to control the thermoelectric properties [50]. In this thesis the "in gap" states of some Heusler compounds were investigated and there influence on the transport properties of the compounds was systematically studied.

3.3 Photoelectron Spectroscopy (PES)

Since the first experiment performed by Kai Siegbahn an co-worker in the 1950 (Nobel prize in 1981), photoelectron spectroscopy (PES) has evolved into the most relevant, powerful, and nondestructive method for the investigation of atoms, molecules and solids. PES is of great importance in many fields of research because of its numerous advantageous properties. Valence band PES approves detailed illustration of the electronic structure, whereas chemical information, like composition or bonding can be obtained by core level PES.

X-ray photoelectron spectroscopy is based on the photoelectric effect. When a solid is radiated with light of energy $h\nu$, electrons can be photoexcited if the energy of the excited electron is high enough to overcome a surface potential Φ (Einstein Nobel prize 1921 [51]). Result is an ejection of core or valence electron with kinetic energy E_{Kin}. The Einstein equation describes the energy balance of a photoemission process:

$$E_{Kin} = h\nu - E_{Bin} - \Phi, \tag{3.6}$$

where E_{Kin} is the kinetic energy of the photoelectron, h is the Plank s constant, ν is the frequency of the incident radiation, E_{Bin} the binding energy of the photoelectron with respect to the Fermi level of the sample and Φ is the work function. The photoemission process is usually described in a three step model. The first step is the photoexitation, resulting in an excitations of electrons from an initial (ground) state to a final (excited) state. The second step is the transport of the electron to the surface. The electron escape depth is limited by inelastic scattering (see equation 3.7). The last step is the escape of the electron into vacuum. This require the electron to overcome of surface potential barrier. While the kinetic energy of the photoelectron is proportional to the frequency of the incident radiation ν. The kinetic energies E_{Kin} of the emitted electrons depend on their binding energies E_{Bin}. E_{Bin} is not only element specific but contains also chemical information about the atoms. Because the energy levels of the core electrons depend on the chemical state of the atoms, like different oxidation states, lattice sites or molecular environments. The last is known as a *chemical shift*.

In the contemporary various types of soft laboratory light sources are used for excitation. Photons of low energy (20 - 100 eV) in the ultraviolet photoelectron Spectroscopy (UPS), or medium energies in X-ray photoelectron spectroscopy (XPS)(Mg K_α or Al K_α with an excitation energy of 1.254 keV or 1.486 keV, respectively,) are commonly used to identify the chemical composition. Unfortunately, the applications of those laboratory sources are limited to the study of surfaces due to the rather small escape depth of the photoelectrons. In contrast, the use of hard X-rays for excitation results in the emission of electrons having high kinetic energies, in turn leading to a high probing depth because of the increased electron mean free path. The first high resolution hard X-ray

photoemission spectroscopy experiments using synchrotron radiation were performed by Lindau et al [52] in 1974, who used X-rays from a bending magnet at SPEAR (Stanford Synchrotron Radiation Laboratory) to measure the intrinsic linewidth of the Au $4f$ core levels with high energy resolution. The observed peak count rate was very low, thus no further trials aiming at high resolution hard X-ray spectroscopy for practical studies were attempted until the first report of HAXPES using a third-generation undulator X-ray source in 2003 [53].

3.3.1 Hard X-ray photoelectron spectroscopy (HAXPES)

HAXPES has emerged as a powerful tool to investigate the bulk electronic structure of materials in a variety of applied fields such as chemistry, physics, materials science and industrial applications [54]. The use of high-brilliance high-flux X-rays from the third-generation synchrotron radiation sources results in emission of electrons having high kinetic energies, in turn leading to a high probing depth because of the increased electron mean free path [55]. Recently, several studies using high-resolution HAXPES have been realized. The electronic structure of solids like valence transitions in bulk systems [56, 57] as well as multilayer systems [55] and the valence band of buried thin films [58] have been investigated. The valence transitions of several bulk systems were successfully investigated by means of HAXPES [59, 60, 61, 7] and very recently, the polarization dependence of the emission from Au and Ag samples was reported [62].

HAXPES is the method of choice to perform bulk sensitive photoemission spectroscopy (at excitation energies of about 8 keV an escape depth greater than 90 Å is attained) on correlated systems in thin films, multilayer and devices because it overcomes the shortcomings of a low electron mean free path in solids. At high kinetic energies of the electrons as used in HAXPES the valence band as well as core level can be investigated spectroscopically with real bulk sensitivity. In standing wave methods [63, 64] this is used to distinguish the valence band signals emerging from bulk or interfaces. The wide energy range easily allows a chemical analysis and moreover the details of the core level spectra allow to investigate satellites that appear in magnetic and correlated systems. Magnetic dichroism in the angular distribution (MDAD) can be excited by any kind of photon polarization and is accessible by laboratory sources. It makes use of the break of symmetry implied by the magnetization of the sample or by orientation of correlated electron states.

At the present time, the high energy excitation and analysis of electrons has become easily feasible due to the development of high intensity sources (insertion devices at synchrotron facilities) and multi-channel electron detection. Thus, HAXPES was recently introduced by several groups (for a complete overview see [65, 54] and references therein) as a bulk sensitive probe of the electronic structure of complex materials. The resolution of HAXPES with down to below 50 meV photon band-width (BL47XU and BL29XU at SPring-8) is competitive to low energy solid state photoemission that is often governed by life time broadening. Even higher resolution (20 meV) seems to be possible after recent improvements concerning the intensity at the SPring-8 beamlines and using a micro/nano focused beam [54].

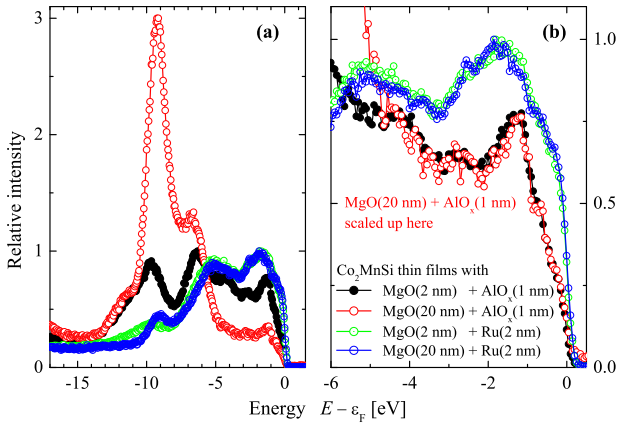

Figure 3.4: High energy valence band spectra of Co_2MnSi / MgO / AlO_x and Co_2MnSi / MgO / Ru.
Shown is the comparison between Co_2MnSi thin films with 2 nm and 20 nm MgO on top of the Co_2MnSi and capped with 1 nm AlO_x or 2 nm Ru. Panel (a) shows the complete valence band while panel (b) shows an enlarged view close to the Fermi energy. Note that in (b) the spectra of the Co_2MnSi thin film with 20 nm MgO on top of it and capped with 1 nm AlO_x is scaled up for better comparison.

Several investigations of bulk Heusler compounds by HAXPES were performed. High resolution photoelectron spectroscopy measurements of the valence band of polycrystalline $Co_2Mn_{1-x}Fe_xSi$ ($x = 0, 0.5, 1$), excited by photons having an energy of approximately 8 keV, was reported in [66, 67]. It was shown that the high energy spectra indicate the bulk electronic structure better than low energy XPS spectra. High resolution measurements of the valence band close to the Fermi energy indicate the existence of a gap in the minority states for all three alloys. Further, HAXPES investigations were also performed on thin films fabricated from Heusler compounds. High energy photoelectron spectroscopy from the valence band of buried Heusler thin films (Co_2MnSi and $Co_2FeAl_{0.5}Si_{0.5}$) excited by photons of about 6 keV energy was carried out and reported in [58, 68]. The measurements were performed on thin films covered by MgO and SiO_x with different thickness from 1 nm to 20 nm of the insulating layer and additional AlO_x or Ru protective layers. In case of AlO_x layer, the insulating layer does not affect the high energy spectra of the Heusler compound close to ϵ_F as shown in Figure 3.4. Whereas by Ru protection the emission from the O states is completely suppressed and the structure of the valence band close to ϵ_F (see figure 3.4(b)) is dominated by the emission from the Ru layer. The high resolution measurements of the valence band close to ϵ_F indicated a very large electron mean free path of the electrons through the insulating layer. The spectra of the buried thin films agreed well with previous measurements from bulk samples.

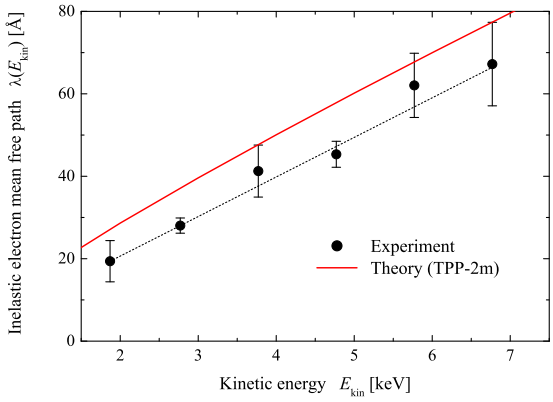

Figure 3.5: Inelastic mean free path.
The electron mean free path in Co_2MnSi for electrons with kinetic energies from 2.25 keV to 7.0 keV. The calculations are for the TPP-2m equation (Tanuma-Powell-Penn [70]).

The electron inelastic mean free path was experimentally determined for Co_2MnSi in a wide energy range [69]. As expected for materials with unfilled *d*-shells, its value is slightly smaller than the calculated one (see Figure 3.5). The buried Co_2MnSi thin film resembles the valence band of the bulk sample that confirms its promise as an electrode for spintronic devices. The electronic structure of the buried thin films at 20 K does not differ from the one measured at 300 K. Accounting for the bulk sensitivity of HAXPES, this illustrates that the electronic structure of the thin Co_2MnSi film itself does not depend on the temperature for $T \leq 300$ K. This fact rules out the possibility that the temperature dependence of the TMR is related to the changes in the bulk electronic structure of the electrodes. The observed temperature dependence of the TMR has to be directly related to the properties of the Co_2MnSi-MgO interface.

3.3.2 Cross sections and inelastic mean free path at high energies.

The high bulk sensitivity is one of the most important properties of HAXPES. The bulk sensitivity is based on the large electron mean free path at high kinetic energies resulting in a large escape depth of the electrons. A reduction of the photon intensity can be safely neglected because the mean free path of X-rays is by orders of magnitude larger than the one of the electrons.

Figure 3.6 illustrates the general behavior of the electron mean free path with variation of the kinetic energy of the photoelectrons. The shape of this dependence is rather independent of the material wherefore it became named *universal curve*. A closer inspection reveals that the mean free path, indeed, is material dependent (see [70]). From Figure 3.6 it is clear that HAXPES covers the widest range of spectroscopic possibilities. Ultraviolet photoelectron spectroscopy (UPS) covers the energy region of the valence

band but is most surface sensitive. The escape depth becomes larger for XPS using soft X-rays or regular laboratory sources (Al K_α, Mg K_α) but is still beyond true bulk sensitivity. The role of threshold or two-photon photoemission (2-PPE) with very low kinetic energies (< 5 eV) is ambiguous. On the one hand one expects a high escape depth whereas on the other hand the spectroscopic information is limited to the Fermi energy and work function, with the latter being again a typical surface property.

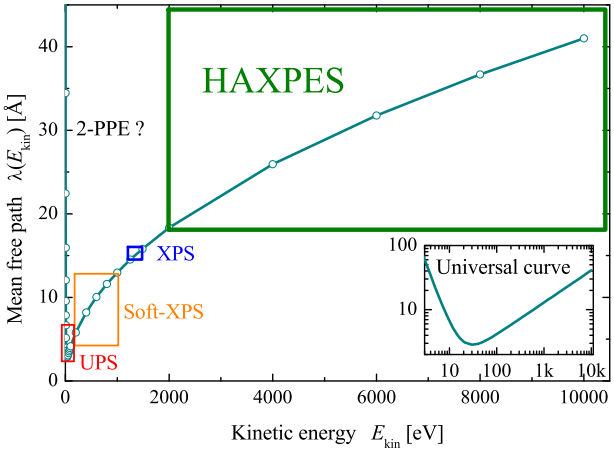

Figure 3.6: *Universal curve* of the electron mean free path $\lambda(E)$. Shown is the variation of the inelastic mean free path as function of the photoelectron kinetic energy. The inset shows $\lambda(E)$ on the often used log-log scale. Typical ranges of different methods are marked by boxes.

The effective probing depth $z_{\text{eff}} = l\cos(\theta)$ is given by the path l of the electrons through the solid with θ being the angle between the direction of electron emission and the surface normal. The effect of varying θ is a high surface sensitivity at large emission angles, rather independent on energy. Therefore, normal emission ($\theta = 0$, $z = l$) will be assumed in the following. The intensity of the electrons passing through a layer of thickness z is reduced according to a exponential law:

$$I(z) = I_0\, e^{-\frac{z}{\lambda(E)}}, \tag{3.7}$$

where $\lambda(E)$ is the energy (E) dependent mean free path. The effect of intensity reduction is illustrated in Figure 3.7 for the example of Co_2MnGe. It is seen that the intensity drops down very fast at low energies. At 50 eV not much more than the topmost cell is probed by the electrons. The situation changes drastically at 8 keV, even after 20 cells the intensity is reduced by only $1/e \approx 0.435$. This also means that still more than 50% of the signal emerge from deeper layers.

From Figure 3.7 and Equation 3.7 it is also expected that intensity is gained when using high kinetic energies as the integrated intensity normalized to the lattice parameter a

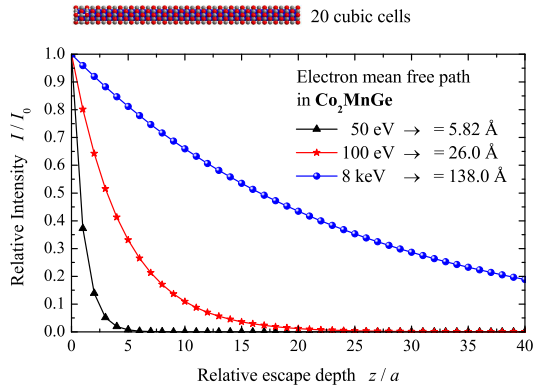

Figure 3.7: Electron mean free path in Co_2MnGe. Shown is the intensity as function of the number of cubic cells ($a = 5.7477$ Å) for different kinetic energies.

$$I_{\text{eff}} = \frac{1}{a}\int_0^\infty I(E,z)dz = I_0\frac{\lambda(E)}{a} \tag{3.8}$$

increases with increasing electron mean free path. Unfortunately, this is not the complete truth. Reason is the decrease of the photoelectron cross sections with increasing photon energy. The partial cross sections (σ_{nl}) of the valence states of the elements contributing in Co_2MnGe are shown in Figure 3.8. The cross sections for core level (not shown here) are reduced in a similar way. A strong reduction of σ_{nl} by up to three orders of magnitude between 1 keV and 8 keV is obtained. Further, it is obvious that the cross sections for excitation of d states decrease faster than for s states. The effective cross section ($\sigma_{\text{eff}} = \sigma_{nl}\lambda/a$) respecting the gain of intensity by the increasing mean free path is shown in Figure 3.8(d) for the states contributing most to the valence band of Co_2MnGe.

3.3.3 Linear dichroism in the angular distribution (LDAD)

The linear dichroism in the angular distribution (LDAD) of photoelectrons has attracted considerable interest as a powerful probe to study the symmetry, orientation, and alignment phenomena in photoionization [71, 72, 73]. The prerequisites for this effect are the orientation of the photons and the alignment of the electronic states [74]. The first is realized by the linear polarization of the photons whereas the second might be produced by the alignment of the molecular axes or by the symmetry of the bands in a solid. The main difference between linear and circular dichroism in the angular distribution is that the former does not require a chirality or magnetization of the investigated system because the electric field vector of linearly polarized photons is a real vector whereas the helicity of circularly polarized photons is a pseudovector [75].

Angle-resolved photoelectron spectra excited by linearly polarized photons indicated that the intensities of emissions from chemisorbed systems exhibited strong variations [76].

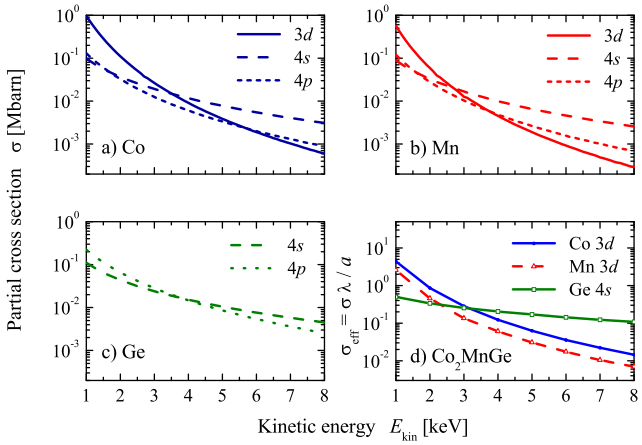

Figure 3.8: Partial cross sections of Co_2MnGe.
Shown are the cross sections of the valence states of Co (a), Mn (b), and Ge (c). Panel (d) shows the effective cross section respecting the intensity gain by the increased mean free path for the states that contributes most to the valence bands of Co_2MnGe.

Later, a dichroism with linearly polarized light was predicted, where the electric field vector is aligned at ±45° with respect to the plane of incidence [75]. Subsequently, many theoretical [77] and experimental studies of the LDAD have been carried out. The basic theory of LDAD was first developed for gas-phase molecules and molecules adsorbed on surfaces [78]. LDAD measurements have been actively used to study different adsorbates as well as surfaces [60, 73]. High asymmetries were reported for the valence orbitals of CO/Pt(111) [79]. The nonmagnetic and nonchiral system 1T-TaS_2 is an example of LDAD from solids [72].

Thus far, most studies dealing with LDAD have been based on soft radiation in the range from the vacuum ultraviolet region (UPS) to the soft X-ray region (XPS), resulting in a very limited probing depth that is suitable only for the examination of surface effects. In contrast, the use of hard X-rays for excitation results in the emission of electrons having high kinetic energies, in turn leading to a high probing depth because of the increased electron mean free path.

In the following, a theoretical and experimental background on the linear dichroism in the angular distribution (LDAD) is given at the example of Au(111):

Dipole approximation

The polarization-dependent spectra can be most easily analyzed for direct emission by neglecting all final state effects in the first step (for example: electron diffraction [80]). In the dipole approximation, respecting only E_1 transitions, the observed intensity ($I^{E_1} \propto \frac{d\sigma}{d\Omega}$) depends on the partial cross section (σ_κ) and the angular asymmetry parameter (β_κ) of the photoexcited states. Here, κ assigns a complete set of quantum numbers

describing the initial state. For atomic-like states in a single electron description, these are $\kappa = n, l$ with main quantum number n and orbital angular momentum l in the non relativistic and $\kappa = n, l, j$ with total angular momentum j in the relativistic case. In the case of linearly polarized photons, the angular dependence of the intensity in the dipole approximation is given as follows [81]:

$$I_\kappa^{E_1}(\theta) = \sigma_\kappa \left[1 + \beta_\kappa P_2(\theta)\right], \tag{3.9}$$

where $P_2(\theta) = (3\cos^2\theta - 1)/2$ is the second Legendre polynomial and θ is measured with respect to the electric field vector. The requirement that the intensity has to be positive restricts the angular parameter to the range $-1 \leq \beta \leq 2$. Both parameters, σ_κ and β_κ, depend on the kinetic energy of the emitted electrons.

In the derivation of Equation (3.9) it is assumed that the atoms or molecules have no preferred orientation or alignment, that is their axes are randomly distributed in space. This applies also to polycrystalline solids when the size of the photon beam is larger than the grains of the sample. For unpolarized or circularly polarized light a similar equation holds with θ_q measured with respect to the photon propagation ($I_\kappa^{E1,unpol}(\theta_q) = \sigma_\kappa \left[1 - \beta_\kappa P_2(\theta_q)/2\right]$).

A dichroism in the angular distribution of the photoelectrons is observed when comparing the intensities taken with two mutually perpendicular orientations of the photon polarization. Switching for example the circular polarization (S_3 component of the Stooke's vector [82]) from σ^+ to σ^- results in the circular dichroism in the angular distribution of photoelectrons (CDAD) [83, 84, 85]. A linear dichroism is observed if switching either the S_1 component from p to s or the $S2$-component of the Stooke's vector. The latter case is described in [75]. The present work deals with the case of linear dichroism in the angular distribution (LDAD) of the photoelectrons that appears by rotating the photon polarization between p and s. In equation (3.9), the angular distribution is given with respect to the polarization vector in the photon frame, therefore the co-ordinate frame of the emitted electrons with respect to the sample orientation has to be rewritten to the photon frame. If one changes now the direction of the polarization by $\pi/2 = 90°$ one has to replace the Cosine by a Sine. The difference between both angular distributions is the LDAD:

$$\begin{aligned} I_\kappa^{LDAD} &= I_\kappa^p - I_\kappa^s \\ &= \sigma_\kappa \cdot \frac{3\beta_\kappa}{2} \cos(2\Theta_\epsilon) \sin^2(\Phi_\epsilon). \end{aligned} \tag{3.10}$$

The term $\sin^2(\Phi_\epsilon)$ arises from the fact that the complete angular distribution is rotated by 90° rather than only shifted by Θ. Φ_ϵ is measured with respect to the plane spanned by the initial electric field and the photon propagation vector. As far as no assumption was made on the initial orientation of the linear polarization vector, this result is independent of the Stookes-vector components. The LDAD from filled shells that have a spherical distribution will always vary with $2\Theta_\epsilon$ independent on the orbital angular momentum of the initial state. The difference between S_1 or S_2 polarization components of the

Stooke's vector is simply, that the LDAD pattern is rotated by 45°. The absolute value of this distribution always looks like a fourfold clover leave in the plane perpendicular to the photon beam. The intensity distributions are illustrated in Figure 3.9 for a view along the direction of the photon beam and the borderline cases of β.

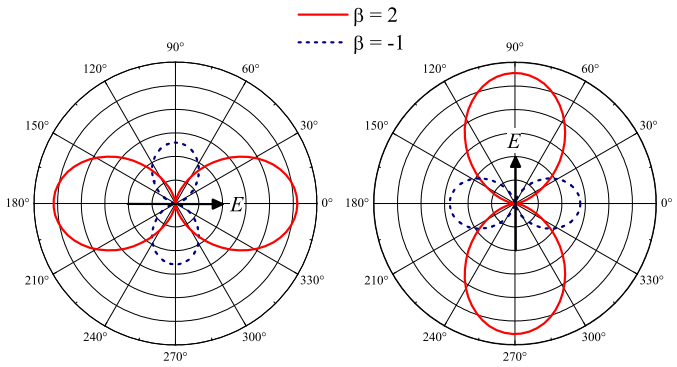

Figure 3.9: Angular distribution of the photoelectrons.
Shown is the angular dependent part $[1 + \beta P_2(\theta)]$ for $\beta = -1$ and 2 when rotating the direction of the electric field (E) by 90° and thus the polarization from p to s.

The integration of Equation (3.10), $\int I^{LDAD}\, d\Theta\, d\Phi$, over all angles vanishes, that is, no linear dichroism in the total intensity is observed. It is also clear from Figure 3.9 that the linear dichroism appears only in the angular distribution. To observe a linear dichroism in the overall intensity one needs either fixed in space molecules [86, 78] or chiral objects [87]. The *chirality* may also be due to magnetic fields or remanent magnetization of samples leading to the magnetic linear dichroism [88].

In the present case, where the emitted electrons are detected either parallel (p) or perpendicular (s) to the electric field vector, the intensities and resulting LDAD are simply given by

$$\begin{aligned} I_\kappa^p &= \sigma_\kappa(1+\beta_\kappa), \\ I_\kappa^s &= \sigma_\kappa(1-\frac{\beta_\kappa}{2}), \\ I_\kappa^{LDAD} &= \sigma_\kappa\frac{3\beta_\kappa}{2}. \end{aligned} \tag{3.11}$$

For atoms or linear molecules, the dipole asymmetry parameter of s electrons is $\beta_{n0} \equiv 2$ in the non-relativistic approximation implying that $I_{n0}^s = 0$.

Electronic structure calculations of Au(111)

The electronic structure of Au was calculated by means of the fully relativistic Korringa-Kohn-Rostoker (KKR) method as implemented in the MUNICH-SPRKKR program package [89]. The k-integration mesh was set to a size of (22×22×22) during the selfconsistent cycles and a doubled k- mesh for calculation of the density of states and the spectroscopic properties. Figure 3.10 shows the density of states of Au calculated with SPRKKR. The main contribution to the density of states arises from d electrons.

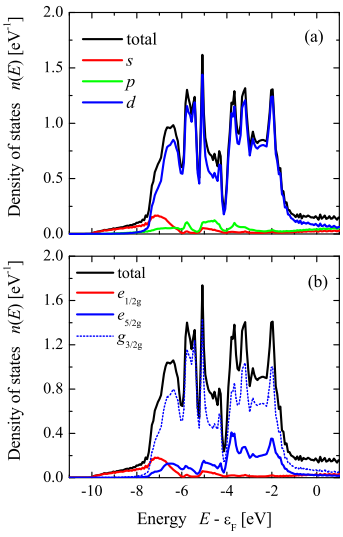

Figure 3.10: Density of states of Au.
(a) total and l resolved partial DOS (b) total and symmetry resolved partial density of states (shown are only the states with even (g) symmetry, that is the p states belonging to odd (u) representations are not shown.

The partial cross sections and angular asymmetry parameters were calculated in the dipole-length approximation by solving the Dirac-Hartree-Fock equations for bound and free electrons of free atoms. The program is based on a modified accurate fully relativistic Dirac-equation-solver developed by Salvat and Mayol [90, 91]. Due to the fast oscillating final state wave functions at 8 keV kinetic energy ($\lambda_{el} = 0.137$ Å), a very fine radial mesh (about 10^3 points per Å on a logarithmic mesh) had to be used for the integration of the radial matrix elements and calculation of the phases. The partial cross sections σ_{nlj} and angular asymmetry parameters β_{nlj} for the dipole length approximation are given in Table 3.1. The results for a photon energy of $h\nu = 8$ keV fit well into the energy dependent scheme of previously published values in the non- relativistic [92] and relativistic [93, 94] approaches. The β-parameter for s states is close to $\beta_{n,0,\frac{1}{2}} \approx 2$ in the relativistic calculation, as expected.

The photoelectron spectra may be simulated by multiplying the l, j resolved partial DOD (see figure 3.10) by the partial cross-sections. In the relativistic case one finds for

Table 3.1: Partial cross sections σ and angular asymmetry parameters β of the atomic valence electrons of Au at $h\nu = 8$ keV. The cross sections are given in kBarn. (Note: there is by definition a factor 8 between relativistic and non relativistic cross sections.)

State nlj	σ_{nlj}	β_{nlj}	State nl	σ_{nl}	β_{nl}
$6s_{1/2}$	3.129	1.93279	$6s$	0.312361	2
$5d_{3/2}$	13.467	1.15904	$5d$	3.29934	1.07286
$5d_{5/2}$	16.493	1.16542			

the geometry of the experiment:

$$\begin{aligned} I^p &\propto \sum n_{l,j}(E)\frac{\sigma_{nlj}}{2j+1}(1+\beta_{nlj}), \\ I^s &\propto \sum n_{l,j}(E)\frac{\sigma_{nlj}}{2j+1}(1-\beta_{nlj}/2), \end{aligned} \tag{3.12}$$

where $n_{l,j}(E)$ is the partial density of states and the sum is over all contributing valence states. The result is shown in Figure 3.11 and compared to measured spectra. In the model calculations using Equation 3.12, the energy interval of the valence states is small compared to the photon energy as well as the kinetic energy and the variation of the photoemission parameters is only small. Therefore, cross sections and angular asymmetry parameters at a fixed energy were used. The simulated spectra were finally convoluted by a Fermi-Dirac distribution for $T = 20$ K to account for the experimental cut-off at the Fermi energy and a Gaussian of 250 meV width to account for the experimental broadening.

The measured spectra shown in Figure 3.11(a) were normalized as described below. A Shirley-type background [95] was subtracted for better comparison with the simulated spectra where intensity from inelastically scattered electrons is not respected. The main features of the simple model calculation render roughly the ones of the measured spectra. However, major differences are observed if comparing the different polarization. Most striking is the complete vanishing, calculated intensity at below -8 eV where one finds the s electrons (see Figure 3.10). This is, indeed, caused by their β parameter being close to two even in the relativistic case.

The deviations make clear that the model of Equation 3.12 derived from the dipole transitions and Equation 3.9 is too simple. Indeed, it is clear that a Au single crystal is not a spherical object but has O_h symmetry according to its fcc lattice. The influence of the symmetry will be explained a little later. A different reason for deviations may be found in the high energies used in the experiment. One of these is the *recoil* effect [96] that leads to energy shifts. It is observed usually for light elements for example in graphite. Here this effect is rather improbable because of the large mass of the Au atoms. Another reason for deviations at high photon energies may be the occurrence of nondipole transitions that deform the angular distribution of the photoelectrons as described in the following.

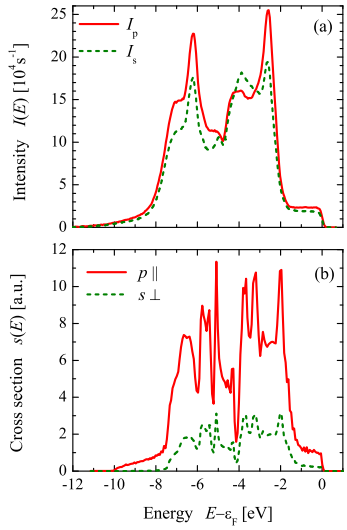

Figure 3.11: Measured and simple model spectra of Au(111).
(a) shows the spectra taken at 8 keV with p and s polarized X-rays, the spectra were normalized as described below (3.3.3) and a Shirley-type background was subtracted. (b) shows the simulated spectra for linearly p and s polarized light. The spectra were simulated by multiplying the partial density of states as given in Equation 3.12 and convoluted by the Fermi-Dirac distribution.

Non-dipole transitions

In addition to the E_1 transitions, higher-order nondipole terms may appear (M_1 and E_2 transitions) in addition to the E_1 transitions. The first- order nondipole approximation results in an additional term:

$$I_\kappa^{M_1,E_2} \propto \sigma_\kappa \left[(\delta_\kappa + \gamma_\kappa \cos^2\theta) \sin\theta \cos\phi \right] \tag{3.13}$$

in the angular distribution [97], with the angular parameters γ_κ and δ_κ that depend on the magnetic dipole and electric quadrupole matrix elements. Note that δ has to vanish if $\beta = 2$ or -1. The results is a distorted angular distribution compared to pure E_1 transitions.

In the present case, where the emitted electrons are either parallel (p) or perpendicular (s) to the electric field vector, the intensities are given by

$$\begin{aligned} I_\kappa^p &\propto \sigma_\kappa(1+\beta_\kappa), \\ I_\kappa^s &\propto \sigma_\kappa(1+\delta_\kappa - \frac{\beta_\kappa}{2}). \end{aligned} \tag{3.14}$$

In the present geometry, the spectra are not influenced by the γ_κ parameter. Using p polarized photons the spectra are nor affected by the nondipole terms. In the case of

s polarization, positive values of δ enhance and negative values attenuate the intensity. For s electrons where $\beta_{n0} \equiv 2$ in the non-relativistic approximation, one has $\delta_{n0} \equiv 0$. This shows that the nondipole terms are not able to explain the deviations between model and measurement especially for the part concerning the s electrons.

Selection rules in O_h symmetry.

The electronic states in solids usually do not carry a spherical or axial symmetry as in free atoms but have to follow the symmetry of the crystal [98]. The dipole selection rules for the O_h symmetry group are given in Table 3.2 for the non-relativistic group and in Table 3.3 for the relativistic double group representations. Further, non-relativistic and relativistic selection rules for the points and directions of high symmetry in cubic lattices are found in References [99] and [100], respectively. Table 3.2 gives also the basic functions of the irreducible representations up to the g states ($l = 4$). The relativistic representations are given in Table 3.3 up to the f states ($l = 3$) that form the cubic basis. For basis functions with higher orbital momentum ($l > 3$ or 4) see Reference [101].

Table 3.2: Non relativistic dipole selection rules for O_h.
Allowed transitions are marked by X. Note that for all possible transitions the parity is changed from g to u or vice versa. The basis symmetry functions ($F(ir)$) of the irreducible representations are given for $l \leq 4$. The e_u representation needs orbital momenta $l \geq 5$, a_{2g} needs $l \geq 6$, and a_{1u} needs $l \geq 9$.

	a_{1g}	a_{2g}	e_g	t_{1g}	t_{2g}	$F(ir)$
a_{1u}	.	.	.	X	X	$l \geq 9$
a_{2u}	.	.	.	.	X	f_{xyz}
e_u	.	.	X	X	X	$l \geq 5$
t_{1u}	X	.	X	X	X	(p_x, p_y, p_z) ,
	X	.	X	X	X	$(f_{x^3}, f_{y^3}, f_{z^3})$
t_{2u}	.	X	X	X	X	$f_{x(y^2-z^2)}$,
	.	X	X	X	X	$f_{y(z^2-x^2)}$,
	.	X	X	X	X	$f_{(x^2-y^2)z}$
$F(ir)$	s	$l \geq 6$	$(d_{z^2}, d_{x^2-y^2})$	$(g_{(x^2-y^2)z^2}, g_{z^4})$	(d_{xy}, d_{xz}, d_{yz})	
	g_{z^4}					
	$g_{(x^2-y^2)^2}$					

In the solid with O_h symmetry the photoexcitation of the s band is described better by a $a_{1g} \rightarrow t_{1u}$ transition as compared to an atom in which one simply has transitions into final p states [85, 98] due to its spherical symmetry. Restricting the partial waves of the initial a_{1g} state to $l = 0$ will allow already direct transitions into partial waves with $l' = 1, 3$ of the final t_{1u} state (see Table 3.4).

In the Au(111) single crystal the measured spectra are integrated over the extend of some Brillouin-zones [102, 80], but averag over different orientation, due to the fixed

Table 3.3: Relativistic dipole selection rules for O_h.
Allowed transitions are marked by X. Note that for all possible transitions the parity is changed from g to u or vice versa. The basis functions $F(ir)$ are given for $l \leq 3$. Note that the same l_j states may belong to more than one representation but with a different distribution of the m_j states.

	$e_{1/2g}$	$e_{5/2g}$	$g_{3/2g}$	$F(ir)$
$e_{1/2u}$	X	.	X	$p_{1/2}$, $f_{7/2}$
$e_{5/2u}$	.	X	X	$f_{5/2}$, $f_{7/2}$
$g_{3/2u}$	X	X	X	$p_{3/2}$, $f_{5/2}$, $f_{7/2}$
$F(ir)$	$s_{1/2}$	$d_{5/2}$	$d_{3/2}$, $d_{5/2}$	

crystal axis. For the investigated polycrystalline Heusler compounds (see chapter 10) with T_d symmetry (NiTiSn, NiMnSb), the obtained spectra are averaged not only over some Brillouin zones, but also over the random orientation of the crystallites.

Selection rules in T_d symmetry

The dipole selection rules for the T_d symmetry group are given in Table 3.4. The selection rules differ from those of the O_h group in the way that there is no distinction between states belonging to irreducible representations of even (g) or odd (u) parity due to the missing center of inversion. Further, non-relativistic and relativistic selection rules for the points and directions of high symmetry in cubic lattices are found in References [99] and [100], respectively. Table 3.4 gives also the basic functions of the irreducible representations up to the f states ($l = 3$) that form the cubic basis. The basis functions of the a_2 representation start at $l = 5$ and are omitted (for basis functions with higher orbital momentum ($l > 3$) see Reference [101]).

Table 3.4: Dipole selection rules.
Allowed transitions are marked by X. The basis functions are given for $l \leq 3$.

	a_1	a_2	e	t_1	t_2	basis functions
a_1					X	s, f_{xyz}
a_2				X		
e				X	X	$(d_{z^2}, d_{x^2-y^2})$
t_1		X	X	X	X	$(f_{x(y^2-z^2)}, f_{y(z^2-x^2)}, f_{(x^2-y^2)z})$
t_2	X		X	X	X	(p_x, p_y, p_z), (d_{xy}, d_{xz}, d_{yz}), $(f_{x^3}, f_{y^3}, f_{z^3})$

Normalization of the spectra

In the following, the normalization of the photoelectron spectra is explained at the example of spectra taken from a Au(111) single crystal.

The approach for normalization of the spectra is based on the fact that the secondary

electrons have lost after various inelastic scattering events the information in which direction the primary electrons were emitted and that the total amount of excited electrons (the total cross section averaged over the full space) is independent of the photon polarization. Further, one can make use of the fact that the sum of the intensities excited by linearly s and p polarized photons corresponds to the intensity obtained from unpolarized radiation $I_s + I_p = 2I_0$. In the same way, the sum of intensities for excitation with circularly polarized photons of opposite helicity (σ^+, σ^-) corresponds to excitation by unpolarized photons $I_{\sigma^+} + I_{\sigma^-} = 2I_0$.

Figure 3.12 shows the raw, near normal emission spectra of the Au(111) valence band excited by different kind of polarization. The angle of photon incidence was $\alpha = 89°$ with respect to the surface normal. The spectrum for p polarization was taken without phase retarder, whereas the spectra for s and σ^+ polarization were taken with phase retarder. The lower intensity, caused by the absorption of photons by the phase retarder, is evident. The secondary background at -12 eV is - compared to linear p polarization - by a factor ≈ 4.8 lower for circularly σ^+ and ≈ 10.8 lower for linearly s polarized photons.

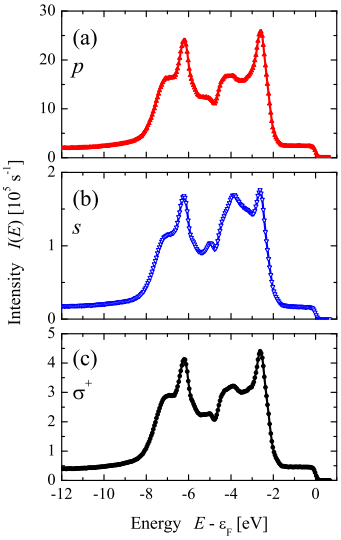

Figure 3.12: Normal emission valence band spectra of Au(111) ($h\nu = 7.039$ keV). Shown are the raw spectra obtained with linearly p (a) and s (b) and circularly σ^+ (c) polarized light (resolution: 150 meV).

Besides the overall change of intensity, the differences in the height of the maxima in the spectra are obvious. The intensity ratios $r = I(-2.6\,\text{eV})/I(-3.9\,\text{eV})$ of the first two maxima below the Fermi energy are $r_p = 1.54$, $r_s = 1.04$, and $r_{\sigma^+} = 1.37$ and thus clearly depend on the polarization. Figure 3.13 shows the spectra after scaling the spectrum taken with p polarization down to the secondary background of that taken with s polarization. The sum of the spectra taken with different linear polarization and different helicity are compared in Figure 3.13 (b) and (c). It is obvious that the *sum-*

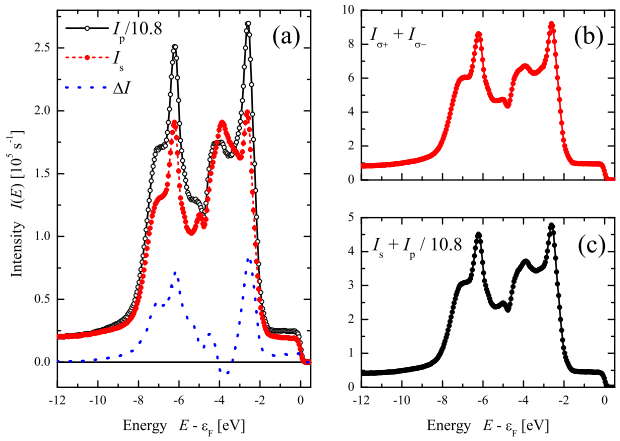

Figure 3.13: Normalized valence band spectra of Au(111).
Spectra obtained with s and p polarized light as well as the difference $I_s - I_p$ (a), $I_{\sigma^+} + I_{\sigma^-}$ (b) and, $I_s + I_p$ (c).

spectra have the same shape. Finally, the deviation of the r ratios of *sum*-spectra for circular and linear polarization are less than 3% and thus confirm the correctness of the scaling approach for the normalization of the spectra taken with excitation by linearly polarized photons.

4 Calculational Details

This chapter summarizes the details of the first principles calculations of the electronic structure and properties of the materials used in the present work.

The electronic structure and transport properties were calculated by all-electron ab-initio methods. The full potential linearized augmented plane wave (FLAPW) method as implemented in WIEN2k [103] in combination with a modified version of BOLTZTRAP [104] has been used for ordered, pure 1:1:1 compounds (for details see References [105, 106]). If not noted otherwise, the exchange-correlation functional was taken within the generalized gradient approximation (GGA) in the parametrization of Perdew-Burke-Enzerhof (PBE) [107]. A $(31 \times 31 \times 31)$ point mesh was used resulting in 816 k-points in the irreducible wedge of the Brillouin zone. The energy convergence criterion was set to 10^{-5} Ry and simultaneously the criterion for charge convergence to $10^{-3}e^{-}$. The muffin tin radii were set to nearly touching spheres. For the calculation of the transport properties the tetrahedron method and energy steps of $\approx 0.16 \times 10^{-04}$ Ry were used for integration. Relaxed lattice parameters were used in all calculations. For example, the optimization of the volume resulted in $a = 5.9534$ Å for NiTiSn. Typical for the use of GGA, this value is slightly larger (0.6%) compared to the one found from experiments. This is not a critical issue as the band gap is rather stable against variation of a independent on the used functional (see below).

The electronic structure calculations of the substitutionally disordered $NiTi_{1-x}M_xSn$ and $CoTi_{1-x}M_xSb$ (where M = Sc, V and $0 < x \leq 0.2$) have been performed by means of the fully relativistic Korringa-Kohn-Rostoker (KKR) method in combination with the coherent potential approximation (CPA) as implemented in the MUNICH -SPRKKR program package [108]. The k-integration mesh was set to a size of $(22 \times 22 \times 22)$ during the selfconsistent cycles. The gradient correction of the PBE-functional was switched off for the vacant site to avoid numerical instabilities caused by low charge densities.

The CPA allows electronic structure calculations for systems with random distribution of the atoms as is here the case where M substitutes partially Ti. For the substitutional compounds, the CPA method has been used to model the statistic distribution of the atoms on the M site and the Ti atoms on a common site of the $C1_b$ crystalline structure. The Ni or Co atoms are placed on the 4a Wyckoff position, the Ti atoms are placed together with the M atoms on the 4c position, and the main group element Sn or Sb are finally placed on the 4d position of the cell with $F\bar{4}3m$ symmetry (space group 216). The swap-type disordered NiTiSn (for example $Ni_{1-x}Vc_xTiSn$) compound was also treated using the CPA method by placing a fraction of x vacancies (Vc) on regular sites and simultaneously the swapped part $(1 - x)$ on the 4b Wyckoff position.

The conductivity of the compounds with random substitution was calculated using the Kubo-Greenwood linear response formalism as described in Reference [109] including vertex corrections [110]. The original formulation [110] was for the case of one site per cell and is extended in the present work to include primitive cells with a basis that contains

several different sites. The chemical disorder scattering resistivities of $NiTi_{1-x}M_xSn$ and $CoTi_{1-x}M_xSb$ were calculated using an enlarged $(92 \times 92 \times 92)$ k-mesh.

The transport properties discussed in this work depend, indeed, critically on the size of the band gap. It is often noted that the local density approximation underestimates the band gaps of semiconductors and insulators (for a recent discussion see Reference [111]). Very often, specialized functionals (for example the Engel-Vosko GGA functional (EV) [112]) or hybrid functionals including Hartree-Fock exchange (for example Becke's B3LYP [113]) give better values for the band gaps if applied to *sp* element based semiconductors, likewise Ge (0.17 eV with PBE, 0.65 eV with EV, and 0.78 eV in experiments) or GaAs (0.48 eV (PBE), 1.04 eV (EV), 1.5 eV (exp)). To check for influences of the exchange correlation functional, the electronic structure of NiTiSn was also calculated using the LSDA [114], EV-GGA [112], and by the hybrid PBEsol [115] functionals. Surprisingly, the size of the band gap stayed stable within less than 100 meV without remarkable changes of the band structure. This points to a fundamental difference in the description of *d*-element based Heusler semiconductors compared to the *sp* element materials. Obviously, the band gap of the *d*-element semiconductors investigated here is much less influenced by the choice of the functional as compared to *sp*-type semiconductors.

The mechanical properties were calculated in addition to the optimization of the lattice parameters. Besides the bulk modulus B that is found directly from the equation of states fit [116, 117], the elastic constants c_{ij} were calculated for CoTiSb and Co_2MnGe as well as the iso-valent compound Co_2MnSi. The elastic stability criteria for the cubic structure are found from the elastic constants (c_{ij}) [118, 119, 120]. The necessary conditions are:

- a) $c_{11} + 2c_{12} > 0$
- b) $c_{44} > 0$
- c) $c_{11} - c_{12} > 0$

that is, the bulk, c_{44}-shear, and tetragonal shear moduli all have to be positive. The elastic anisotropy is defined for cubic crystals by:

$$A_e = \frac{2c_{44}}{c_{11} - c_{12}}. \tag{4.1}$$

A_e also allows a decision about the structural stability. Materials exhibiting large A_e ratios show a tendency to deviate from the cubic structure under applied external forces.

The vibrational properties of Co_2MnGe and CoTiSb were calculated by means of PHONON [121] on the basis of the results from WIEN2k. The primitive cell of Co_2MnGe containing four atoms was enlarged to a cell with 16 (or 12) distinguished atoms to calculate the Hellmann-Feynman forces for the phonon analysis. For these calculations, a force convergence criterion of 10^{-4} Rya_{0B}^{-1} was used in addition to the energy convergence criterion.

5 Experimental Details

This chapter summarizes the details of the sample preparation and measurement of the materials properties.

All bulk samples were prepared by arc melting of stoichiometric amounts of the constituents in an argon atmosphere. To ensure the homogeneity of the samples they were remelted several times. The arc melting results in polycrystalline ingots. The as-cast samples were subsequently annealed.

The Co_2MnGe ingots were annealed in an evacuated quartz tube for 7 days at 800°C and subsequently for another 7 days at 1000°C. Directly after annealing, the hot ingots were quenched in ice water. This procedure resulted in samples exhibiting the Heusler type $L2_1$ structure, which was verified by XRD using Mo K_α radiation as well as synchrotron radiation.

The series $NiTi_{1-x}M_xSn$ (M = Sc, V and $x = 0, \ldots, 0.1$) was subsequently annealed at 950°C for 72 h followed by quenching in ice-water in order to improve the crystalline order. The existence of a single and compositionally homogeneous phase was verified by X-ray powder diffraction using MoK_α radiation. The determination of the lattice parameters and the crystal structure refinements were performed using the Rietveld method.

To compensate the loss of the Sb during the arcmelting of the series $CoTi_{1-x}M_xSb$ (M = Sc, V and $x = 0, \ldots, 0.2$), an excess of 3% Sb was used. The ingots were wrapped in tantalum foil and annealed at 700°C for 10 days under argon in quartz ampules, followed by slow cooling to room temperature. To compensate the loss of the main group elements during the arcmelting of the polycrystalline samples PtYSb, PtLuSb and PtLaBi an excess of 3% Sb and 5% Bi was used. The ingots were then annealed in evacuated quartz tubes at 800°C for two weeks.

Anomalous XRD experiments were performed at the X-ray powder diffraction beamline [122] at the bending magnet D10 of the Brazilian Synchrotron Light Laboratory (LNLS). The powder samples were used in complementary EXAFS measurements, which have been performed at the XAFS1 beamline of LNLS [123] using a Si 111 channel-cut monochromator. The spectra were collected at the Co (7709 eV), Mn (6539 eV), and Ge (11103 eV) K edges at room temperature in the transmission mode using three ionization chambers. Standard metal foils were placed at the third chamber to check the monochromator energy calibration.

The transport, hall and specific heat measurements were performed by means of a physical properties measurement System (PPMS; Quantum Design model 6000, supported by LOT, Germany). For transport measurements, sticks of $(2 \times 2 \times 8)$ mm^3 were cut from the ingots. The measurements of the Seebeck coefficient, thermal conductivity, and resistivity were performed using the thermal transport option (TTO) with the

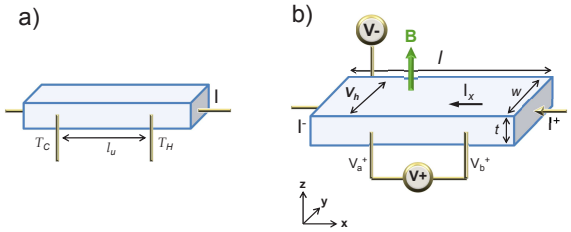

Figure 5.1: Schematic illustration of a) thermal transport and b) five-wire-probe hall measurement.

four-probe method as shown in Figure 5.1a).

Hall measurements were performed by an AC transport measurement system (ACT) option in applied magnetic fields up to 5 T using a five-wire method (as shown in Figure 5.1b). For the specific heat measurements, small sample pieces of approximately 4 mg were used. The temperature was varied from 1.8 K to room temperature or 350 K. All measurements were performed at a residual pressure of about 9.0×10^{-5} mbar in the chamber.

For the hard X-ray photoelectron spectroscopy (HAXPES) the sample sticks as used for the transport measurements were fractured *in situ* in the ultra-high vacuum (UHV) chamber before each measurement to avoid contamination when exposed to air.

For the measurements with linearly polarized photons polycrystalline samples were cut to discs and the surface was polished. The Au(111) sample surface was prepared by Ar^+ bombardment to remove traces of oxidation. The cleanness of the samples was checked by regular low-energy XPS (Al $K\alpha$).

The HAXPES experiments were performed using the beamlines BL15XU [124] and BL47XU at SPring-8 (Japan) [54]. In the regular set-up, photons with energies of 3.237 keV, 5.9468 keV (BL15XU) or 7.938 keV (BL47XU) that were linearly p polarized in the horizontal direction were used for selective excitation. The p polarized light was obtained from undulator sources without the use of any polarization optics. At BL15XU, the photons were monochromized using a Si(111) double crystal monochromator and the (220) or (333) reflexion of a Si channel-cut post monochromator for 3.237 kev, or 5.9468 keV, respectively. At BL47XU, the ((444) reflections of the channel-cut post monochromator following the Si(111) double crystal monochromator were used to fix the energy.

At both beamlines, the kinetic energy of the photoemitted electrons was analyzed using hemispherical analyzers (VG-Scienta R4000-HV). The overall energy resolution was set to 150 or 250 meV, as verified by the spectra obtained at the Fermi edge of a Au sample. The angular resolution was set to 2°. The angle between the electron spectrometer and photon propagation was fixed at 90°. The detection angle was set to $\theta = 2°$ in order to reach a near-normal emission mode. The angle of incidence of $\alpha = 88°$ ensures that the polarization vector of the p polarized photons is either nearly parallel to the surface normal. The experimental set up is sketched in Figure 5.2.

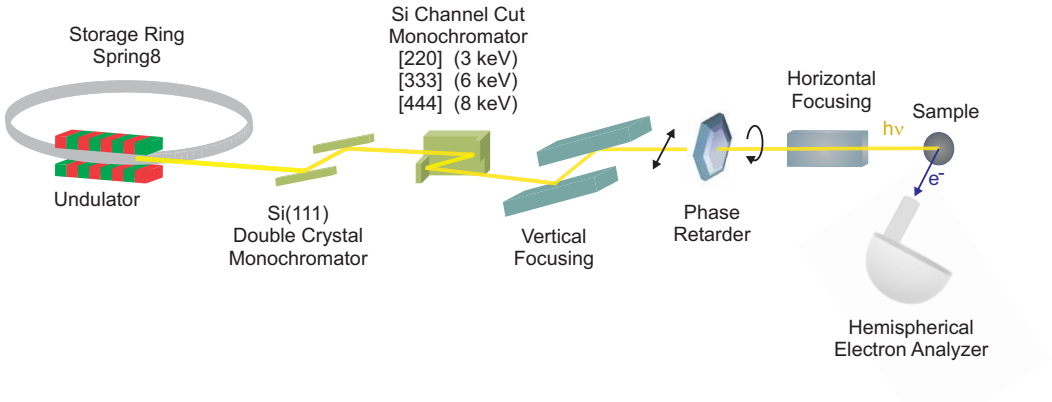

Figure 5.2: Set up of the HAXPES experiment (beamline BL15XU and BL47XU at SPring-8, Japan).

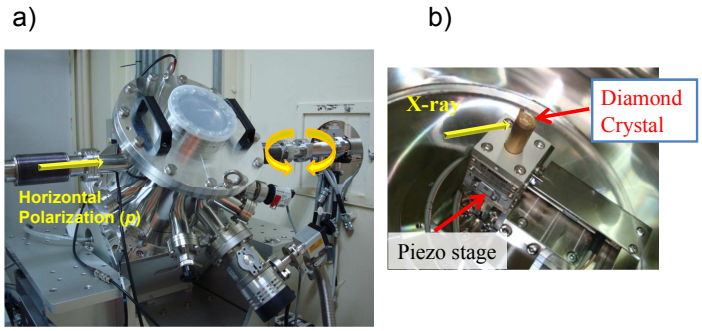

Figure 5.3: An in-vacuum phase retarder at BL47XU (a) and the 200-μm-thick diamond crystal with (220) orientation (b).

For polarization dependent HAXPES at BL47XU, an in-vacuum phase retarder based on a 200-μm-thick diamond crystal with (220) orientation [125] was used to rotate the linear polarization into the vertical plane or to produce circularly polarized photons (see Figure 5.3).

The direct beam is linearly polarized with $P_p = 0.99$. The degrees of polarization were $P_L = (I_h - I_v)/(I_h + I_v) = 0.99$ for p polarization and $-0.7 \cdots - 0.9$ for s polarization, where I_h and I_v denote the X-ray intensities of the horizontal and vertical polarization components, respectively. The nearly gracing incidence ensures that the polarization vector of the linearly polarized photons is either nearly parallel (p) or perpendicular (s) to the surface normal. The use of the phase retarder for s polarized light considerably decreases the overall intensity because of the absorption by the diamond crystal. The integration of the count rate over the valence band of NiTiSn results in a ratio of $I^p/I^s \approx 20$ when p polarization without the phase retarder is compared with s polarization with the retarder. For circularly polarized photons the polarization vector is nearly parallel (σ^+) or antiparallel (σ^-) to the in-plane magnetization M^+. The sign of the

magnetization was varied by mounting samples with opposite directions of magnetization (M^+, M^-). Using the phase retarder, the degree of circular polarization is set to $P_c > \pm 0.9$. The circular dichroism is characterized by an asymmetry that is defined as the ratio of the difference between the intensities I^+ and I^- and their sum, $A = (I^+ - I^-)/(I^+ + I^-)$, where I^+ corresponds to σ^+- polarized light and I^-, to σ^-- type helicity.

6 Structure and Properties of the Half-Metallic Heusler Compound Co_2MnGe

6.1 Introduction

Heusler compounds have recently attracted increasing interest, owing to their multifarious properties [126]. Research on half-metallic ferromagnetic materials based on Heusler compounds has been rapidly growing since its prediction for NiMnSb in 1983 by de Groot and co-workers [2]. Several Heusler alloys crystallizing in the space groups $L2_1$ have been verified to be half-metallic ferromagnets by electronic band structure calculations [10]. Kübler and co-workers demonstrated that in many Heusler alloys the minority spin density of states (DOS) exhibits a band gap at the Fermi energy while the majority spins are responsible for the metallic properties. Those compounds are considered one of the most useful candidates for tunneling magnetoresistance (TMR) devices, because the magnetoresistance (MR) is expected to be large if the conduction electron spins are 100% polarized. This conduction electron spins can be possibly injected into a semiconductor, when the materials are epitaxially grown on the semiconductor surface.

The Heusler alloy Co_2MnGe, a half-metallic compound, is considered one of the most useful candidates for spintronics since it combines a high Curie temperature (905 K) [18] and coherent growth on top of semiconductors. Recently, several groups were successful in growing Co_2MnGe epitaxially on semiconductor substrates [127]. Ishikawa and co-workers [128] and Hakamata and co-workers [129] have already fabricated epitaxial magnetic tunnel junctions (MTJs) based on Co_2MnGe and a MgO tunnel barrier, and they found relatively high tunnel magnetoresistance ratios of 185% at 4.2 K and 83% at room temperature with a Co-rich Co_2MnGe film. They have shown that the TMR ratio depends on the amount of Co in Co_2MnGe. Therefore, a systematic study of the influence of the crystal quality on the magnetic and transport properties as well as the half-metallicity in the compounds needs to be made.

This chapter presents a comprehensive theoretical and experimental study of the Heusler compound Co_2MnGe. Electronic structure calculations were carried out to verify and explain its half-metallic ferromagnetic behavior. Anomalous X-ray powder diffraction (aXRD) and extended X-ray absorption fine-structure spectroscopy (EXAFS) were performed for the structure determination and to obtain the cell parameters. To open new fields of application for Heusler compounds, the mechanical and vibrational properties of Co_2MnGe were calculated and the hardness of the compound was experimentally determined. Furthermore, measurements of the magnetic as well as transport properties were performed. To verify the calculated electronic structure a detailed investigation by hard X-ray photoelectron spectroscopy (HAXPES) was carried out.

6.2 Results and Discussion

6.2.1 Magnetic properties

The magnetic properties of the polycrystalline Co_2MnGe samples were investigated with a superconducting quantum interference device (SQUID, Quantum Design MPMS-XL-5) using small pieces of 23.6 mg. The magnetic moment was determined to be $4.982\mu_B$ at 5 K (see Figure 6.1). Owing to the high Curie temperature of the compound, no noteworthy changes were detected for temperatures up to 300 K.

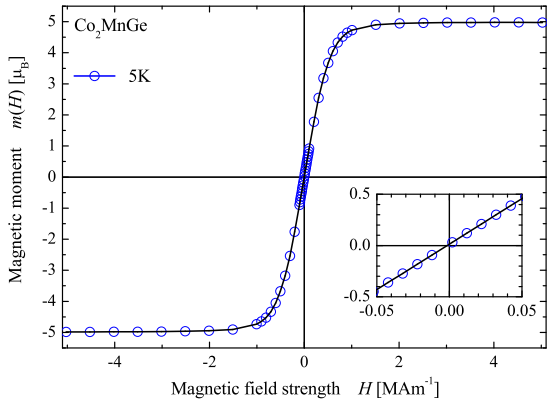

Figure 6.1: Low-temperature magnetization of Co_2MnGe.

6.2.2 Structure determination by EXAFS and aXRD

The powder diffraction pattern taken with Mo K_α radiation (not shown here) did not exhibit the (002) fcc superstructure reflection, because of the nearly equal scattering amplitudes of the constituent elements, and the intensity of the 111 reflection was extremely low. This complicates the unambiguous determination of the details of the structure. A lattice parameter of about ≈ 5.75 Å was found from a Rietveld refinement of the low resolution Mo K_α XRD data. Additional high resolution synchrotron-based scattering experiments have been performed to overcome the problems of structure determination by XRD with Mo K_α radiation.

Synchrotron-based absorption and scattering experiments (EXAFS and aXRD) were performed because of the problems in unambiguously determining the structure in laboratory XRD experiments using Mo K_α radiation. In the first step, the raw EXAFS spectra allow to select the energies of the K absorption edges of the contributing elements that are used for the aXRD. The aXRD data then allow for a better description of the long-range order and crystalline structure to be used for the fitting of the EXAFS data. Figure 6.2 displays the X-ray absorption spectra (XAS) taken at the K edges of Co, Mn, and Ge. The XAS spectra correspond to f'' and exhibit the typical EXAFS intensity modulations. The program FPRIME [130] was used to find the f' parameter from

an Kramers-Kronig analysis. (f' and f'' are the real and imaginary parts, respectively, of the atomic scattering factor.)

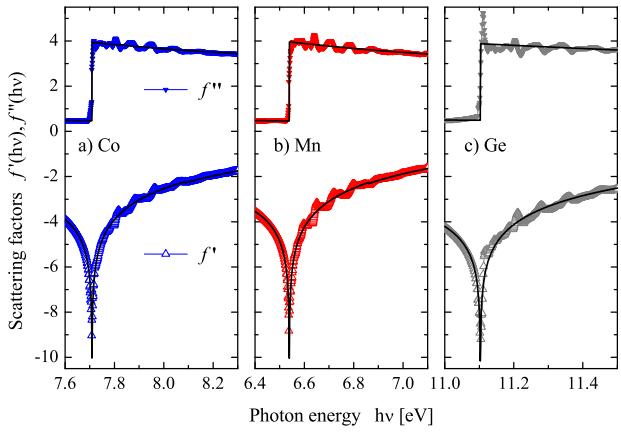

Figure 6.2: K-edge absorption spectra and Kramers-Kronig analysis of the Co_2MnGe EXAFS data. The absorption spectra correspond to f''. For all spectra, the intensity was normalized to the photon intensity and afterwards to an *edge jump* of one after subtracting a constant background.

Figure 6.3 compares the results of the aXRD experiments performed at a sample temperature of 300 K. At off-resonant excitation (7112.27 keV) the fcc (111) and (200) superstructure reflections of the ordered $L2_1$ structure are weakly visible. The situation is different if the energy is moved closer to the K absorption edge of Mn at 7112.27 keV, where a strong enhancement of the (111) reflection is observed. The 200 reflection appears already for samples with $B2$ structure, whereas (111) appears alone in the $B32$ structure. The appearance of both together is indicative for $L2_1$ or DO_3 type structures. The higher intensity of the (111) reflection compared to (200) gives clear evidence for the $L2_1$ structure as the dominant phase in the sample.

The aXRD data were analyzed in more detail using Powdercell [131] with anomalous scattering parameters calculated by SCATFAC [132]. The results of the Rietveld refinement are summarized in Table 6.1. The results from the measurement with Mo K_α radiation are given for comparison. The lattice parameter averaged over the high resolution synchrotron measurements taken with different energies is $\overline{a} = (5.7477 \pm 0.0017)$ Å. The analysis of the aXRD data makes the $L2_1$ structure of Co_2MnGe clearly evident.

Figure 6.4 summarizes the results of the EXAFS analysis of the x- ray absorption spectra taken at the K edges of Co, Mn, and Ge. The XAS spectra were analyzed in accordance with the standard procedure of data reduction [133], using IFEFFIT [134]. FEFF was used to obtain the phase shift and amplitudes [135]. The EXAFS signal χ(k) was extracted and then Fourier transformed using a Kaiser-Bessel window with a Δk range of 9.0 Å^{-1}. The $\chi(k)$ curves display the characteristic pattern of a cubic structure, as expected for this Heusler compound. The Fourier transforms (FTs) display two well-

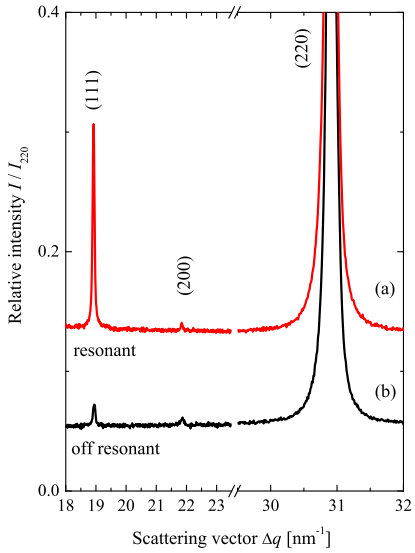

Figure 6.3: Anomalous XRD of polycrystalline Co_2MnGe. The data were taken at room temperature using synchrotron radiation for excitation. The excitation energy was set to (a) 6539.89 eV (Mn resonant) or (b) 7112.27 eV (off-resonant).

Table 6.1: Anomalous XRD of polycrystalline Co_2MnGe. The data were taken resonant at the Mn K absorption edge (6539.89 keV), off-resonant (7112.27 eV), and with Mo K_α radiation (17479.2 eV). The R values of the refinement are given in percent.

	Mn resonant		Off-resonant		Mo K_α	
	exp.	calc.	exp.	calc.	exp.	calc.
I_{111}/I_{220}	0.207	0.207	0.019	0.023	0.025	0.019
I_{200}/I_{220}	0.041	0.048	0.007	0.006	0	0.002
R_p	5.88		3.37		6.24	
R_{wp}	8.61		9.49		9.84	

defined peaks at about 2.2 and 4.5 Å (uncorrected for the phase shift), which correspond to the scattering contribution in the coordination shell and next nearest neighbors. Multiple scattering contributions appear in the region between the two main peaks. The best-fitting curves (gray lines) of the EXAFS signal and FT modulus considering the $L2_1$ structure are also displayed in Figure 6.4. Single and multiple scattering events were considered in the fitting procedure. The overall fitting procedures of all elements contained in Co_2MnGe lead to physically reasonable numbers close to those of the theoretical structural model. A quantitative analysis extracted from the EXAFS data is presented in Table 6.2. The obtained amplitude-reduction term (S_0^2) varied between 0.70 and 0.84. The shifts in distances (ΔR) were also small, with a typical variation from

−0.02 to −0.07 Å. Excellent agreement between the data and the theoretical $L2_1$ model was accomplished, as demonstrated in Figure 6.4 and by the low R factors (< 1% in Table 6.2).

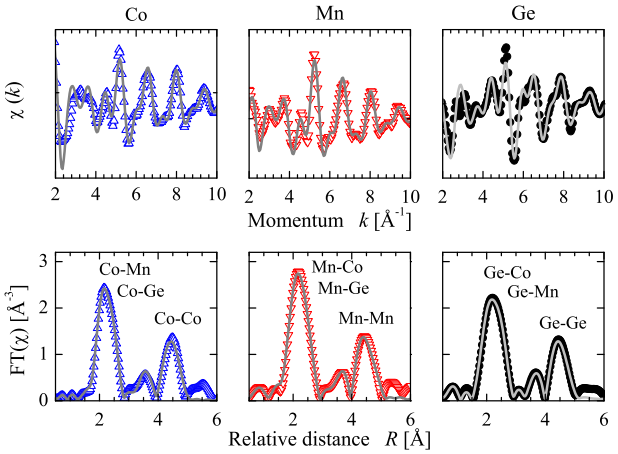

Figure 6.4: EXAFS oscillations (top rows) extracted from the X-ray absorption measurements at the K edges of Co, Mn, and Ge, along with the corresponding Fourier transforms (bottom rows, symbols) and best-fitting results (gray lines).

Table 6.2: Co_2MnGe EXAFS data analysis. Results are obtained from the quantitative analysis of the EXAFS data for the Co, Mn, and Ge K edges, considering the coordination numbers (N) of the $L2_1$ structure. The best fitting provided the next neighbor distances (d), Debye-Waller factor σ^2, and R factor for each absorbing atom.

Pair	N	d (Å)	σ^2 (10^{-2} Å^2)	R (%)
	Co K edge (7709 eV)			
Co-Mn	4	2.47±0.02	0.63±0.02	
Co-Ge	4	2.47±0.02	0.63±0.02	0.89
Co-Co	6	2.85±0.02	0.81±0.05	
Co-Co	12	4.04±0.03	1.2±0.1	
	Mn K edge (6539 eV)			
Mn-Co	8	2.47±0.02	0.63±0.02	
Mn-Ge	6	2.86±0.02	0.70±0.1	0.49
Mn-Mn	12	4.08±0.04	1.0±0.1	
	Ge K edge (11103 eV)			
Ge-Co	8	2.47±0.02	0.63±0.02	
Ge-Mn	6	2.86±0.02	0.70±0.1	0.57
Ge-Ge	12	4.04±0.04	0.80±0.1	

6.2.3 Electronic structure calculations

The electronic and magnetic structures were investigated with *ab initio* calculations using WIEN2k [103]. As a starting point the lattice parameter was optimized by using the generalized gradient approximation in the parametrization of Perdew-Burke-Enzerhof [107]. The relaxed lattice parameter is $a = 5.7301$ Å at a bulk modulus of 317 GPa. Figure 6.5 shows the band structure of Co_2MnGe calculated for the relaxed lattice parameter. The compound is a half-metallic ferromagnet with a gap in the minority states. This finding is in good agreement with previously reported calculations [136]. The size of the minority gap amounts to $\Delta E = 0.58$ eV. The top of the minority valence band is about 70 meV below ϵ_F. Owing to the half-metallic character the magnetic moment in the primitive cell is $5\mu_B$, in excellent agreement with the Slater-Pauling rule [19].

Additional details of the electronic structure are revealed in Figure 6.6, which shows not only the total DOS but also the site, orbital momentum, and symmetry-resolved DOS. The states below -9 eV are of a_{1g} character and mainly located in the vicinity of the Ge sites. The occupied d states are found between ϵ_F and -5 eV. The existence of the minority band gap at ϵ_F is obvious from all DOS plots. Its size and position are exclusively determined by Co states (compare Figure 6.6(a) and 6(b)). At the minority valence-band maximum the Co states are of t_{2g} character whereas they have e_g character at the minimum of the minority conduction band (see Figure 6.6(d)). The electrical conductivity of the compound is determined by the strongly dispersing majority bands at ϵ_F. They are rather delocalized and cannot be assigned to a particular site of either Co or Mn. From Figure 6.6(d), it is seen that the d electron densities located close to Co exhibit

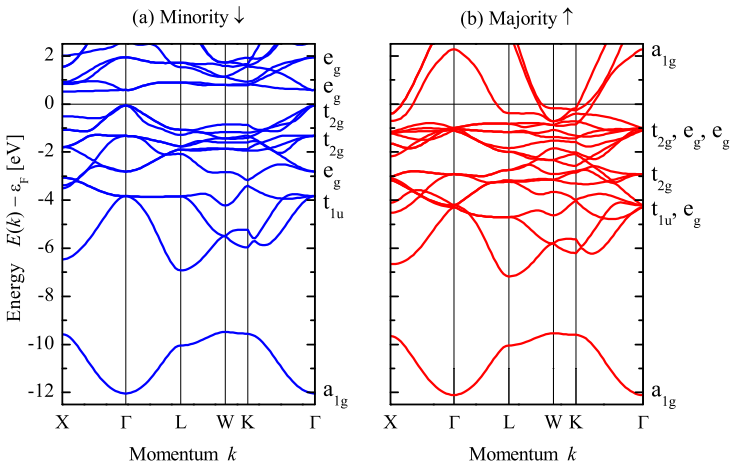

Figure 6.5: Calculated band structure of Co_2MnGe for (a) minority states and (b) majority states, respectively. The irreducible representations of the states at the Γ point are marked for O_h symmetry. Note that the subscripts g and u are given in the standard notation for states with even and odd parity with respect to the orbital angular momentum. The series of irreducible representations for majority states being close together is given from left to right, starting with the topmost state (see also the scheme in Figure 6.7(c)).

a nearly uniform distribution over the energy range of the valence bands, independent of the symmetry or spin character. In contrast, the valence electrons attributed to the Mn site exhibit a pronounced localization at -1 eV (e_g) and around -3 eV (t_{2g}) in the majority channel. This leads to a distinct exchange splitting of 2.8 eV between the occupied majority and unoccupied Mn e_g states. The spin-averaged decomposition of the number of occupied d states localized in the vicinity of Co or Mn is summarized in Table 6.3.

Table 6.3: Site-resolved magnetic moments (m) and d state occupancy n_d of Co and Mn in Co_2MnGe. All magnetic moments (m) are given in μ_B.

	Co			Mn		
	d	e_g	t_{2g}	d	e_g	t_{2g}
n_d	7.4	2.7	4.7	5.1	1.9	3.1
m	1.0	0.9	0.1	3.0	1.55	1.45

Given the previous considerations it should be noted that many of the electrons are located in the interstitial space between the muffin-tin spheres describing the atoms of the primitive cell and thus cannot be specifically attributed either to one or another of the contributing elements or a specific orbital momentum. At this point—and before

continuing with the magnetic moments—recall that, from the objective point of view of the solid, all electrons are indistinguishable whereas only a subjective observer divides the solid arbitrarily into spheres or other objects of a given but virtual size. Strictly speaking, the dispersion $E(k)$, total density of states, and total magnetic moments are the only well-defined ground-state quantities but they are not the site-resolved ones.

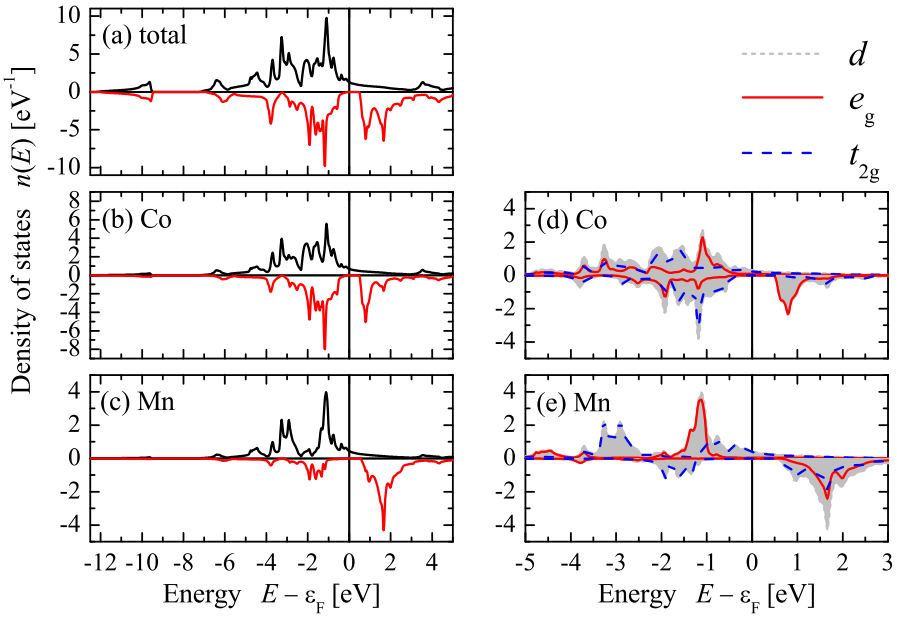

Figure 6.6: Partial density of states of Co_2MnGe. (Note the different scales of the $n(E)$ plots.)

Galanakis and co-workers [136] explained the half-metallicity of Co_2MnGe by a particular molecular orbital coupling scheme. To develop the model, they had to assume, however, that the Co atoms are in an environment with O_h symmetry. This assumption is incorrect even though the total symmetry of the cubic cell of $L2_1$ Heusler compounds is O_h. The sites occupied by Co have no inversion symmetry and carry T_d symmetry, as is evident from the primitive cell shown in Figure 6.7(b). In contrast, the sites occupied by Mn and Ge exhibit O_h symmetry. Alternative molecular orbital diagrams are developed in Ref. [126] for the examples of half-metallic Co_2MnSi and semiconducting Fe_2VAl. Figure 6.7(c) shows schematically, without assumption of any particular molecular orbital coupling scheme, directly the order of the states at the Γ point of Co_2MnGe. The half-metallic character determined by the band filling of the minority states is obvious. The successive complete filling of the minority bands (a_{1g}, t_{1u}, e_g, $2 \times t_{2g}$) by 12 electrons leads to a quasi-closed-shell character. The energy scheme for the majority electrons is considerably different from that of molecular orbital models. It is seen that the additionally occupied doubly degenerate states are pushed at Γ below the triply degenerate states. Finally, the strongly dispersing high-lying (a_{1g} and t_{1u} character at Γ) majority bands start to cross ϵ_F and bring the majority electronic structure close to

a simple metal (compare Figure 6.5 and 6.7(b)). Both effects together show the limits for the application of molecular orbital schemes. The latter has another important consequence: When the two additional e_g states are occupied one reaches compounds with 28 valence electrons overall, which exhibit a total spin moment of $4\mu_B$. At that valence electron concentration the "localized" weakly dispersing bands are used up and a further increase will need to fill "delocalized" states with strong band dispersion. The filling of these bands needs a rather large exchange interaction to split the occupied and unoccupied localized states. It seems that there is a limit at which the exchange interaction cannot be increased further. This limit is reached when the compound has 30 valence electrons, that is, when about two "delocalized" majority bands are filled. This explains why Heusler compounds with magnetic moments of considerably more than $6\mu_B$ are not known, in contrast to fully localized, nondispersing molecular orbital schemes that suggest $7\mu_B$ as a limit [136].

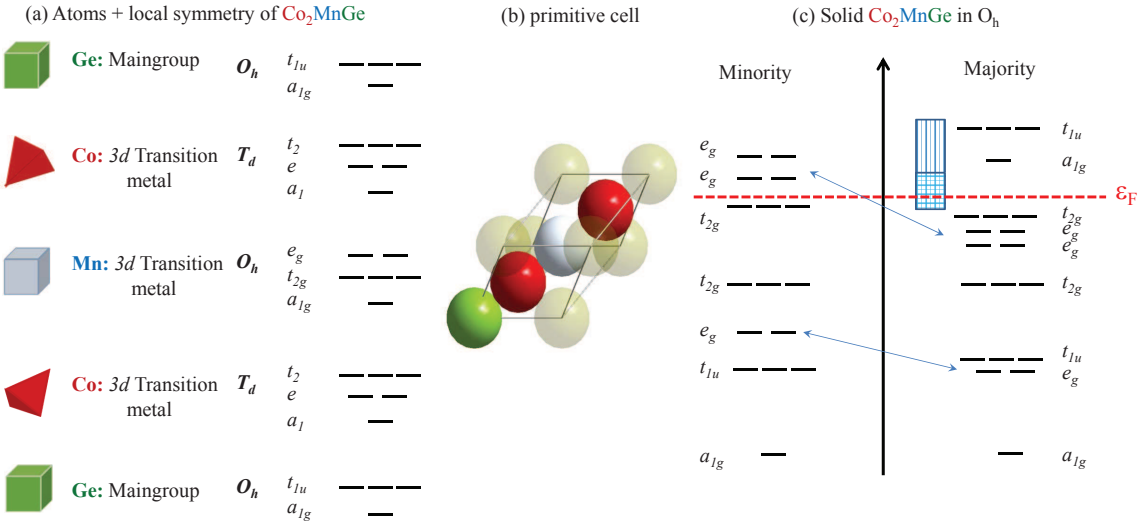

Figure 6.7: Schematic illustration of the orbitals and states in Co_2MnGe. The local symmetries and basic states of the atoms in an environment with O_h symmetry are shown in (a). The primitive fcc cell with a base of four atoms as shown in (b) reveals the center of inversion of the O_h symmetry group. (c) is a schematic of the states at the Γ point of the solid with O_h symmetry. The box in (c) indicates that the unoccupied majority states with a_{1g} and t_{1u} character are delocalized and smeared over a wide band of energies in k space.

The calculated ground-state magnetic moment of $5\mu_B$ in the primitive cell agrees well with the measured saturation magnetic moment of $4.982\mu_B$ at 5 K. The calculations reveal that the site-resolved moments per atom are about 1 and $3\mu_B$ at Co and Mn, respectively. Besides the site-specific moments, the symmetry-resolved moments are of interest, that is, the distribution of the moments arising from the e_g and t_{2g} states. The site- and symmetry-resolved values are summarized in Table 6.3. It is seen that the

site-resolved moments arise exclusively from the d electrons for both constituents Co and Mn. At the Co site one obtains $n_d^{\mathrm{Co}} = 7.4$ d states, from which 4.7 d states have t_{2g} character; however, the main part of the moment arises from e_g states, which have a lower occupancy of $n(e_g) = 2.7$. The situation is different at the Mn site, where one has a d state occupancy of $n_d^{\mathrm{Mn}} = 5$ with a $n(e_g)/n(t_{2g})$ ratio of about 2/3. At Mn, the d states of both symmetries contribute uniformly about $1.5\mu_B$ to the site-resolved moment.

The site-resolved magnetic moments are in good agreement with measurements using X-ray magnetic dichroism (XMCD), which resulted in spin magnetic moments of $m_{\mathrm{Co}} = 0.93\mu_B$ and $m_{\mathrm{Mn}} = 3.25\mu_B$ [137, 138, 139, 140].

6.2.4 Hard X-ray photoemission

Core-level spectroscopy

Hard X-ray core-level spectra of Co_2MnGe were measured to investigate the spin-orbit splitting as well as the exchange interaction of the unpaired valence electrons with the core holes. The spectra of the Co $2p$ and Mn $2p$ core levels are shown in Figures 6.8(a) and 6.8(b), respectively. The spectra are taken at low temperature (16 K) with an excitation energy of about 8 keV. The spin-orbit interaction splits the $2p$states into $p_{1/2}$ and $p_{3/2}$. The additional splitting by the magnetic exchange (for explanation see below) is assigned by EX.

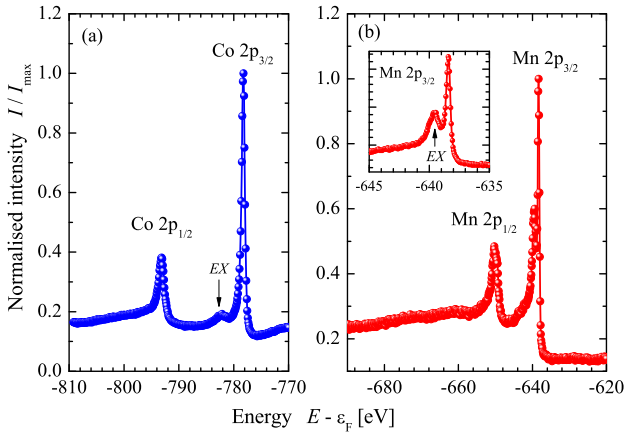

Figure 6.8: High-energy photoelectron spectra of the Co $2p$ (a) and Mn $2p$ (b) core level of Co_2MnGe. The spectra are excited by a photon energy of $h\nu = 7.9392$ keV at low temperature (16 K). The inset in (b) shows the details of the Mn $2p_{3/2}$ state on a stretched scale.

Figure 6.9 shows the hard X-ray photoelectron spectrum of Co_2MnGe in the energy range of the semi-core level. (Note the low intensity of the valence band). Details of the energies are summarized in Table 6.4. Obviously, the spin-orbit splitting of the Ge

$3p$ state is more pronounced than the one of the Co $3p$ state even though the nuclear charge Z_{Ge} is only five higher than Z_{Co}.

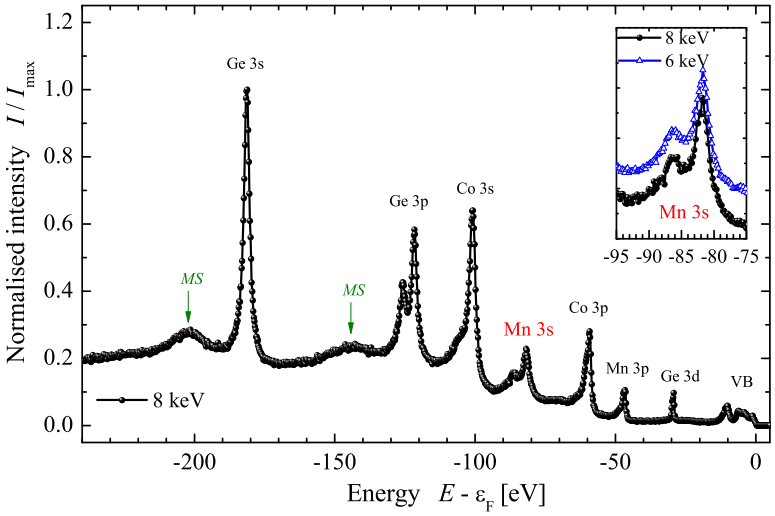

Figure 6.9: Semi-core-level spectra of Co_2MnGe. The spectrum was taken at 300 K and excited by a photon energy of $h\nu = 7.9392$ keV. The inset shows a magnified view of the Mn $3s$ state taken at different photon energies (5.9468 and 7.9392 keV).

Besides the spin-orbit splitting of the p states, the spectra shown in Figures 6.8 and 6.9 exhibit several satellites that result from other effects. Typical is the appearance of metallic satellites (MS) or multiplet splittings from the exchange interaction (EX). The metallic satellites arise from plasmon losses or excitation of interband transitions. The spin-orbit splitting (Δ_{SO}), exchange splitting (Δ_{EX}), and metallic satellites (Δ_{MS}) were determined for selected core and semi-core levels and the results are summarized in Table 6.4.

Table 6.4: Core-level splittings in the Co_2MnGe spectra. Given are spin-orbit splitting Δ_{SO}, exchange splitting Δ_{EX} (subscripts 1 and 2 assign energies found from the fit using an additional spliting), and metallic satellites Δ_{MS} of selected core states of Co_2MnGe. All energies are given in eV.

	Co $2p$	Mn $2p$	Ge $3p$
Δ_{SO}	14.91	11.72	4.13
Δ_{EX1}	3.95	1.17	22.78
Δ_{EX2}	2.18	2.76	18.65
Δ_{MS}	7.70	0.95	—

Most interesting is that the Mn $3s$ state exhibits a well-distinguished exchange splitting

of $\Delta_{ex} = 4.68$ eV (see inset in Figure 6.9(b)). The intensity ratio between the main $3s$ line and the exchange-split satellite appears to be independent of the excitation energy. Such a splitting was not observed in previous work on Co_2MnSi [68]. In analogy to the Co $2p$ spectra, the Mn $2p$ core level shows $\Delta_{SO} = 12.1$ eV. Different from the Co $2p$ spectra, the multiplet splitting of the Mn $2p_{3/2}$ state is clearly revealed. The inset of Figure 6.8(b) demonstrates the occurrence of the multiplet splitting at the Mn $2p_{3/2}$ state by $\Delta_{EX} = 1.17$ eV. The splitting is too small to be resulted a metallic satellite. It was shown theoretically and experimentally for the case of Mn that the Coulomb interaction of the $2p$ core hole and the $3d$ valence electrons leads to the splitting of the Mn $2p_{3/2}$ level into several main sublevels [141] caused by the existence of more than one possible excited ionic state during ejection of electrons from the p core level. The splitting is less pronounced at the $2p_{1/2}$ state owing to the broadening of the line caused by a shorter lifetime of the hole in the $2p_{1/2}$ region compared to the $2p_{3/2}$ one.

In atoms, the multiplet splitting is due to the interaction of the nl^{-1} core hole with the polarized open valence shell. It is expected that the core hole (here $3s^1$ or $2p^5$) in solids interacts with the polarized d states of the valence band. Assuming that the atomic character of the valence electrons is—at least partially—retained in the solid one is able to use the well-known multiplet theory to explain the observed splittings in the spectrum [142, 143, 144, 145, 146].

Now, concentrating on the Mn atoms in Co_2MnGe, one sees that the description becomes complicated as it is not *a priori* clear what ionic state the Mn adopts in the metal. From the calculations (see Table 6.3) one has Mn d^5, neglecting all other shells. However, some of the d electrons are delocalized or screened in the metal and may not contribute to the coupling.

Assume a Mn^{2+} or Mn^{3+} ionic state with a ${}^6S_{5/2}$ or ${}^5D_4$ ground state in **LSJ** coupling. Note that the description of the ground states of neutral $Mn^0(4s^2 3d^5)$ and $Mn^{2+}(4s^0 3d^5)$ are principally the same because the filled $4s^2$ shell does not contribute. According to the dipole selection rules the following transitions take place for the various ground and excited states for excitation of ns core levels (here for the example of $3s$):

- from $3s^2 3d^5\ ({}^6S_{5/2})$
  to $\left\{\left[3s^1 3d^5\ ({}^{5,7}S_J)\right] + \epsilon(p)\right\}\ ({}^6P_{7/2,5/2,3/2})$,
- from $3s^2 3d^4\ ({}^5D_4)$
  to $\left\{\left[3s^1 3d^4\ ({}^{4,6}D_J)\right] + \epsilon(p)\right\}\ ({}^5P_{J'}, {}^5F_{J'})$,

or for np core levels (here for the example of $2p$):

- from $2p^6 3d^5\ ({}^6S_{5/2})$
  to $\left\{\left[2p^5 3d^5\ ({}^{5,7}P_J)\right] + \epsilon(s,d)\right\}\ ({}^6P_{7/2,5/2,3/2})$,
- from $2p^6 3d^4\ ({}^5D_4)$
  to $\left\{\left[2p^5 3d^4\ ({}^{4,6}F_J, {}^{4,6}P_J)\right] + \epsilon(s,d)\right\}\ ({}^5P_{J'}, {}^5F_{J'})$.

$\epsilon(p)$ or $\epsilon(s,d)$ denote the ejected electrons with kinetic energy ϵ_k and orbital angular momentum $l' = 1$ or $l' = 0, 2$ for ionization of the $3s$ or $2p$ shells, respectively. The final

total angular momentum related to the $^5D_4$ ground state can take the values $J' = 3$, 4, or 5. It is obvious that the intermediate ionic states always have spin values of $\mathbf{S}(d^5) = 5, 7$ or $\mathbf{S}(d^4) = 4, 6$. From this point of view, the splitting observed in emission from $3s$ or the two groups of transitions at the $2p$ may be assigned by the spin-exchange splitting of the ionic states. The remaining smaller splittings observed in emission from the $2p$ shell correspond to states with different total angular momentum J of the $^7P_{J=4,3,2}$ and $^5P_{J=3,2,1}$ intermediate ionic states for Mn^{2+} (or similar for the $^5D_4$ ground state of Mn^{3+}). For the $^6S_{5/2}$ ground state, in particular, $^7P_4$ corresponds to the ionic state with highest energy in the spectrum (the lowest final-state energy).

The observed intensity ratio of the two transitions at the Mn $3s$ state is 2.5, which is considerably larger than the expected 6:4 = 1.5 ratio for a Mn^{3+} d^4 ($^5D_4$) ground state (7:5 = 1.4 for d^5 ($^6S_{5/2}$)) when calculating it from the spin multiplicity ($2\mathbf{S}+1$) of the intermediate ionic states. Therefore, atomic type multiplet calculations were performed using de Groot's program CTM4XAS [147] to provide more details of the ionic state of Mn in Co_2MnGe. The details of the multiplet description and applied methods are found in Refs. [142, 145]. For the $3s$ excitation, the Slater integrals were scaled to 90% of their value from the Hartree-Fock calculations. The same reduction was used for the $2p$ excitation where the LS coupling parameter for the ground state was also scaled to 90%. A Lorentzian of 100 meV width for the lifetime broadening and a line broadening by Gaussians of 240 meV were used to account for the experimental resolution.

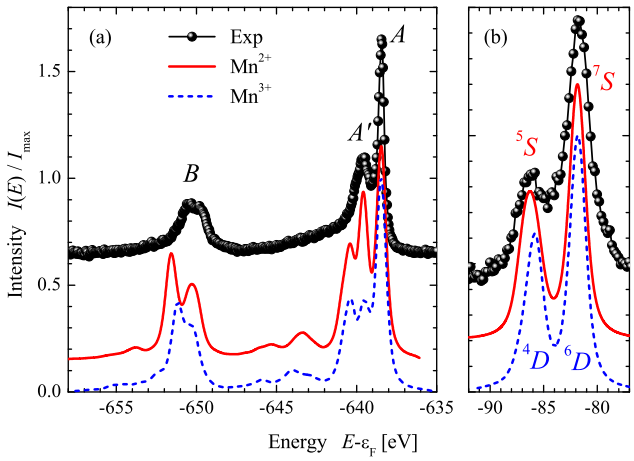

Figure 6.10: Comparison of the experimental and calculated core-level spectra of Mn in Co_2MnGe. The Mn$2p$ spectra are shown in (a) and $3s$ spectra in (b). The calculations were performed for d^5 and d^4 configurations of Mn, resulting in $^6S_{5/2}$ (full lines) and $^5D_4$ (dashed lines) ground states, respectively. In (a) the states A and B correspond in the single-particle picture to the spin-orbit-split $2p_{3/2}$ and $2p_{1/2}$ initial states. In the many-electron description the notation will depend on the assumed ground state (see text for details).

To understand the electronic state of Mn in Co_2MnGe, the photoemission spectra of

the $2p$ and $3s$ states for the Mn^{2+} as well Mn^{3+} were calculated and compared to the investigated high-energy photoelectron spectra. The results are shown in Figure 6.10. For Mn $3s$ the splitting of both the Mn^{2+} and Mn^{3+} ionic states fit the experimental data very well. Different lines of the underlying multiplet structure are not resolved. The calculated ^4D-^6D splitting of Mn^{3+} is slightly too small compared to the experimental value or to the ^5S-^7S splitting when assuming Mn^{2+}. In both cases the branching ratio does not fit the experiment. The situation is different for the $2p$ excitation where the splitting is not only determined by the Coulomb interaction but also by the spin-orbit interaction. By using the same scaling for the Slater integrals as for the $3s$ excitation, the main splitting between the multiplet components A and B at about -640 and -650 eV fits the experiment better when assuming a Mn^{3+} configuration. The details of the A-A' splitting of the spectrum at about -640 eV make clear that neither Mn^{2+} nor Mn^{3+} ionic states explain the spectra correctly. Comparing the intensities shows that the experimental spectrum is obviously between these cases. This means that one has either a mixture of d^4 and d^5 or, what is a more appropriate description for a metallic solid, a formal $d^{4.x}$ configuration with respect to the incomplete localization of the d electrons at the Mn site. This might be seen as contradicting the electronic structure calculations in which 5.1 d electrons are found at Mn (see Table 6.3). Above, the "size of Mn" was haphazardly set to touching spheres; if a sphere with a 15% smaller radius is chosen then one finds only 4.6 d electrons, without changing any other property of the electronic structure. One should be aware that, by taking this as the size of Mn in the solid, it becomes impossible to figure out the exact numbers of *localized* and *delocalized* electrons.

Valence-band spectroscopy

In the next step, the valence states of Co_2MnGe were investigated by photoelectron spectroscopy. Figure 6.11(b) compares the valence-band spectra of Co_2MnGe taken at low (20 K) and high (300 K) temperature at an excitation energy of about 6 keV. The changes in the spectra at different temperatures are unremarkable. The only effect is the expected broadening of the spectra and the slight smearing of the states at the Fermi edge caused by the change of the Fermi-Dirac distribution while going from 20 to 300 K. This observation is in accordance to the work on Co_2MnSi [68, 54] where also no temperature-dependent changes were detected.

Figure 6.11(a) compares the valence-band spectra taken with different photon energies of about 6 and 8 keV. The differences in the spectra are caused by the different weights of the partial photoionization cross sections for s, p, and d electrons at different excitation energies. With increasing energy the cross sections for d electron excitation decrease faster than those for s or p electrons (see Refs. [148, 149]). Therefore, the contribution from d electrons is more pronounced at lower energy.

The maximum of the emission from the a_{1g} states appears at -10.5 eV, which is about 1 eV lower compared to the calculated DOS. The maximum at about -3.9 eV corresponds to an excitation of the Mn t_{2g} minority states; its center is about 0.9 eV lower compared to the center of the states in the calculated DOS. The calculated site-

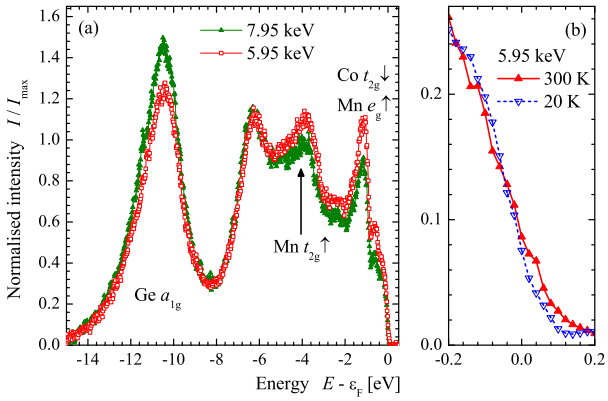

Figure 6.11: Valence-band spectra of Co_2MnGe (a) taken at 20 K excited by different photon energies (5.9468 and 7.9392 keV) and (b) in the vicinity of the Fermi energy at different temperatures ($h\nu = 5.9468$ keV).

resolved DOS exhibits pronounced Co and Mn e_g majority states as well as Co t_{2g} minority states at about -1 eV, where a strong maximum is observed in the spectrum. A pronounced influence of a correlation energy can thus be excluded, as proven by the small energy deviations between the experimental spectrum and calculated DOS. The observed energy shifts increase when moving further away from ϵ_F. This points clearly to lifetime effects: The holes at ϵ_F have a longer lifetime compared to those at lower energies. Accounting for the lifetime effects by increasing the imaginary part in the self-energy of the photoexcited electrons results in observed states that not only have an increased width when moving away from ϵ_F but also exhibit an increase of the energy shift. States that are farther away from ϵ_F are more strongly influenced because of the nonlinearity of the self-energy, being zero at ϵ_F and rising within a small energy range (a few eV) to its final value. It is concluded that the observed deviations between experiment and single-electron calculation are due to the photoemission process and are not related to an electron-electron interaction in the ground state.

6.2.5 Mechanical properties

In most cases only the electronic structure and magnetic properties of Heusler compounds are reported and used to compare theory and experiment. There are, however, other physical quantities available from the calculations and experiments that are important for later applications of the materials. Therefore, the mechanical, vibrational, and transport properties are reported in the following.

Table 6.5 compares the mechanical properties of Co_2MnSi and Co_2MnGe. The elastic constants were calculated by applying isotropic strain as well as volume-conserving tetragonal and rhombohedral strains to the optimized cubic primitive cell. The bulk modulus of the Si-containing compound is about 16% larger than that of the Ge-based compound. The elastic constants of both compounds follow the general inequality

$B > c_{44} > G > 0$, where B is the bulk modulus and G is Voigt's shear or rigidity modulus. Both A_e and the elastic stability criteria show that the compounds are stable in the cubic $L2_1$-type crystal structure.

Table 6.5: Mechanical properties of Co_2MnZ (Z = Si, Ge). Calculated bulk (B), Young's (E), and rigidity (G) moduli as well as the elastic constants c_{ij} are given in GPa; Poison's ratio (ν) and elastic anisotropy (A_e) are dimensionless quantities. Vickers hardness $HV1$ was measured with a load of 9.806 N and is given in kg/mm^2.

	Co_2MnSi	Co_2MnGe
c_{11}	290	250
c_{12}	179	180
c_{44}	158	132
B	216	203
G	104	77
E	269	206
ν	0.29	0.33
A_e	2.83	3.76
$HV1$	807 ± 14	741 ± 2

Figure 6.12 displays the three-dimensional distribution of the bulk (B), Young's (E), and rigidity (G) moduli of Co_2MnGe. (Those of Co_2MnSi are not shown, but they have a similar shape because of the close values of the elastic constants.) The bulk modulus is isotropic as mentioned above. By comparing the distribution of the remaining two moduli it is obvious that Young's modulus is largest in the $\langle 111 \rangle$-type directions whereas the rigidity modulus is largest in the $\langle 100 \rangle$-type directions, that is, along the cubic axes.

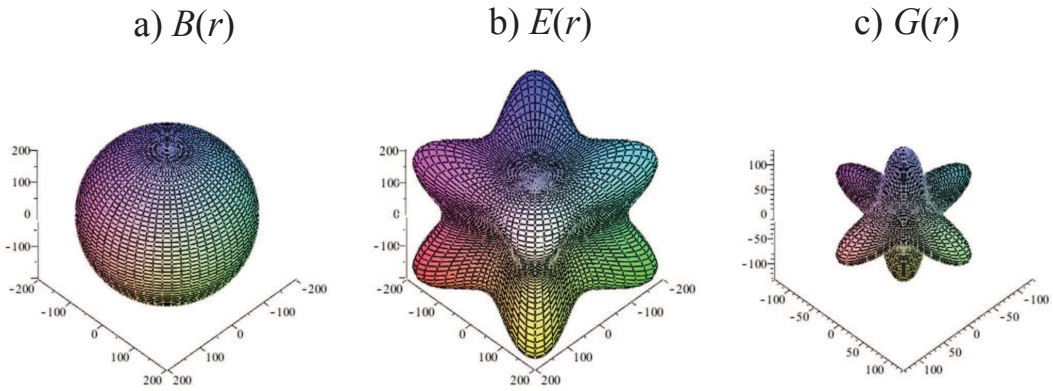

Figure 6.12: Calculated spatial distribution of the bulk (B), Young's (E), and rigidity (G) moduli of Co_2MnGe.

From the elastic constants, or say better the elastic moduli, one is able to calculate the speed of sound and Debye temperature Θ_D^{acc} in the approach given by Anderson [150].

For Co_2MnGe one finds in the acoustical approximation $\Theta_D^{\mathrm{acc}} = 554$ K from the values in Table 6.5.

The hardness (HV) was measured using a low-load Vickers hardness tester (Zwick, type Z3212). The load used to evaluate the Vickers micro-hardness ($HV1$) was $F = 9.806$ N ($P = 1$ kg). The Vickers hardness is determined from

$$HV = \frac{1.8544P}{d^2}, \tag{6.1}$$

where d is the diagonal length of the impression of the diamond probe (pyramid with apex angle = 135°). The Vickers hardness is not directly proportional to the elastic bulk modulus but indirectly depends on the elastic constants. The trend, however, is obvious: The Si-containing compound with higher bulk modulus also has a 8% higher hardness compared to the Ge-based compound.

The Chin-Gilman parameter $c_{\mathrm{CG}} = H/c_{44}$ is the ratio of the hardness number H to the shear modulus [151, 152]. For cubic crystals the latter is the elastic constant, c_{44}. Chin showed that it varies systematically with the type of chemical bonding in the crystals [153]. For cubic crystals the average values of metallic, ionic, or covalent systems are $c_{\mathrm{CG}}^{\mathrm{met}} = 0.006$, $c_{\mathrm{CG}}^{\mathrm{ion}} = 0.01$, or $c_{\mathrm{CG}}^{\mathrm{cov}} = 0.1$, respectively [154, 153]. The obtained values c_{CG} taken from measured hardness and calculated elastic constants for Co_2MnSi and Co_2MnGe are 0.05 and 0.06, respectively. These values prove that the type of bonding of the compounds is close to covalent.

6.2.6 Vibrational properties

The results of the phonon calculations are based on the spin-polarized electronic structure calculations. Figure 6.13 shows the calculated phonon dispersion $h\nu(q)$ and the accompanied density of states $g(\omega)$ of Co_2MnGe. The topmost, separate bands arise mainly from the optical modes related to the vibrations of the Ge atoms.

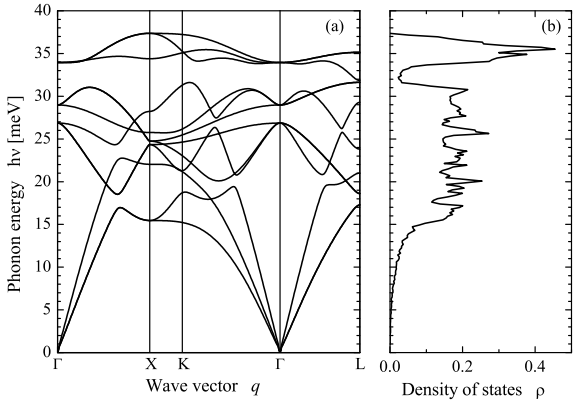

Figure 6.13: Phonons of Co_2MnGe. (a) Phonon dispersion and (b) corresponding density of states.

Figure 6.14 compares the temperature dependence of the calculated phonon $C_L(T)$ as well as the electron $C_e(T)$ part of the specific heat to the measured specific heat $C(T)$. Above 240 K the sum of $C_L(T)$ and $C_e(T)$ agrees well with the measured specific heat $C(T)$. The small differences between measured and calculated values at low temperature ($T < 100$ K) reveal that the specific heat is dominated by the phonon contribution. Deviations at higher temperature are caused by the fact that the measured C contains not only the lattice contribution but also contributions from electrons and magnons.

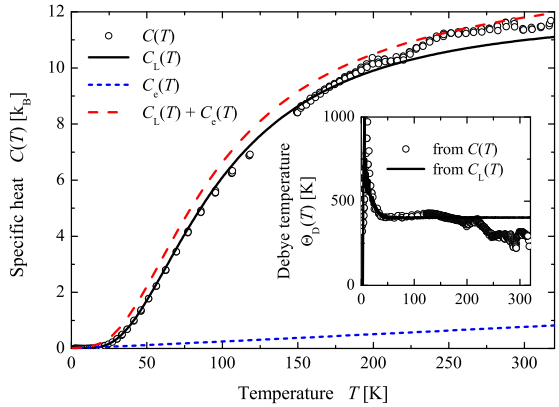

Figure 6.14: Specific heat of Co_2MnGe. $C(T)$ is the measured specific heat containing also electron and magnon contributions; $C_L(T)$ and $C_e(T)$ are the calculated lattice and electron specific heat, respectively. The inset shows the Debye temperature calculated from a fit to the $C(T)$ data.

The temperature-dependent heat capacity is expressed according to a suggestion from Ref. [155] as a polynomial sum [Eq. 3]. A fit of the data in the low-temperature range to

$$C(T) = A \cdot T^{-2} + \gamma \cdot T + \beta \cdot T^3 \tag{6.2}$$

results in values of $A = (35.15 \pm 0.06)$ mJ K/mol, $\gamma = (23.2 \pm 1.4)$ mJ/(mol K^2), and $\beta = (1.46 \pm 0.03)$ μJ/(mol K^4). The Debye temperature Θ_D is found by fitting the measured or calculated specific heat to the Debye model. The result is shown in the inset of Figure 6.14. The Debye temperature calculated from $C_L(T)$ is $\Theta_D = 403$ K in the high-temperature limit ($T > 50$ K). The temperature dependence of Θ_D calculated from the measured specific heat $C(T)$ does not clearly approach the high-temperature limit, which is mainly due to experimental uncertainties as well as the increasing influence of the electron and magnon specific heats at higher temperatures. The Debye temperature derived from the specific heat is lower compared to the acoustic value derived from the elastic constants ($\Theta_D < \Theta_D^{\mathrm{acc}}$; see above), pointing to the influence of the high-lying optical modes.

The calculated thermal displacements $\langle u^2 \rangle$ at 300 K are 4.2×10^{-3}, 4.1×10^{-3}, and 3.9×10^{-3} Å^2 for Co, Mn, and Ge, respectively. The average value of 4.06×10^{-3} Å^2 is about half of the average Debye-Waller factor $\sigma^2/2 = 3.9 \times 10^{-3}$ Å^2 found in the

EXAFS measurements (see Table 6.2). The values of the mean square displacement and the Debye-Waller factor depend on the underlying model and the factor of about 2 between $\langle u^2 \rangle$ and σ^2 is explained in detail in Ref. [156].

6.2.7 Transport properties

The measured transport properties of Co_2MnGe are summarized in Figure 6.15. The electrical resistivity $\rho(T)$ data from 5 to 300 K were obtained by a standard linear four-point contact method. The results shown in Figure 6.15(a) exhibit a regular metallic behavior. The inset shows the resistivity as a function of temperature on a logarithmic scale. Below 50 K the resistivity becomes 0.27 $\mu\Omega\,\mathrm{m}$, nearly independent of temperature, while above this value the resistance increases with increasing temperature. The temperature-independent part at low temperatures was suggested to be typical for half-metallic ferromagnets [157, 158]. The residual resistivity ratio is $R_{RR} = \rho(300\,\mathrm{K})/\rho(2\,\mathrm{K}) = 1.8$. This value is small compared to other polycrystalline Heusler compounds. The overall low values of the resistivity are also remarkable, being a factor of 100 smaller compared to those of polycrystalline Co_2MnSi samples that were produced in the same way (from data not shown here). Both together point to the high quality of the Co_2MnGe samples.

Figure 6.15(b) shows the temperature-dependent thermal conductivity $\kappa(T)$ of Co_2MnGe. At low temperatures, $\kappa(T)$ increases with a T^3 law and a maximum appears between 40 and 50 K. Above 100 K, $\kappa(T)$ increases linearly with temperature. This behavior arises from the large electronic component of the total thermal conductivity in metals [41].

The Seebeck coefficient $S(T)$ (see Figure 6.15(c)) is negative in the entire temperature range. Similar to $\rho(T)$, the absolute value is almost constant below 50 K, as shown using a logarithmic scale in the inset of Figure 6.15(c), and increases with increasing temperature. The value of $-16\ \mu\mathrm{V\,K^{-1}}$ at 300 K is comparable to that of elemental metals Co ($-30.8\ \mu\mathrm{V\,K^{-1}}$) and Mn ($-9.8\ \mu\mathrm{V\,K^{-1}}$). Similar values are observed in other polycrystalline Heusler compounds [159]. $S(T)$ was calculated from the electronic structure using a modified version [106] of BOLTZTRAP [104] and compared to the experiment as shown in Figure 6.15(c). The measured value agrees well with the calculated one. Deviations are seen at low temperatures where one expects the largest influence of the phonon-drag effect at about 0.2 times the Debye temperature [160], which here is at about 80 K. At elevated temperatures the electronic structure starts to deviate from that of the ground-state half-metallic ferromagnet and minority and majority states start to mix owing to the thermal fluctuations already below the Curie temperature. This explains the deviations between measured and calculated $S(T)$ at higher temperatures.

6.3 Summary

In summary, the structural, electronic, magnetic, mechanical, and transport properties of the half-metallic ferromagnet Co_2MnGe have been studied in detail. The crystalline structure of Co_2MnGe was investigated by XRD, EXAFS, and anomalous XRD and

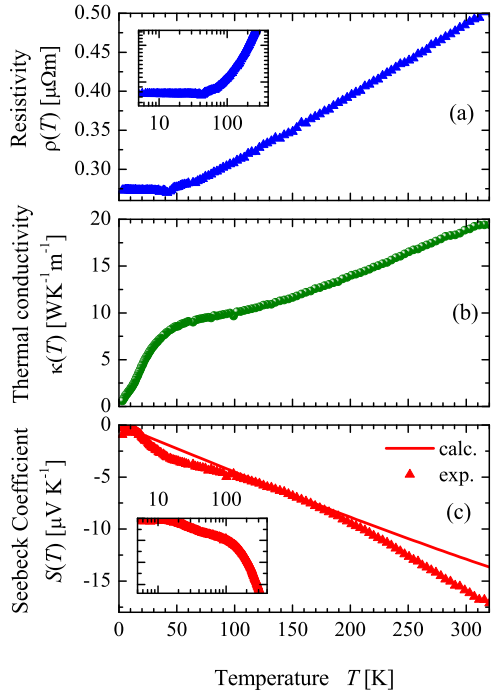

Figure 6.15: Temperature dependence of the transport properties of Co_2MnGe. Shown are (a) the electrical resistivity $\rho(T)$, (b) the thermal conductivity $\kappa(T)$, and (c) the calculated and experimental Seebeck coefficient $S(T)$.

it was found that the compound exhibits the $L2_1$ structure typical for well-ordered Heusler compounds. The vibrational and mechanical properties of the compound were calculated. The comparison of observed and calculated mechanical properties proves a covalent-like bonding of Co_2MnGe. Band-structure calculations based on the $L2_1$ structure result in a half-metallic ferromagnetic ground state for the compound. The compound is a localized magnetic moment system with a ground-state magnetic moment of $5\mu_B$ in the primitive cell. This is in excellent agreement to the SQUID measurement, which revealed a magnetic moment of $4.982\mu_B$ at 5 K. Thus, Co_2MnGe fulfills the requirement for half-metallicity according to the Slater-Pauling rule. The transport measurements show the expected metallic behavior with a resistivity of 0.48 $\mu\Omega\,\mathrm{m}$ and a Seebeck coefficient of $-16\ \mu\mathrm{V\,K^{-1}}$ at room temperature. The temperature independence of the resistivity below 50 K supports the occurrence of half-metallic ferromagnetism in this compound. The bulk sensitivity of HAXPES was used to explore the core levels as well as the valence-band electronic structure of polycrystalline Co_2MnGe. The measured valence-band spectra are clearly resolved and in good agreement with the first-principles calculations of the electronic structure. Spin-orbit splitting and exchange splitting of the core levels are explored in detail. Multiplet calculations of $2p$ and $3s$ core levels were performed for Mn in 2+ and 3+ ionic states to determine the importance of the

many-electron contributions to the core-level photoelectron spectra of the compound. Comparison of the calculation to the experiment revealed that the state of Mn cannot be identified as being a definite ionic one. This is expected for metallic compounds.

7 NiTiSn Based Heusler Compounds for Thermoelectric Application

7.1 Introduction

The development of highly efficient thermoelectric (TE) materials is important for energy generation, refrigeration and energy storage technologies. The efficiency of a TE device is determined by the materials used to build the device [36]. Presently, the world market for TE devices is still small, caused by their low efficiencies, which is limited by high cost (e.g.: SiGe alloys), significant toxicity (e.g.: Bismuth or Thallium chalcogenides), and stability at the operation temperatures. The Heusler compounds with 1:1:1 composition crystallize in the cubic MgAgAs-type structure ($F\,\bar{4}3m$, $C1_b$) [31, 32]. Their excellent potential as materials for high temperature power generation was demonstrated in the past [42]. Advantages are their environmentally friendly constituents, easy synthesis, and chemical stability (high melting points) [43] as well as good reproductibility. The compounds of the general formula NiMSn (M = Ti, Zr, Hf) have 18 valence electrons. They were reported to exhibit unusual transport and optical properties because of the band gap or pseudo-gap at the Fermi energy. The NiMSn (M = Ti, Zr, Hf) system shows some promise for *n-type* TE materials, due to the large Seebeck coefficients and high electrical conductivity [42, 161]. Sakurada and Shutoh reported a high figure of merit of 1.5 at 700 K for Sb-doped $NiTi_{0.50}Zr_{0.25}Hf_{.25}Sn$ [47, 162], which is one of the highest values for Heusler compounds at that temperature. A variety of substitutions in NiMSn with other main-group metals as well as transition metals have been made for further optimization of the thermoelectric performance [36]. For example, doping on the M and Ni sites causes mass fluctuation disorder that may lead to a reduction of thermal conductivity [162, 163, 164, 165], while doping on the Sn site provides charge carriers [165, 166]. Numerous Heusler alloys have been investigated focusing on their high-temperature thermoelectric properties. The majority of these compounds are n-type thermoelectric materials. On the other hand, efficient p-type materials based on Heusler compounds that operate at high temperatures are rare. However, few studies have been reported on thermoelectric properties of p-type Heusler compounds [167, 168].

In order to achieve the best performance of thermoelectric modules the n- and p-type materials to be used should be designed to exhibit similar chemical and physical properties [41]. This can be easily realized when starting from the same material, here the Heusler compound NiTiSn. Yang and coworkers evaluated theoretically the thermoelectric-related electrical transport properties of several Heusler compounds, they calculated the maximum power factors and the corresponding optimal n- or p-type doping levels [49], which can provide guidance to experimental work. Horyn and coworkers investigated the effect of a partial substitution of Ti and Zr by Sc on the thermoelectric properties of NiMSn-based compounds and obtained at room temperature a fairly high positive Seebeck coefficient of about 121 μV/K with 5% Sc substitution of Zr [169].

Miyamoto and coworkers studied the electronic structures of the Heusler compounds NiMSn by means of photoelectron spectroscopy [50]. They observed "in gap" states close to the Fermi edge and suggested that these electronic states are mainly created by chemical disorder, which could be the key to control the thermoelectric properties.

In the commonly used one-parabolic-band approaches n- or p-type doping lead to rather similar results, just with opposite signs for the Seebeck coefficient. The situation in practical materials is more difficult. Depleting the valence or filling the conduction band acts on electronic states with rather different characters. It will be shown that the effect of doping shows a completely different impact for the NiTiSn compounds when comparing n- and p- type substitution. To explain the different effect on the conductivity a new approach is used that combines the coherent potential approximation and calculation of the impurity scattering resistivity for the multielement case.

In this chapter, electronic structure and transport properties of the series $NiTi_{1-x}M_xSn$ (where M = Sc, V and $0 < x \leq 0.2$) were calculated by ab-initio methods. The series was synthesized and the structure was determined by X-ray diffraction (XRD). The transport properties were investigated and the results are compared to the calculated properties. Hard X-ray photoelectron spectroscopy (HAXPES) was performed on the compounds to experimentally determine the valence states and to compare them to the calculated electronic structure.

Furthermore, the effect of Ti substitution by Sc on the thermoelectric properties of the Heusler compounds $NiTi_{0.3-x}Sc_xZr_{0.35}Hf_{0.35}Sn$ (where $0 < x \leq 0.05$) was investigated. The electronic structure was investigated by means of HAXPES.

7.2 Electronic Transport Properties of Electron and Hole Doped, Semiconducting $C1_b$ Heusler Compounds: $NiTi_{1-x}M_xSn$ (M = Sc, V)

7.2.1 Electronic structure and calculated transport properties

Figure 7.1 shows the calculated band structure and the density of states of NiTiSn. The compound is a semiconductor with an indirect gap. The valence band maximum appears at Γ and the conduction band minimum at X. The band gap has a size of $\Delta E_{\text{gap}} = 0.45$ eV. The optical gap at Γ is considerably larger ($\Delta E_\Gamma = 1.38$ eV).

The electronic structure exhibits at 5 eV to 8 eV below the Fermi energy the typical sp hybridization gap that separates the low lying a_1 (s) from the t_1 (p) bands. The high density of states at about -2 eV emerges mainly from Ni d states. The high density of states at -0.7 eV arises mainly from Ni d states with e symmetry. Most important for the transport properties, the states at both band edges are due to Ti d states with t_2 symmetry. From the band structure shown in Figure 7.1 it is obvious that electron (n) or hole (p) doping will have rather different results. It is easily seen that p-type doping creates holes in the triply degenerate valence band at Γ whereas the situation is completely different for n-type doping that fills electrons into the single conduction band above the indirect gap at X.

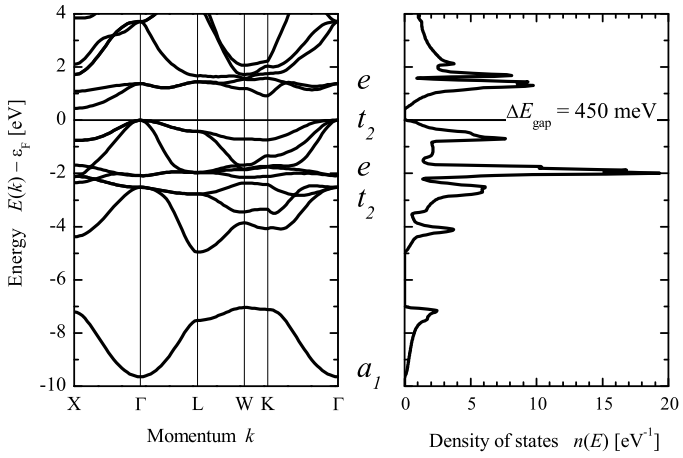

Figure 7.1: Electronic structure of NiTiSn.
The irreducible representations of the states at the Γ point are given for the T_d point group.

Starting from the calculated electronic structure, the transport properties were calculated using Boltzmann transport theory [160]. Doping the semiconducting materials by electrons or holes will change the transport properties. The doping will cause the chemical potential to change its position. At high doping levels it will shift into the valence (hole doping) or conduction (electron doping) band. Figure 7.2 shows the calculated Seebeck and power coefficients as function of the position of the chemical potential. The calculations were performed for $T = 300$ K. It is assumed that the shift $\delta\mu = 0$ corresponds to the middle of the band gap at $T = 0$. In References [170, 171] the calculated Boltzmann transport quantities were reported as a function of the chemical potential and temperature for much higher doping level using the same method. The results agree with the here reported values for low doping that close the gap in the considered range of substitution. The Seebeck coefficient exhibits the typical semiconductor behavior under doping, it is positive for hole and negative for electron doping. It is largest for small shifts of the chemical potential from the original position. At 300 K it is already slightly positive in the middle of the band gap. the reason is the shift of the chemical potential with temperature $\mu = \mu(T)$ to ensure charge neutrality of the system when no voltage is applied. At 300 K the shift amounts to $\delta\mu \approx 13$ meV. The size and direction of the shift depends on the shape of the valence and conduction bands.

Figure 7.3 shows the temperature dependence of the chemical potential and its effect on the Seebeck coefficient of the undoped material. $\delta\mu$ was also calculated for low electron or hole doping (10^{-6}, 10^{-3}) with hypothetical impurity states located close to the band edges (±50 meV). It is seen that the chemical potential is pinned at the impurity states at very low temperature. In the high temperature limit the chemical potential goes over into the one of the pure semiconductor, depending on the degree of doping.

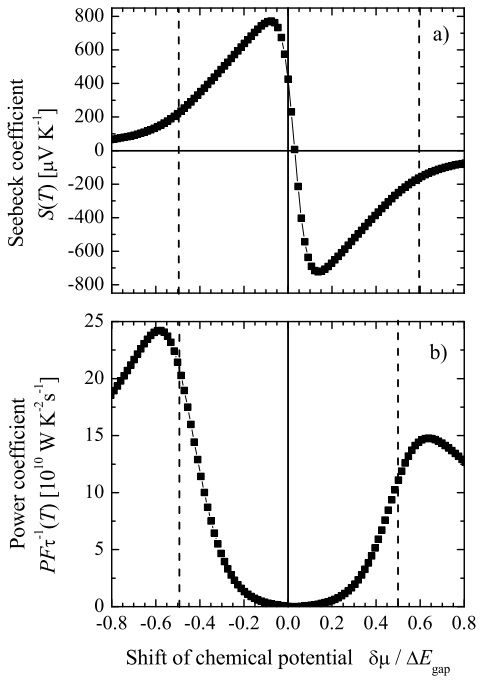

Figure 7.2: Calculated Seebeck and power coefficients of NiTiSn. The shift of the chemical potential is given with respect to the size of the gap. The valence and conduction band extrema are marked by dashed lines. ($T = 300$ K)

For applications, the power factor $PF = S^2\sigma$ is more interesting than the Seebeck coefficient alone. The power coefficient, as shown in Figure 7.2(b), is defined here by the power factor divided by the relaxation time τ. The reason for this is that the calculations deliver σ/τ rather than directly the pure conductivity. The largest power coefficient appears for hole doping when the chemical potential is already shifted slightly outside of the band gap into the valence band. The maximum for electron doping is smaller and also appears when μ is slightly shifted outside of the gap. The reason for this is in both cases the high conductivity when the compound goes over into the completely metallic state. From the integrated density of states it is estimated that the maxima of the power coefficient are reached at an electron or hole doping of about 1.1% or 1.4%, respectively.

Substituting Ti by V or Sc will act as electron or hole doping, respectively. The difference in the number of valence electrons is in both cases one, such that a substitution by an amount x changes the electron concentration also by $\pm x$. At high substitution levels in the order of several per cent it is, however, not clear *a priori* that the electronic structure stays unchanged and only the chemical potential or Fermi energy is shifted. Therefore, the electronic structure was also calculated for substituted compounds using values up to $x = 0.2$.

The density of states of $M =$ Sc or V substituted $NiTi_{1-x}M_xSn$ is shown in Figure 7.4.

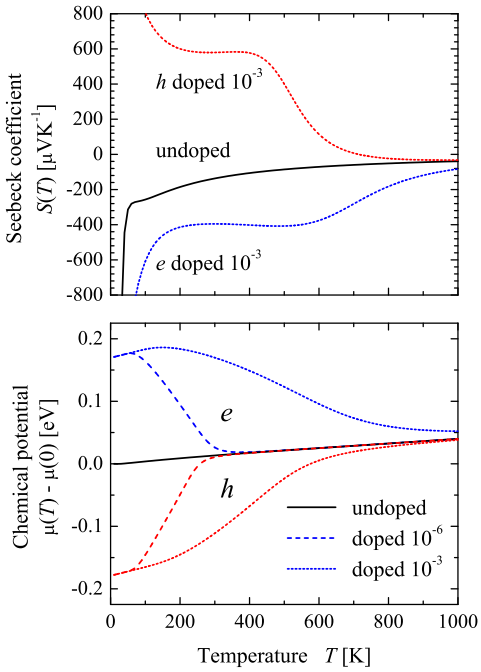

Figure 7.3: Seebeck coefficient and chemical potential of NiTiSn.
The shift of the chemical potential was calculated for pure as well as electron and hole doped NiTiSn (e and h assign electron and hole doping, respectively).

The band gap is conserved upon substitution up to the 20 % level for both elements, Sc and V. Overall, the shape of the density of states stays rather unaffected up to $x = 0.2$. The main effect of the substitution is the shift of the Fermi energy such that the compound becomes metallic. Other than in the earlier studies on Fe substituted $CoTi_{1-x}M'_xSb$ (M' = Mn, Fe) [172, 173] a magnetic ground state was not found by the calculations. One reason might be the much higher electron concentration (4 per substituted Fe) compared to the case studied here or the strong tendency of Mn to form localized moments.

7.2.2 Structure properties

Based on the theoretical findings, the series $NiTi_{1-x}M_xSn$ (M = Sc, V) was synthesized as described above. The crystal structure of the samples was investigated by X-ray powder diffraction (XRD) using excitation by Mo K_α radiation. Figure 7.5 shows the obtained diffraction pattern of the compound NiTiSn as an example. All compounds exhibit the $C1_b$ structure. The Rietveld refinement for a disorder of 5% swapped Ti to the vacant position (Vc) delivered the lowest R values. The difference to the measured data is shown in Figure 7.5. The refinement of the data resulted in a lattice parameter

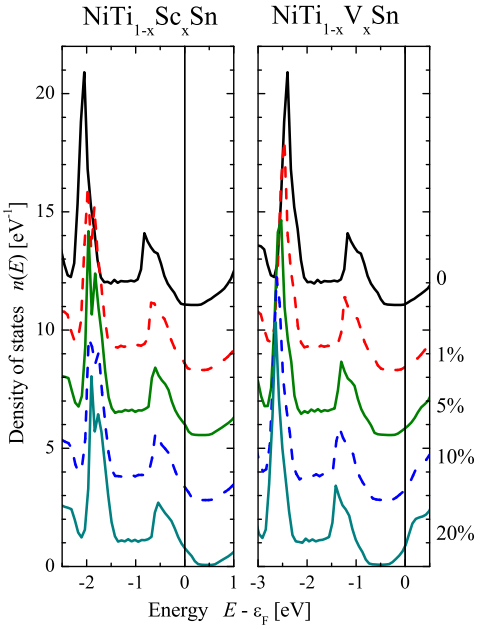

Figure 7.4: Density of states of M = Sc and V substituted $NiTi_{1-x}M_xSn$. For better comparison, the Fermi energy (ϵ_F) of the pure NiTiSn was set to the valence band maximum in the case of Sc substitution and to the conduction band minimum for V substitution.

of $a = 5.9185$ Å for pure NiTiSn. This value agrees with the values found in literature [174, 162]. The inset in Figure 7.5 shows a monotonic increase of the lattice parameter of $NiTi_{1-x}Sc_xSn$ with increase of the scandium content. A linear regression gives a slope of $\Delta a = x \times 2.54 \times 10^{-3}$ Å. This increase is caused when replacing the Ti atoms of smaller size ($r_{\mathrm{Ti}} = 1.36$ Å) by the larger Sc atoms ($r_{\mathrm{Sc}} = 1.44$ Å). The dependence of the lattice parameter of the V ($r_{\mathrm{V}} = 1.25$ Å) substituted compounds exhibits only a very low decrease (not shown here).

7.2.3 Hard X-ray photoelectron spectroscopy

The electronic structure of the series $NiTi_{1-x}Sc_xSn$ was investigated by HAXPES. Figure 7.6 compares the measured valence band spectra of NiTiSn to the Sc substituted compounds $NiTi_{1-x}Sc_xSn$. The spectra were taken at 20 K with an excitation energy of about 7.9 keV. The low lying a_1 (s) states are revealed below -7.5 eV as well as the sp hybridization gap being typical for Heusler compounds. The higher lying valence band spectrum of NiTiSn shows clearly a structure with four major peaks at energies of about -1.3 eV, -2.3 eV, -3.1 eV, and -4.9 eV below the Fermi energy (ϵ_F) that are associated with p and d states, in agreement to the calculated density of states. Compared to the electronic structure calculations the peaks arise mainly from t_2 (p) states (-4.9 eV), t_2

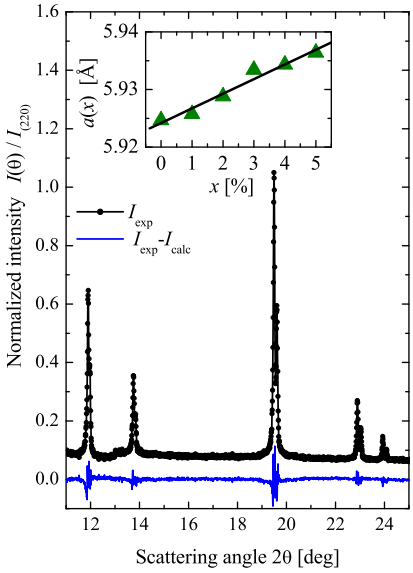

Figure 7.5: X-ray diffraction of polycrystalline NiTiSn.
The data were taken at room temperature using Mo K_α radiation. The inset shows the dependence of lattice parameter a for $NiTi_{1-x}Sc_xSn$ versus Sc content. The line is a result of a linear fit to Vegards law.

states (-3.1 eV) as well as unresolved e and t_2 states (-2.3 eV) located at the Ni atoms, and of different d states located at Ni and Ti (-1.3 eV). The states with different symmetry character are not resolved in the spectra. Similar structures are also observed for the Sc substituted compounds. A remarkable shift of the peaks towards the Fermi edge is obtained with increase of the Sc content. It is explained by the depletion of states in the valence band when substituting Ti ($3d^24s^2$) by Sc ($3d^14s^2$). As a fact, the Fermi energy is lowered or - equivalently - the bands move towards ϵ_F that is here the reference energy.

Figure 7.7 compares the valence band spectra close to the Fermi energy that were taken with a higher energy resolution. For the pure NiTiSn compound one observes typical *"in gap"* states. These states were previously suggested to be responsible for the excellent thermoelectric properties of such compounds [50], and make the pure compound metallic as shown in the calculations. The shape of the observed *"in gap"* states corresponds well to the assumption of a Ti↔vacancy swap as will be discussed below. The area of the in-gap states is about 0.5% of the overall valence band spectrum. Assuming constant and equal cross sections for all states this would correspond to about 0.1 electrons only. Figure 7.7 reveals also the shift of the states towards ϵ_F while increasing the amount of Sc. The observed shift is not linear for two reasons. The Sc substitution does not decrease linearly the numbers of states at ϵ_F (see inset in Figure 7.11a) and moreover it suppresses the in-gap states.

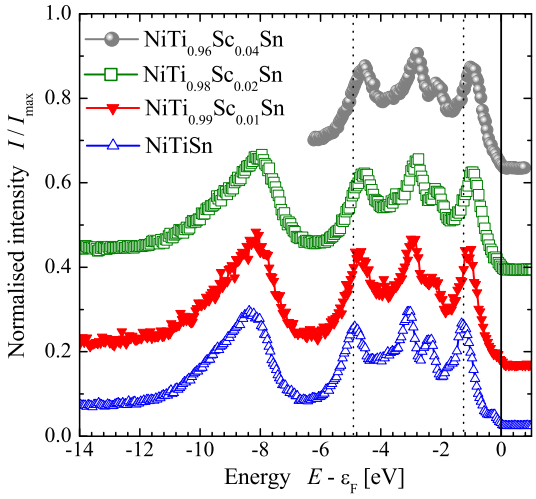

Figure 7.6: Valence band spectra of $NiTi_{1-x}Sc_xSn$ (x= 0, 0.01, 0.02, and 0.04). The measurements were performed at 20 K, the excitation energy was fixed to 7.939 keV .

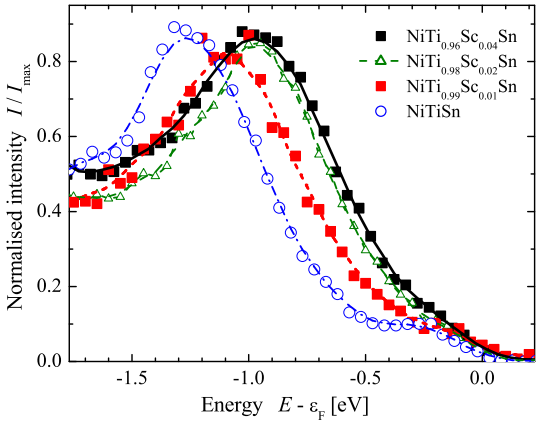

Figure 7.7: Valence band spectra of $NiTi_{1-x}Sc_xSn$ close to the Fermi edge ϵ_F for an excitation energy of 7.939 keV and an improved, higher resolution (ΔE = 150 meV) compared to Figure 7.6.

As found by powder XRD, the pure NiTiSn tends to anti-site disorder with Ti swapped into the vacant position of the $C1_b$ lattice. The KKR method in conjunction with coherent potential approximation was used to investigate the changes of the electronic structure for different types of disorder. Figure 7.8 compares the consequences of different types of disorder on the density of states. Assumed is a swapping of the atoms from

their regular sites to the vacant position (Vc) of the $C1_b$ structure without changing the overall composition. States appear in the band gap and NiTiSn becomes metallic in all three cases already if 1% of the atoms is exchanged with the vacancy. The details of the changes of the density of states inside of the initial band gap are rather different for the three types of atoms. For Ni an additional state appears at ϵ_F close to the middle of the original gap whereas several states are obtained for Sn. In all three cases the total energy (about 17.1×10^3 Ry) of the system becomes slightly higher with the disorder and increases with the amount of disorder (assuming an unchanged lattice parameter). For Ni↔Vc the energy of the disordered state is about 0.5 Ry higher at a disorder level of 1% (2.5 Ry at 5%). Therefore, this type of disorder becomes very improbable. The situation is different for Ti↔Vc that raises the total energy only by about 5 mRy at 1% disorder. The Ti swap causes two impurity states at about -0.2 eV and +0.1 eV with respect to ϵ_F. At the low disorder level the occupied state contains about 0.03 electrons (≈ 0.15 electrons at 5%). This type of disorder is thus consistent with the observations by XRD as well as photoelectron spectroscopy. It leads to a self-doping in the compound and finally in a high n-type Seebeck coefficient as will be shown in the following.

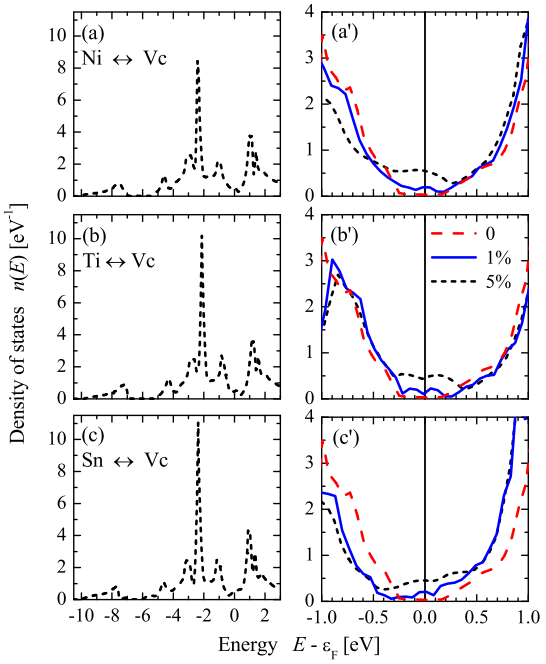

Figure 7.8: Density of states of disordered NiTiSn. The left panel (a)-(c) show the density of states for 5% of the atoms swapped into the vacant site (Vc). The right panel (a')-(c') compare the part around the Fermi energy for different amount of disorder to the well ordered compound. The Fermi energy (ϵ_F) of ordered NiTiSn was placed in the middle of the band gap for better comparison.

Independent of the type of disorder, the *"in gap"* states always make the compound metallic. It is worthwhile to note that similar impurity states will appear if the substituted elements occupy the vacant sites instead of the original Ti position. The situation becomes more complicated because the number of valence electrons is changed at the same time.

7.2.4 Transport properties

The measured temperature dependence of the transport properties for different types of substitution (Sc, V) are shown in Figure 7.9 for three exemplary cases. Figure 7.9 compares the temperature dependence of electrical conductivity $\sigma(T)$, thermal conductivity $\kappa(T)$, and Seebeck coefficient $S(T)$ of pure NiTiSn to the substituted compounds $NiTi_{0.97}Sc_{0.03}Sn$ and $NiTi_{0.97}V_{0.03}Sn$. The pure compound does not exhibit a clear semiconducting behavior what is expected from the occurrence of the in-gap states reported above. Substituting Ti by V makes the compound metallic with a typical decreased electrical conductivity by increasing of the temperature. On the other hand, the values of the electrical conductivity is changed by more than one order of magnitude in comparison with that of the non-doped compound. It stays increasing with temperature under Sc substitution, what gives another hint on the suppression of the "in gap" states. The

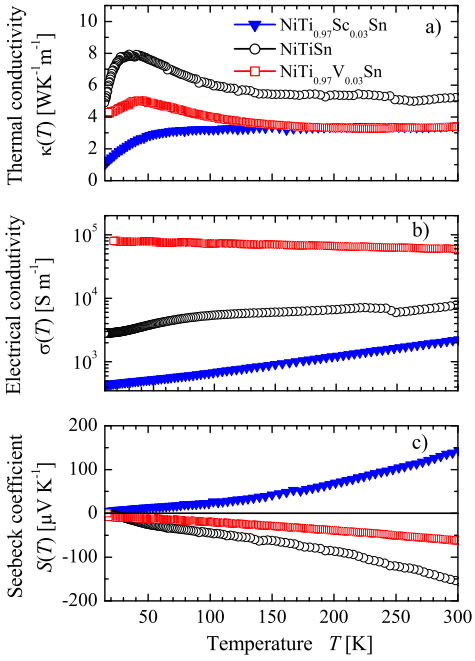

Figure 7.9: Temperature dependence of thermal conductivity $\kappa(T)$, electrical conductivity $\sigma(T)$,and Seebeck coefficient $S(T)$ of NiTiSn and $NiTi_{0.97}M_{0.03}Sn$ (M = Sc, V).

thermal conductivity $\kappa(T)$ of NiTiSn exhibits a maximum at about 30 K that is typical for well ordered compounds. Substituting Ti by Sc or V results in a considerably lower thermal conductivity and in the case of Sc to a full suppression of the maximum. The decrease of $\kappa(T)$ is explained by scattering of electrons and phonons at the substituted atoms that act as impurities even though they occupy regular lattice sites. At higher temperatures, the thermal conductivity of both substituted compounds becomes nearly equal what points to similar scattering processes.

The Seebeck coefficient is already n-type in the pure compound. It stays negative, as expected, but its absolute value becomes smaller when substituting Ti by V. When substituting Ti by Sc the Seebeck coefficient reverses the sign such that the compound becomes p-type in full agreement with the expectations from the calculations. Most interestingly, the Seebeck coefficient changes the sign at 300 K from -155 μV/K for the undoped compound to +140 μV/K for the compound with 3% Sc substitution.

Figure 7.10 compares the behavior of the measured transport properties as function of the substitution of Ti by Sc (Fig. 7.10a) or V (Fig. 7.10b) at fixed temperatures (100 K, 300 K). The data for high Sc substitution with $x \geq 5\%$ reported by Romaka and co-worker [175] continue seamless the low substitution results reported here. The general variation and changes of the transport properties agree qualitatively with the calculated transport coefficients using Boltzmann transport theory (see above). Neglecting the differences observed for the pure NiTiSn compound that are caused by in-gap states, the sign and occurrence of maxima (minima) of the Seebeck coefficient are in agreement to a simple doping electrons or holes model as given in Figure 7.2. The sign of the Seebeck coefficient for NiTiSn is negative and changes to positive with increasing the substitution ratio on Sc. Since the number of valence electrons of Sc is one less than that of Ti, Sc acts as a hole donor, and the number of hole carries increases. The absolute value of the Seebeck coefficient decreases with increasing amount of V. The electron-doping increases the density of states at ϵ_F due to the Fermi-level shift to a higher position in the conduction band (Figure 7.4). As a result, the Seebeck coefficient decreases with V concentration. The behavior agrees roughly with the result of the Boltzmann transport calculations (see Figure 7.2). Details of the observed transport properties are different from those found from Boltzmann transport equations because the latter do not contain detailed information about the relaxation times. Therefore, the residual resistivities of the substituted compounds were also calculated by means of the KKR-CPA method. The behavior of the residual resistivity due to chemical disorder is different when substituting Ti by Sc or V. In Figure 7.11 the calculated conductivity $\sigma = 1/\rho$ is shown that allows a better estimation of its influence on the power factor that depends linearly on σ but is inversely proportional to ρ. Compared is the calculated conductivity $\sigma(x)$ as a function of the substitution level x. The shift of the Fermi energy into the valence or conduction band (see Figure 7.4) makes the compound metallic. The resulting increase of the density of states at the Fermi energy is obvious from the insets in Figure 7.11. Its progression is different for Sc or V because of the differences in the valence or conduction bands, respectively. The results for Sc substitution agree well with those reported by Stopa and co-worker [176]. The conductivity behaves quite different for the two kinds of substitution, even though the general increase of $n(\epsilon_F, x)$ is rather

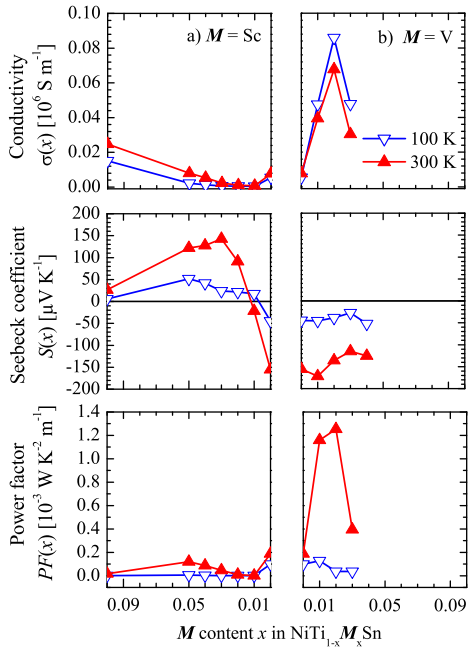

Figure 7.10: Dependence of the electric conductivity $\sigma(x)$, Seebeck coefficient $S(x)$, and power factor $PF(x)$ on the electron and hole doping of $NiTi_{1-x}M_xSn$ (M = Sc, V).

similar without large differences in its magnitude (see insets in Figure 7.11). For the case of Ti substitution by Sc, $\sigma(x)$ reflects directly the increase of the number of electrons that take part in the transport properties. The initial increase of $\sigma(x)$ is much more pronounced for V caused by the different character of the conduction band compared to the valence band (see also Figure 7.1), already at 0.2% substitution the compound becomes metallic. The conductivity exhibits a maximum at about 1% substitution of Ti by V. The following decrease of $\sigma(x)$ is explained by the increase of chemical disorder scattering at the V atoms. In contrast to Sc substitution, the increase of the V impurity scattering is not compensated by the increase of $n(\epsilon_F, x)$ with increasing x.

The details reveal that a simple shift of the chemical potential is not able to explain the measured data. For the power factor that does contain the scattering rates, this is easily understandable. Obviously, the calculation of the Seebeck coefficient needs also the inclusion of different scattering rates for different bands rather than a single, fixed relaxation time. The differences between Sc and V type substitution are obvious from the band structure of the pure NiTiSn compound. From Figure 7.1 it is easily seen that p-type doping (Sc) creates holes in the triply degenerate (at Γ) topmost valence band. The situation is completely different for n-type doping (V) where only the single state of the lowest conduction band above the indirect gap at X is filled by electrons. The difference in the relaxation times for electrons in the various involved bands together

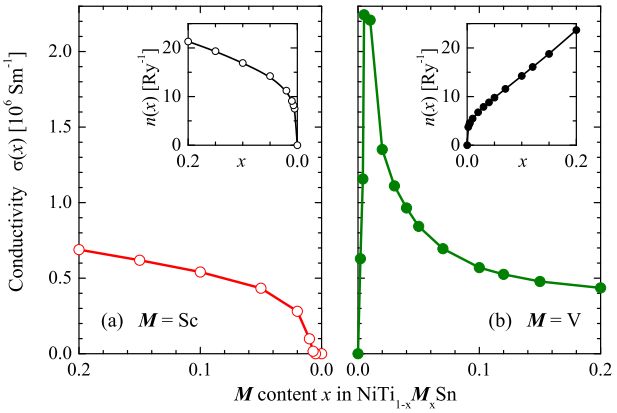

Figure 7.11: Calculated conductivity of M = Sc and V substituted $NiTi_{1-x}M_xSn$. (a) shows the results of Sc↔Ti and (b) of V↔Ti substitution corresponding to hole or electron doping, respectively. The insets show the density of states $n(\epsilon_F, x)$ at the Fermi energy as function of the substitution. The density of states was broadened by a Lorentzian to reduce the numerical noise.

with the different character of those bands have finally the effect that the behavior of the power factor does not agree with the prediction shown in Figure 7.2.

The measured conductivity agrees well with the Kubo-Greenwood-type calculations that account for chemical disorder, not only qualitatively but also quantitatively if keeping in mind that the calculated values represent the residual resistivity for 0 K. Obviously the disorder scattering causes completely different results if the electrons responsible for the transport are from the *"initial valence"* band for Sc substitution or the *"initial conduction"* band for V substitution. The behavior of the conductivity has a major impact on the behavior of the power factor under substitution. The highest value is observed for the n-type V substitution and the p-type Sc substitution leads to considerably lower power factors. Indeed, the difference arises from the different behavior of the conductivity for both types of substitution. It is worthwhile to note that the rather comparable impact of the substitution on the thermal conductivity favors a high figure of merit for the n-type material. According to this observation, the improvement of p-type materials needs essentially an improvement of their electric conductivity and thus of their power factor.

7.2.5 Summary of $NiTi_{1-x}M_xSn$ (M = Sc, V)

The solid solution series $NiTi_{1-x}M_xSn$ (M = Sc, V) was systematically studied by experimental and theoretical methods. The electronic structure and transport properties of the compounds were measured in detail and compared to all-electron ab-initio density functional calculations. The results show the possibility to create n-type and p-type thermoelectric materials within one compound series.

X-ray powder diffraction was performed to determine the structure type and the lattice parameters of the compounds. All compounds of the series crystallize in the $C1_b$ structure type. Substitution of Ti by V or Sc leads to a linear change of the lattice parameter according to Vegards law. A swap of about 5% Ti into the vacant site was found from the diffraction data of pure NiTiSn. Calculations as well as photoelectron spectroscopy revealed that this type of anti-site disorder is responsible for the occurrence of *"in gap"* states that result in the favorable thermoelectric properties of the pure compound.

The thermal conductivity, electrical resistivity, and Seebeck coefficient were measured in the temperature range from 10 K to 300 K. In general the change of measured transport properties with composition agree qualitatively with the calculations. The $n-$type behavior of the pure compound is provided by the *"in gap"* states. Sc substitution of Ti leads to a p-type behavior and a suppression of the *"in gap"* states. The observed behavior of the resistivity of both types of substituted materials is explained by the calculations respecting disorder scattering. The lattice thermal conductivity of the $NiTi_{1-x}M_xSn$ (M = Sc, V) compounds are effectively depressed by substitution of Ti by Sc or V. The sign of the Seebeck coefficient with Sc substitution from n- to p-type is related to the appearance and the dominant contribution of free holes to the intermetallic semiconductor conductivity. In addition, the electronic structure of the compounds was studied using bulk sensitive, hard X-ray photoelectron spectroscopy. The observed *"in gap"* states suggested that the electronic states close to the Fermi edge play a key role to control the thermoelectric properties. The observed shifts of the valence states agree with the calculated shift of the Fermi energy when substituting Ti by Sc or V.

The reduction of the thermal conductivity is achieved by substitution of Ti and independent of the type of the doping (Sc or V). Therefore, the impact of the lowered thermal conductivity on the figure of merit is nearly the same. The presented systematic study of the solid solution series $NiTi_{1-x}M_xSn$ (M = Sc, V) shows the possibility to create n-type and p-type thermoelectric materials within one compound series.

7.3 Thermoelectric Properties and Electronic Structure of Substituted Heusler Compounds: $NiTi_{0.3-x}Sc_xZr_{0.35}Hf_{0.35}Sn$.

7.3.1 Transport properties

The temperature dependencies of the electrical conductivity ($\sigma(T)$), the Seebeck coefficient, and the power factor of the compounds $NiTi_{0.3-x}Sc_xZr_{0.35}Hf_{0.35}Sn$ (x = 0, 0.01, and 0.04) are shown in Figure 7.12. The temperature dependence of the electrical conductivity exhibits a metallic or semimetallic-type tendency for the pure compound and becomes closer to semiconducting for the Sc substituted compounds. A considerable decrease of $\sigma(T)$ by more than one order of magnitude under Sc substitution is observed. The sign of the Seebeck coefficient for $NiTi_{0.3}Zr_{0.35}Hf_{0.35}Sn$ is negative and switches to positive when substituting Ti by small amounts of Sc. At 4% substitution it reaches its highest positive values.

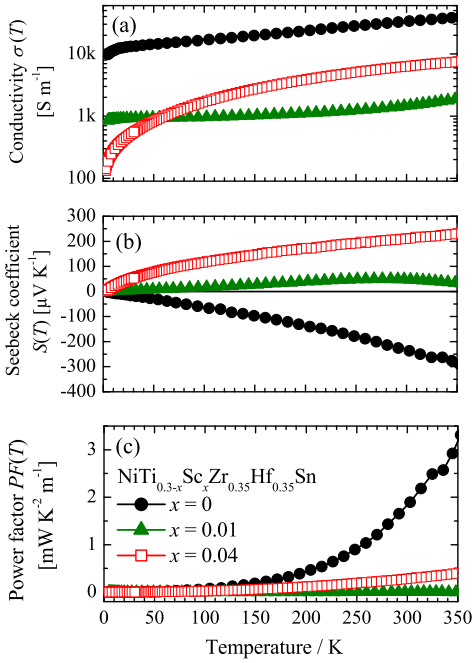

Figure 7.12: Temperature dependence of electrical conductivity $\sigma(T)$, Seebeck coefficient $S(T)$, and power factor $PF(T)$ of $NiTi_{0.3-x}Sc_xZr_{0.35}Hf_{0.35}Sn$ (x=0, 0.01, and 0.04).

Table 7.1 summarizes the behavior of thermal conductivity, Seebeck coefficient, electrical conductivity, power factor, and figure of merit of $NiTi_{0.3-x}Sc_xZr_{0.35}Hf_{0.35}Sn$ with different Sc substitution x at 350 K. The thermal conductivity exhibits a maximum value of 5.75 W $K^{-1}m^{-1}$ for the pure $NiTi_{0.3}Zr_{0.35}Hf_{0.35}Sn$ compound and decreases with increasing Sc content. The reduction of κ is explained by the substitution of Sc atoms at the Ti site, which enhances the point defect scattering for phonons due to additional mass fluctuations.

The sign of the Seebeck coefficient for $NiTi_{0.3}Zr_{0.35}Hf_{0.35}Sn$ is negative and changes to positive. It increases with increasing amount of Sc. Since Sc has one less valence electron compared to Ti, it acts as hole donor and thus the number of hole carriers increases. A maximal Seebeck coefficient of +230 μV/K was found at 4% Sc substitution, which is the highest value for *p-type* thermoelectric materials based on Heusler compounds. For the *p*-type compounds the power factor increases with increasing amount of Sc. The highest value of 0.63 mW $K^{-2}m^{-1}$ is obtained for 5% substitution but is still lower compared to *n*-type compounds. The different behavior of both types arises from the conductivity. In Reference [8] it was explained by the different influence of the impurity scattering on the electrons in the valence or conduction band.

Table 7.1: Thermal conductivity κ, Seebeck coefficient S, electrical conductivity σ, power factor PF and figure of merit ZT of $NiTi_{0.3-x}Sc_xZr_{0.35}Hf_{0.35}Sn$ at 350 K.

x (%)	0	1	3	4	5
κ [$WK^{-1}m^{-1}$]	5.75	4.06	2.31	2.83	2.72
S [μVK^{-1}]	-288	33	128	230	183
σ [10^3 Sm^{-1}]	38.86	1.91	2.24	7.47	19.08
PF [$mW\ K^{-2}m^{-1}$]	3.19	2.7 10^{-3}	0.04	0.41	0.63
ZT	0.19	4.8 10^{-4}	0.005	0.05	0.08

7.3.2 Valence band spectra

The electronic structure of the compounds was investigated by HAXPES. Figure 7.13 compares the valence band spectra of $NiTi_{0.3}Zr_{0.35}Hf_{0.35}Sn$ ($x = 0$) to the Sc substituted compound $NiTi_{0.26}Sc_{0.04}Zr_{0.35}Hf_{0.35}Sn$ ($x = 0.04$). The spectra of $NiTi_{0.3}Zr_{0.35}Hf_{0.35}Sn$ were measured at different excitation energies of about 6 and 8 keV. Only a slight difference is observed that is caused by the change of the partial cross sections for s and d electrons with energy. The valence band spectrum of $NiTi_{0.26}Sc_{0.04}Zr_{0.35}Hf_{0.35}Sn$ was measured at 6 keV. The maximum at about -8.5 eV arises from the s states localized at Sn. These states as well as the characteristic Heusler sp hybridization gap at around - 7 eV are clearly resolved. The higher lying valence band spectrum of both compounds shows clearly a structure with four major maxima. Those typical Heusler structures were previously predicted and detected in theoretical [177] and experimental [8, 50] works.

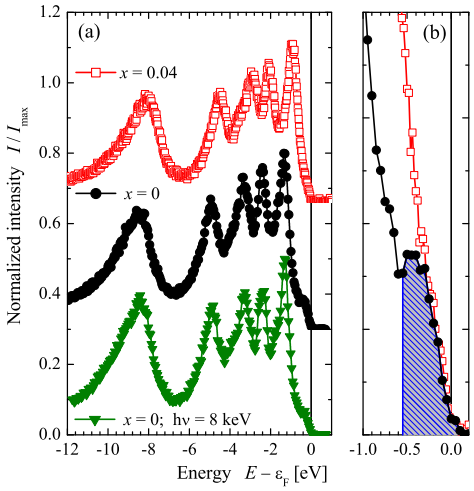

Figure 7.13: Valence band spectra of $NiTi_{0.3-x}Sc_xZr_{0.35}Hf_{0.35}Sn$ ($x = 0$, 0.04). The *in gap* states are marked by the shaded area in b).

The steep onset of the topmost d band hints at a gap size of approximately 0.8 eV in the

pure compound. The reduction of the number of valence electrons in the Sc substituted compound leads to a considerable shift of the *d*-states towards the Fermi energy (ϵ_F). In the pure compound, the energy range of the gap is filled by a distinguished state. This *in gap* state just below ϵ_F is clearly revealed in Figure 7.13 b). A depletion of that state is observed in the Sc substituted compound. From the integral valence band intensities it is approximated that the number of electrons in the gap (shaded area) correspond to 0.16 or 0.028 electrons for $x = 0$ or 0.04, respectively. These values agree with the reduction of valence states by the substitution of Ti ($3d^4$) by Sc ($3d^3$). The *in gap* states were previously suggested to have a pronounced influence on the thermoelectric properties of Heusler compounds [8, 50, 178, 179].

7.3.3 Summary for $NiTi_{0.3-x}Sc_xZr_{0.35}Hf_{0.35}Sn$

A systematic study of the transport and thermal properties on the Sc substituted alloy $NiTi_{0.3-x}Sc_xZr_{0.35}Hf_{0.35}Sn$ was performed in the temperature range from 2 K to 300 K. In summary it was shown that the thermal conductivity of the compounds is effectively lowered when substituting Ti by Sc. The substitution leads to an increase in the power factor. A maximum value of 0.63 mW/(K^{2}m) for the *p-type* material is obtained at 350 K and a Sc content of $x = 0.05$. Both together lead to a relatively high figure of merit that is only about a factor of 2 smaller than the one of the parent, *n-type* compound.

The studies of the electronic structure using hard X-ray photoelectron spectroscopy showed that the observed *in gap* states close to the Fermi energy play a key role on the behavior of the transport properties. This systematic study shows the possibility to create *n-type* and *p-type* thermoelectric materials based on the same basic compound and thus to produce suitable, well matched pairs for thermoelectric devices.

8 CoTiSb Based Heusler Compounds: Electronic Structure, Optical, Mechanical and Transport properties

8.1 Introduction

Heusler compounds with a 1:1:1 composition and ordered $C1_b$ structure consist of three filled interpenetrating fcc sublattices and one vacant sublattice V_c. Those compounds are expected to be semiconducting for a valence electron concentration (VEC) of 18 in the primitive cell [31, 34] and considered to be promising thermoelectric materials [37, 180].

Since the first investigation as semiconductor by Kouacou and co-worker [181], CoTiSb has attracted a considerable interest as a promising candidate for thermoelectric applications. Up today there are more than thirty investigations, that are focused on CoTiSb-based compounds, concerning band structure calculations [32, 33, 34, 170, 182, 183, 184], synthesis [185], disorder [186, 187, 188, 189], magnetism [172, 173, 190] and thermoelectric properties [167, 191, 192, 193, 194, 195, 196, 197, 198, 199]. The best p-type thermoelectric properties for Heusler compounds were achieved in CoSb-based materials [167, 196]. Recently, the highest thermoelectric figure of merit ZT of 0.8 at 700°C was observed for the p-type Heusler compound $CoZr_{0.5}Hf_{0.5}Sb_{0.8}Sn_{0.2}$ [46]. This promising behaviors enhance intensive theoretical and experimental studies of the CoTiSb compound.

On the other hand, the study of the optical and mechanical properties were reported as useful method to investigate the band gap [200, 201] and stability of some Heusler compounds [202, 203, 204]. Most recent studies focused on the optimization of the thermoelectric properties, such as nanostructuring to minimize thermal conductivity, or partial atom substitution to decrease electrical conductivity and/or increase the Seebeck coefficient. However, investigations of optical and mechanical properties have been neglected.

In the present study, the optical properties of CoTiSb measured using spectroscopic ellipsometry and Fourier Transform infrared spectroscopy were investigated and compared to ab-initio calculation. The stability of the compound was studied by investigation of mechanical properties and phonon calculations. The electronic structure of CoTiSb and Sc and V substitution of Ti was investigated by means of hard X-ray photoelectron spectroscopy (HAXPES) and compared to the calculations. The influence of site disorder on the electrical conductivity of CoTiSb was investigated by ab-initio calculations and compared to experiments. Furthermore, the effect of Ti substitution by Sc and V on the thermoelectric properties of the Heusler compounds $CoTi_{1-x}M_xSb$ (where M = Sc, V and $0 < x \leq 0.2$) was investigated and compared to theoretical predictions.

8.2 Details of the calculations

Electronic structure, optical properties and transport properties of the compounds were calculated by the full potential linearized augmented plane wave (FLAPW) method as implemented in WIEN2k [103] in combination with a modified version of BOLTZTRAP [205](for details see Reference [8]). The calculations were performed in the semi-relativistic mode by solving the Dirac equation only for core states and neglecting spin-orbit interaction for the valence states. The exchange-correlation functional was taken within the generalized gradient approximation (GGA) in the parametrization of Perdew, Burke, and Enzerhof (PBE) [107]. For integration a $(31 \times 31 \times 31)$ point mesh was used resulting in 816 k-points in the irreducible wedge of the Brillouin zone. The energy convergence criterion was set to 10^{-5} Ry and simultaneously the criterion for charge convergence to $10^{-3}e^{-}$. Relaxed lattice parameters were used in all calculations, the optimization of the volume resulted in $a = 5.8981$ Å for CoTiSb. Details of calculations are described in Reference [8].

The calculation of the electronic structure of disordered or substituted compounds is more demanding compared to the pure compounds because of non-integer site occupancies and loss of periodicity. One approach is the use of supercells with a large number of sites. This allows to model vacancies by removal of atoms in the supercell or anti-site disorder by changing the positions of selected atoms. Substituted compounds may be described by exchanging kinds of atoms on fixed sites. Drawback is that the calculations can be performed only for fractional types of site occupancies ($x = i/n$, $i < n$) that depend on the total number of sites (n) in the supercell. In the present work two alternative approaches were used that allow for non-rational site occupancies x. One is the virtual crystal approximation (VCA) that can be performed within the FLAPW method. In the VCA, the atoms are replaced by *"virtual"* elements that have different (non-integer) nuclear charges and numbers of valence electrons. It is suited for small amounts ($x \ll 1$) of substituted atoms that are (neighboring) in the same row of the periodic table of elements. The other method used here – and allowing to replace *"real"* elements – is the coherent potential approximation (CPA) that can be performed within the Korringa-Kohn-Rostoker (KKR) Green's function method. In the CPA, the random array of real on-site potentials is replaced by an ordered array of effective potentials and thus it describes the behavior of an atom in a mean-field environment. The CPA is suited for any site occupation $0 < x < 1$. The disadvantage of both, VCA or CPA, is that they do not include the local environment effects such as preferential ordering or lattice relaxations around the impurity site.

The electronic structure of substitutionally disordered $CoTi_{1-x}M_xSb$ (where M = Sc, V and $0 < x \leq 0.2$) was calculated by means of the VCA. The substitution of Ti by an amount x of Sc or V results in a reduction or an addition by xe^{-} because the difference in the valence electrons of those atoms is ± 1. Therefore, the charge and number of electrons at the Ti site (4c) of CoTiSb was set to $(22 \pm x)\, e^{-}$ to model the $Co(Ti_{1-x}M_x)Sb$ (M = Sc, V) solid solutions. It should be noted that the VCA method has the drawback that it is not element specific. This means that the result would be the same for $CoTi_{1\pm y}Sb$ or any suitable substitution by other elements resulting in the same valence charge. The

resulting band structure is also an approximation as it is absent in real solid solutions with random site occupation and thus a missing periodicity of the crystalline structure.

Furthermore, the electronic structure calculations of CoTiSb with antisite disorder and substituted $CoTi_{1-x}M_xSb$ (where M = Sc, V and $0 < x \leq 0.2$) have been performed by means of the fully relativistic KKR method in combination with the CPA as implemented in the MUNICH-SPRKKR program package [108]. The calculations were performed in the fully relativistic mode by solving the Dirac equation for core and valence states. The k-integration mesh was set to a size of $(28 \times 28 \times 28)$ during the selfconsistent cycles (1128 k-points in the irreducible wedge of the Brillouin zone). The gradient correction of the PBE-functional was switched off for the vacant site to avoid numerical instabilities caused by low charge densities. The Co atoms are placed on the 4a Wyckoff position, the Ti atoms are placed together with the M atoms on the 4c position, and the main group element Sn is finally placed on the 4d position. The swap-type disordered CoTiSb (here $Co(Vc_{1-x}Ti_x)(Ti_{1-x}Vc_x)Sb$) compound was also treated using the CPA method by placing a fraction of x vacancies (Vc) on the regular Ti site (4c) and simultaneously the swapped Ti part $(1 - x)$ on the 4b Wyckoff position.

8.3 Structure and composition

The experiments revealed that pure CoTiSb samples have the correct 1:1:1 stoichiometry and the $C1_b$ structure. Figure 8.1(b) shows the primitive cell of cubic face centered CoTiSb. The $C1_b$ structure exhibits a vacant site (Vc) in the 4b Wyckoff position (the light sphere in the center at $(\frac{1}{2}, \frac{1}{2}, \frac{1}{2})$). Co, Ti, and Sb occupy the 4a, 4d, and 4c Wyckoff positions at (0,0,0), $(\frac{3}{4}, \frac{3}{4}, \frac{3}{4})$, and $(\frac{1}{4}, \frac{1}{4}, \frac{1}{4})$, respectively. The space group is $F\,\bar{4}3m$ and the primitive cell as well as the vacant and all three occupied Wyckoff positions have T_d point group symmetry. A Rietveld refinement of the x-ray powder diffraction of CoTiSb is shown in 8.1(a). The refinement has the lowest R value ($\leq 2.7\%$) when assuming a 3.7 % swap of Ti atoms into the vacant position Vc. Assuming other types of antisite disorder resulted in considerably larger R values. The lattice parameter determined from powder XRD is $a_{\mathrm{exp}} = 5.8837$ Å. The observed value is in good agreement with those reported previously [182, 172]. It is slightly smaller (0.2%) compared to the optimized lattice parameter as is typical for calculations using GGA. The difference is too small to have a noticeable impact on the result of the calculations reported in the following.

Figure 8.2(a) shows a SEM micrograph of polished CoTiSb recorded over a large area. No evidence of other phases or faults (as for example cracks or inclusions) was observed. The compositional homogeneity checked by the corresponding EDX line scan is show in Figure 8.2(b). A uniform distribution of the elements consistent to the microstructure is observed. The results of the quantitative chemical analysis are presented in Table 8.1. CoTiSb shows a 1:1:1 composition within the experimental uncertainty.

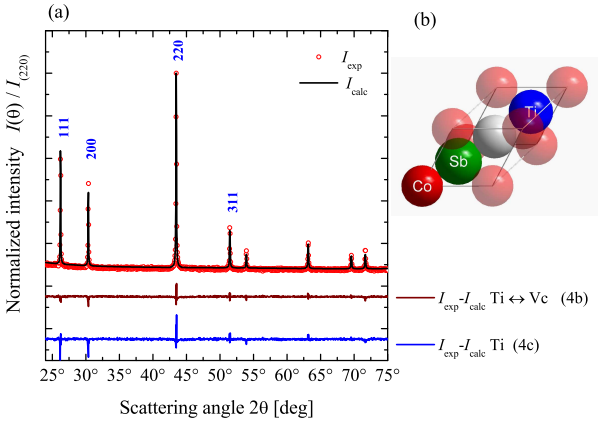

Figure 8.1: Crystalline structure of CoTiSb.
(a) shows the X-ray diffraction data and results of the Rietveld refinement for ordered and partially disordered CoTiSb. The data were taken at room temperature using Cu K_α radiation. (b) shows the primitive cell of CoTiSb in the $C1_b$ structure. The light sphere in the center represents the vacancy.

Table 8.1: Chemical composition of CoTiSb

Atom	Co	Ti	Sb
Fraction	1.01 ± 0.01	1.00 ± 0.02	0.99 ± 0.02

8.4 Electronic structure and optical properties

Figure 8.3 compares the band structure of pure CoTiSb to the cases of electron lack and excess at the Ti site calculated in VCA. The topmost valence band at ϵ_F of the semiconducting pure CoTiSb ($x = 0$) has t_2 character at the Γ point that has T_d symmetry. It is followed by d bands of e (-1.56 eV) and bands of t_2 (-2.39 eV) character. The low lying a_1 states are found below -9.4 eV and are separated from the higher lying bands by the *sp* hybridization gap that is typical for Heusler compounds. The pure CoTiSb exhibits an indirect $\Gamma - X$ band gap of about 1.06 eV, whereas the optical gap at Γ is considerably larger (1.83 eV). Both, topmost valence band and lowest conduction band appear very low dispersing with a bandwidth of ≈ 150 meV in the $\Gamma - L$ direction and thus allow easily for direct optical transitions at energies of about 1.8 eV.

The variation of the number of valence electrons results in an emptying or filling of the valence or conduction bands, respectively. The result is a shift of the ϵ_F into the valence ($x < 0$) or conduction ($x > 0$) bands. Due to the high density of states already close to both band edges this energy shift is only small. At a doping level of $x = \pm 0.1$, ϵ_F is located about 110 meV below or 115 meV above the valence or conduction band edges. The gap is kept with the same size when adding or removing electrons and the change of the electronic structure appears to be *rigid-band* type, that is, no major changes in the dispersion are observed here when using the VCA approach.

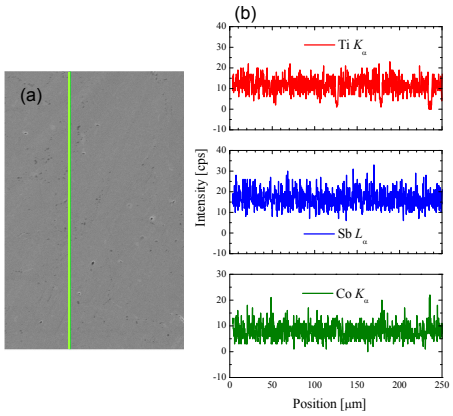

Figure 8.2: EDX measurement of CoTiSb.
(a) SEM micrograph and (b) intensities of characteristic x-ray emission of Ti K_α, Sb L_α, and Co K_α along the line scan.

The optical properties of pure CoTiSb are presented in Figure 8.4. The spectral dependence of the complex permittivity $\varepsilon = \varepsilon_r + i\varepsilon_i$ is shown in Figure 8.4 (a). The dominant feature of those spectra is a strong absorption peak at 1.80 eV. This value is in perfect agreement with the direct band gap at Γ and the distance between the flat valence and conduction bands in the $\Gamma - L$ direction as shown in Figure 8.3 (b). For energies below 1.8 eV, the optical absorption (ε_i) quickly drops to zero, as expected for semiconductors when the photon energies become smaller than the gap size. The experimentally determined spectra are compared with the results of the ab-initio calculations. The main features are well reproduced. The position and strength of the optical absorption peaks for energies above 2 eV, namely at around 3.2 and 5.0 eV, agree well between experimental data and the ab-initio calculations.

The wide range infrared reflectivity is presented in Figure 8.4(b), measured from 10 meV (far-infrared) to 1 eV (near infrared). The dominant feature is a strong absorption peak at about 34 meV, where the reflectivity changes abruptly from 100% to 30%. There is also one small absorption peak observed at about 28 meV (see inset in Figure 8.4(b)).

In order to describe the reflectivity in detail, the following contributions to the permittivity are used for a fit of the data:

$$\varepsilon = \varepsilon_\infty + \varepsilon_{\mathrm{Dru}} + \sum_{j=1}^{3} \varepsilon_{\mathrm{GL},j}. \tag{8.1}$$

The term ε_∞ describes the shift of the real part of the permittivity due to photon absorption at higher photon energies. The Drude term originates from the presence of free electrons: $\varepsilon_{\mathrm{Dru}}(E) = E_D^2/(-E^2 - i\gamma E)$, where E_D and γ are the plasma and damping energies, respectively. The fit provides a rather week Drude term with $E_D = 250$ meV and $\gamma = 223$ meV. This corresponds to a quasi-static conductivity of $\sigma = (E_D^2\varepsilon_0)/(\gamma\hbar) =$

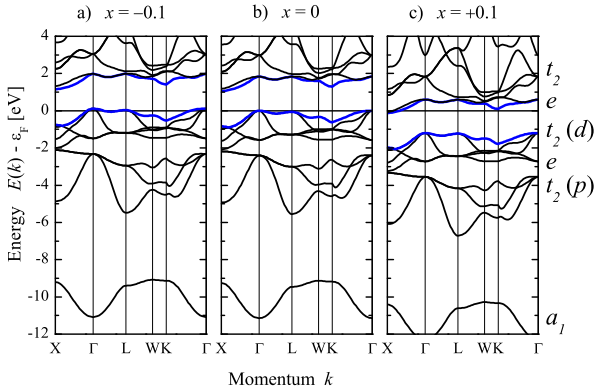

Figure 8.3: Band structure of CoTiSb with $(22 \pm x)\ e^-$ $(x = 0, 0.1)$. The calculations were performed using FLAPW with VCA. The irreducible representations of the states at Γ are marked in (c).

3.8×10^3 Sm^{-1}. This rather low optical conductivity reflects the semiconducting nature of CoTiSb (ε_0 is the vacuum permittivity and $\hbar$ is the Planck's constant). The last three terms $\varepsilon_{\mathrm{GL},j}$ correspond to resonant phonon vibrations and are described using Lorentz-Gaussian (Voight) oscillators [206].

The dominant peak at $E_{0,1} = 32.1$ meV and two minor peaks at $E_{0,2} = 33.1$ meV and $E_{0,2} = 28.7$ meV describe the main features of the infrared spectra (bottom inset in Figure 8.4b). The fit reveals that those absorption peaks are very sharp, with quality factors of $E_0/\gamma > 100$. The peaks originate from absorption of optical phonons (compare Figure 8.8). Similar absorption peaks were observed at photon energies of 16.7 and 23.8 meV in PtYSb [207] or at 15.3 and 21.1eV in NiHfSn [200].

8.5 Hard x-ray valence band photoelectron spectroscopy

The electronic structure of CoTiSb, $\mathrm{CoTi_{0.95}Sc_{0.05}Sb}$, and $\mathrm{CoTi_{0.9}V_{0.1}Sb}$ was investigated by HAXPES. The spectra were taken at 20 K sample temperature with an excitation energy of about 6 keV. Figure 8.5 compares the calculated total and partial DOS of CoTiSb to the measured valence band spectra. The valence band spectrum with five maxima exhibits the typical structure of Heusler compounds with $C1_b$ structure [184, 8, 208, 207]. In the present work, those states are clearly and much better resolved compared to previous investigations of the valence band of CoTiSb [184, 173]. Cause is the much higher resolution ($\Delta E = 140$ meV) of the high brilliant photon source at Spring-8.

All major structures observed in the spectrum are in well agreement to the calculated DOS (see also Figure 8.3 for the irreducible representations of the states at the Γ point). The low lying maximum at about -11.5 eV below ϵ_F arises from a_1 (s) states localized at the main group element Sb. Compared to the partial DOS, the peaks at -1.6, -2.3,

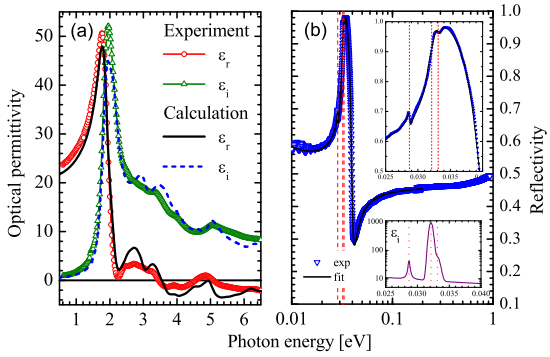

Figure 8.4: Optical properties of CoTiSb.
(a) compares the calculated and measured real ε_r and imaginary ε_i part of the permittivity and the infrared reflectivity is shown in (b). Red dashed lines show positions of resonance peaks. Bottom inset in (b) is imaginary part of the permittivity in the infrared region. The calculations in (a) were performed using FLAPW.

and -4.0 eV arise mainly from different d states with t_2 or e character located at Co and Ti. The peaks at about -6.9 eV arises mainly from t_2 (p) states. The peaks close to ϵ_F are sharper, as those lying farther away from ϵ_F. This is due to the lifetime broadening that increases with increase of the binding energy. Furthermore, the intensity ratios of the peaks are different from the calculated DOS. This deviation arises from the different partial cross sections of the s, p and d states located at different atoms. Both, cross section and lifetime effects are discussed in more detail in Reference [184].

A large amount of states inside of the semiconducting gap is obvious from Figure 8.5(d). In Section 8.3, evidence for a Ti↔Vc type antisite disorder of about 4% was found by XRD. As reported previously [173, 8], the occupation of the vacant site of the $C1_b$ structure by one of the constituents while keeping the 1:1:1 stoichiometry leads to the occurrence of *in-gap* states. KKR-CPA calculations were performed to explain and analyze the influence of Ti↔Vc antisite disorder on the electronic structure. The results for 5% swap of Ti atoms into the vacant site at fixed, ideal 1:1:1 stoichiometry are shown in Figure 8.6.

A band structure is not longer defined in disordered or substituted systems with random site occupancies due to the lack of periodicity. However, the density of states and the Bloch spectral function can still be calculated by Green's function methods. The antisite disorder causes a broadening of the initial band dispersion as is seen from the Bloch spectral function in comparison to the initial band structure. The course of the major features is the same for the KKR-CPA and the FLAPW-VCA calculations, in particular there are no mentionable differences in the energies between valence and conduction states. Different from the original band structure, now one recognizes states in the initial band gap that are found around the Γ-point and thus are strongly localized

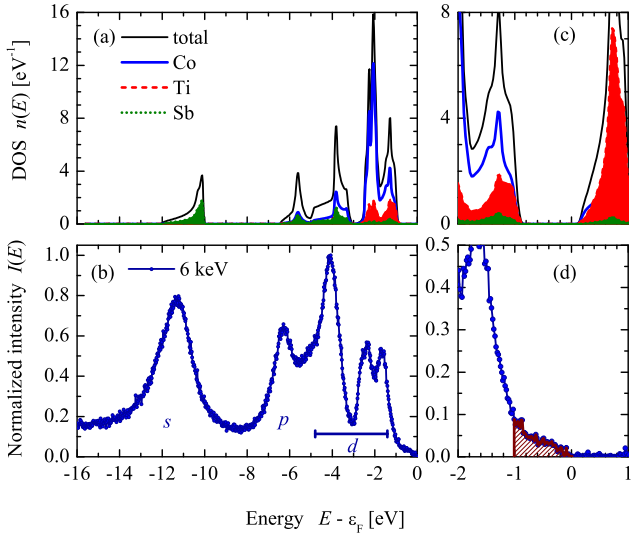

Figure 8.5: Total and partial density of states (a) and (c), and valence band spectra (b) of CoTiSb. The excitation energy was fixed to 5.9534 keV . The DOS was calculated by FLAPW. The *in gap* states are marked by the shaded area in (d).

as expected for impurity states. The states exhibit a low dispersion but are found over a rather wide band of energies inside of the initial semi-conducting band gap. The orbital momentum analysis of the DOS reveals that those in-gap states have d-character. It is interesting to note that the in-gap states below ϵ_F are to a large amount localized at the Co atoms, whereas those above ϵ_F are to a larger amount localized at both Ti atoms in the original 4d as well as the vacant 4b position (see Figure 8.6b). That is, they are split of from the former valence or conduction band edges.

Figure 8.7 compares the measured valence band spectra of the Sc ($CoTi_{0.95}Sc_{0.05}Sb$) and V ($CoTi_{0.9}V_{0.1}Sb$) substituted compound. Structures similar to those of pure CoTiSb are observed also for the substituted compounds. A remarkable shift of the peaks towards the Fermi energy ϵ_F is obtained for Sc substitution, whereas for V substitution a shift away from ϵ_F is observed. It is explained by the depletion or filling of states in the valence band when substituting Ti ($3d^2 4s^2$) by Sc ($3d^1 4s^2$) or V ($3d^3 4s^2$). In fact, ϵ_F is changed or – equivalently – the bands move towards or away from ϵ_F that is here the reference energy.

For a pure semiconducting compound the Fermi-energy is located at $T = 0$ –by definition– at the highest occupied state that is the top of the valence band. Any small deviation $\delta \to \pm 0$ in the number of electrons will shift the Fermi energy in the spectra. Creation of holes ($\delta < 0$), indeed, keeps ϵ_F very close to the top of the valence band. In contrast, creation of electrons ($\delta > 0$) will cause a jump of ϵ_F to the bottom of the conduction band. From Figure 8.5 and 8.7(b) it is evident that the CoTiSb sample is electron doped. Independent on the occurrence of in-gap states, ϵ_F is obviously located

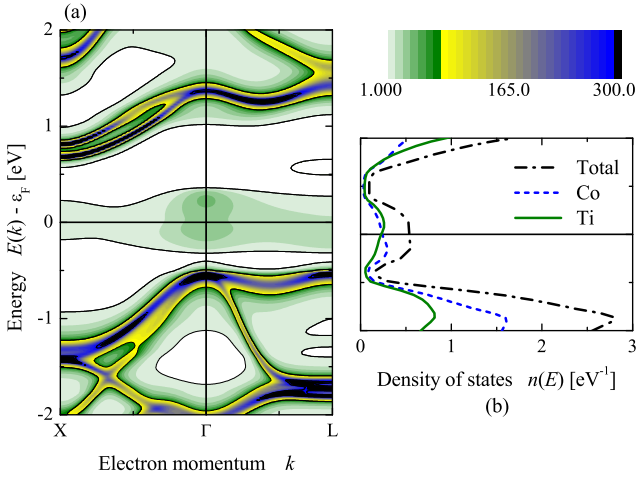

Figure 8.6: Electronic structure of CoTiSb with 5% Ti↔Vc antisite disorder. (a) shows the Bloch spectral function in the Δ ($\Gamma - X$) and Λ ($\Gamma - L$) directions. (b) shows the accompanied total and partial density of states calculated for the full Brillouin zone.

at the bottom of the conduction band. Substitution by V and thus further electron doping results in a only small shift of the steep onset of the *d*-bands by about 150 meV as is expected from the VCA calculations. From the spectrum of $CoTi_{0.9}V_{0.1}Sb$ it is seen that the in-gap states survive the V substitution. The substitution by Sc and thus hole doping leads seemingly to much more drastic changes. Here, the onset of the *d*-band jumps by about 1 eV towards 0 and no in-gap states are recognized. This change of the spectrum is caused because the Fermi energy falls now into the valence band. The $in-gap$ state, if still existing, stays thus unoccupied and can not be detected anymore by photoelectron spectroscopy. The electron filling and depletion is also seen from the shift of the major maxima in the spectra of the V and Sc substituted samples. The average shift is $\Delta E = 1.03 \pm 0.03$ eV. The differences in the spectra taken from $CoTi_{0.9}V_{0.1}Sb$ and $CoTi_{0.95}Sc_{0.05}Sb$ thus confirm that the size of the band gap is in the order of 1 eV in agreement to the ab-initio calculations.

8.6 Vibrational and mechanical properties

The vibrational properties of CoTiSb were calculated by means of PHONON [121] on the basis of the results from WIEN2k. The primitive cell containing three atoms was enlarged to a cell with 12 distinguished atoms to calculate the Hellmann-Feynman forces for the phonon analysis. For these calculations, a force convergence criterion of 10^{-4} Rya_{0B}^{-1} was used in addition to the energy convergence criterion. Figure 8.8 shows the calculated phonon dispersion $h\nu(q)$ and the accompanied density of states $g(\omega)$ of CoTiSb. As expected for $C1_b$ structure with three atoms in the primitive cell, the phonon dispersion exhibits 9 branches, three acoustic (1 longitudinal (LA) and 2 transversal (TA)) and 6

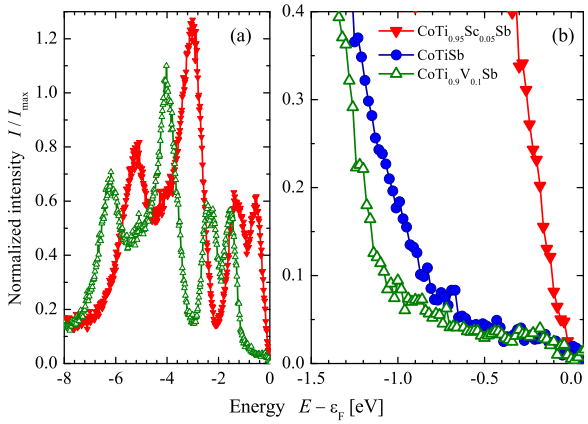

Figure 8.7: Valence band spectra of substituted CoTiSb.
(a) shows the valence bands of $CoTi_{0.95}Sc_{0.05}Sb$ and $CoTi_{0.9}V_{0.1}Sb$ in the range of the d states and (b) the energy range close to ϵ_F on an enlarged view (CoTiSb is included for comparison).

optical branches. A gap of about 4.4 meV between the acoustic and the optical branches is observed, due to the differences in the atomic masses of the atoms. The energies of the optical phonons at the Γ point are 28.4 meV and 32.2 meV, in perfect agreement with the absorption lines observed in the experiment as shown in Figure 8.4b).

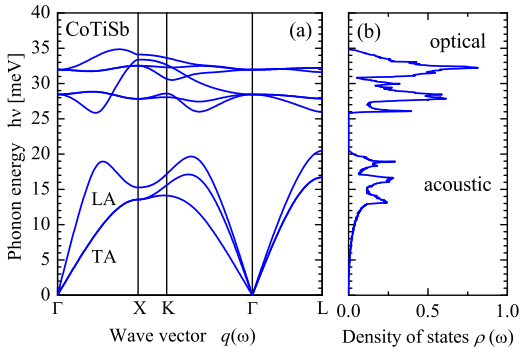

Figure 8.8: Phonon dispersion (a) and corresponding density of states (b) of CoTiSb.

The mechanical stability of thermoelectric materials is required to reach high efficiency and reliability of thermoelectric modules. Therefore, the mechanical properties of CoTiSb were investigated. Details of the calculations have been reported in previous work [202]. The values of the calculated elastic constants c_{ij}, bulk modulus B, Young's modulus E, rigidity modulus G, Poison's ratio ν, and elastic anisotropy A_e are listed in Table 8.2. The values of the calculated elastic constants as well as the elastic anisotropy A_e being close to unity satisfy the criteria for mechanical stability of CoTiSb in the cubic system [118].

Table 8.2: Mechanical properties of CoTiSb.
Calculated elastic constants c_{ij} as well as the modulus are given in GPa; Poison's ratio (ν) and elastic anisotropy (A_e), are dimensionless quantities.

c_{11}	c_{12}	c_{44}	B	E	G	ν	A_e
259	84	93	142	224	91	0.24	1.06

The elastic anisotropy $A_e = 2\,c_{44}/(c_{11} - c_{12})$ is close to unity that means that Young's modulus $E(\hat{r})$ exhibits a spherical distribution. For $A_e \leq 0$ or $A_e \to \infty$, the crystal would not be stable in the cubic structure as one of the Born-Huang criteria for stability ($c_{11} - c_{12} > 0$ or $c_{44} > 0$) is violated [118]. For $A_e > 1$ one finds that $E(\hat{r})$ is highest along the space diagonal ($\langle 111 \rangle$-type directions) whereas it is highest along the cubic axes ($\langle 001 \rangle$-type directions) for $1 > A_e > 0$.

Figure 8.9(a) compares the temperature dependence of the measured specific heat $C(T)$ to the calculated lattice specific heat $C_L(T)$. Below 100 K, $C(T)$ agrees well with $C_L(T)$, where at higher temperature the measured specific heat $C(T)$ is higher than $C_L(T)$, due to the contribution from electrons in the experimental $C(T)$. Both curves increases with increasing temperature and reach a value of about 9 k_B at high temperatures as expected from the Dulong-Petit law.

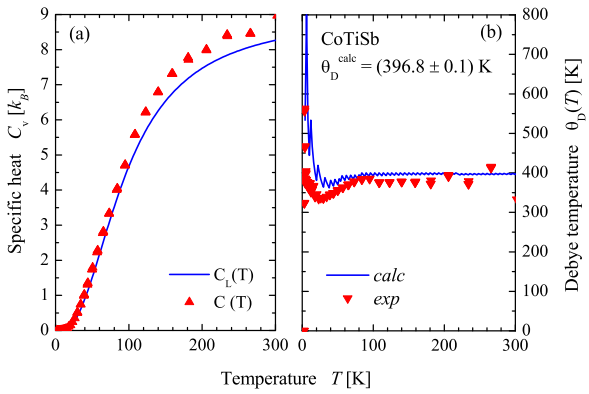

Figure 8.9: Specific heat (a) and Debye temperature (b) of CoTiSb. $C(T)$ is the measured specific heat and $C_L(T)$ is the calculated lattice specific heat.

The Debye temperature Θ_D^{calc} or Θ_D^{exp} is found by fitting the calculated or measured specific heat to the Debye model, respectively. The results are shown in Figure 8.9(b). The Debye temperature calculated from $C_L(T)$ is $\Theta_D^{\text{calc}} = 396.8$ K in the high-temperature limit ($T > 100$ K). This value is in good agreement with $\Theta_D^{\text{exp}} = 396.2$ K obtained from the measured specific heat $C(T)$.

8.7 Transport properties

Due to the vacancy in the crystalline structure, $C1_b$ Heusler compounds are sensitive to anti-site disorder, which may have a strong influence on the electronic structure, and consequently on the physical properties [8, 37, 173, 189]. Therefore, the electrical conductivity σ of difference kinds of disorder in CoTiSb was calculated using KKR-CPA. The antisite disorder was modeled within CPA. Figure 8.10a) shows the calculated conductivity σ of disordered CoTiSb by swapped Sb or Ti atoms into the vacant position 4*b*. The density of states at the Fermi energy is drawn in the inset as function of the disorder leve δ. The Co-Vc swap causes less states in the gap at ϵ_F, a noticable conductivity was only found for $\delta > 5\%$. It is interesting to note that the Sb swap causes a faster increase of the conductivity compared to Ti, even though the density of states at the Fermi energy behaves opposite. The horizontal line at about 20×10^3 Sm^{-1} shows the measured conductivity of CoTiSb. For a disorder of 3.7% (as found from the refinement of the XRD data) the measured conductivity is in well agreement to the Ti↔Vc swap.

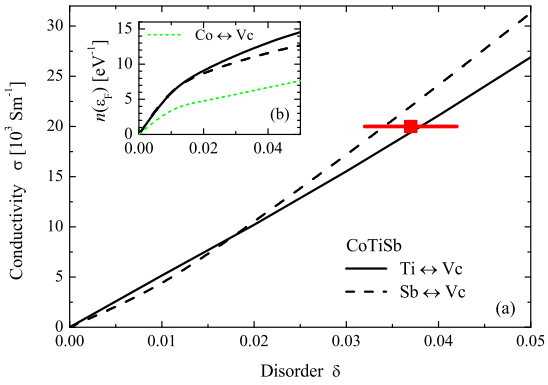

Figure 8.10: Calculated dependence of the electrical conductivity σ of CoTiSb on different types of disorder.
δ is the number of swapped atom to the vacant position 4*b*. The inset (b) shows the density of states at ϵ_F (the Co - Vc swap is given for comparison). The calculations were performed using KKR with CPA.

Figure 8.11 compares the temperature dependence of electrical resistivity $\rho(T)$, Seebeck coefficient $S(T)$ and thermal conductivity $\kappa(T)$ of pure CoTiSb to the substituted compounds $CoTi_{0.95}Sc_{0.05}Sb$ and $CoTi_{0.9}V_{0.1}Sb$. The electrical resistivity of the substituted compounds exhibits a semiconducting-type behavior and decreases with increasing temperature. The thermal conductivity $\kappa(T)$ of CoTiSb is high and exhibits a maximum at about 60 K that is typical for well- ordered compounds. By Sc or V substitution, a reduction of $\kappa(T)$ by about 30% is observed (see Table 8.3). This reduction is caused by impurity scattering of phonons at the substituted atoms.

The Seebeck coefficient $S(T)$ of CoTiSb is negative with a value of -35 μV/K at

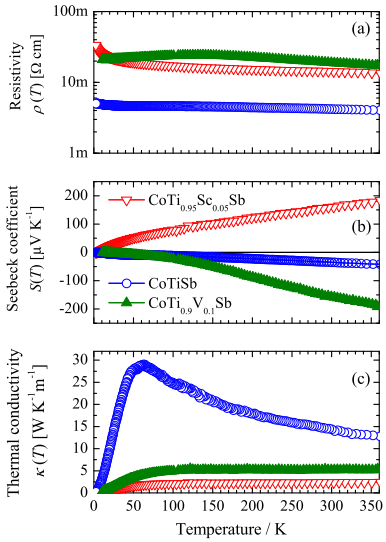

Figure 8.11: Temperature dependence of electrical resistivity $\rho(T)$, Seebeck coefficient $S(T)$ and thermal conductivity $\kappa(T)$ of CoTiSb, $CoTi_{0.95}Sc_{0.05}Sb$ and $CoTi_{0.9}V_{0.1}Sb$.

room temperature. This value is lower compared to the previously reported Seebeck coefficients. Concerning previous works, the measured Seebeck coefficient and electrical conductivity of CoTiSb show mutually inconsistent values from -40 up to -265 μV/K for S (see Refs. [197] and [191]), and from 1×10^3 to 3×10^3 S/m for σ (see Refs. [191] and [167]). It is worthwhile to note, however, that both $S(T)$ and $\sigma(T)$ depend strongly on the synthesis procedures and post fabrication heat treatments.

The absolute value of $S(T)$ increases for V substitution. When substituting Ti by Sc the Seebeck coefficient reverses its sign such that the compound becomes $p-$type in full agreement with the expectations from the calculations (see Figure 8.13). Table 8.3 summarizes the behavior of thermal conductivity, Seebeck coefficient, electrical conductivity, and figure of merit of $CoTi_{1-x}M_xSb$ at 350 K with different amounts (x) of Sc and V substitution. At high Sc substitution (20%), the compound becomes metallic, as expected, and $S(T)$ decreases rapidly. The electrical conductivity of Sc substituted CoTiSb is higher that of the V substituted one, in contrast to the NiTiSn system [8].

However, such differences in the properties depend critically on the element occupying the T and T' sites in the compounds, which play the main role in the behavior of the electronic band dispersion of the topmost valence or lowest conduction bands. To clarify the influence of the electronic structure on the electronic transport properties, the Fermi surfaces of $CoTi_{0.95}M_{0.05}Sb$ (M = Sc, V) were calculated using KKR-CPA. As mentioned above a band structure is not defined in non periodic structures but only the Bloch spectral function. The latter allows to project the number of states onto the Fermi-surface. Figure 8.12(a) and (b) compares parts of the KKR-CPA Fermi surfaces in the $\Gamma - X$ type planes of $CoTi_{0.95}Sc_{0.05}Sb$ and $CoTi_{0.95}V_{0.05}Sb$, respectively.

Table 8.3: Thermal conductivity κ, Seebeck coefficient S, electrical conductivity σ, and figure of merit ZT of $CoTi_{1-x}M_xSb$ (M = Sc, V) at 350 K.

M	x [%]	κ [$WK^{-1}m^{-1}$]	S [μVK^{-1}]	σ [10^3 Sm^{-1}]	ZT
Sc	20	6.6	4	26.1	1.9 10^{-5}
Sc	5	2.4	178	7.3	0.034
Sc	2	3.5	131	15.5	0.027
	0	13	-35	20	0.001
V	1	4.5	-367	2.5	0.012
V	5	4.7	-163	6.7	0.013
V	10	5.2	-183	5.7	0.013

These correspond to Fermi surface cross- sections in the (001) plane. The random site occupation leads to a smearing of the states that cross the Fermi surface. The Fermi surface is populated around the Γ point for Sc substitution, whereas the population is largest around the X point for V substitution. One clearly has only one hole pocket at Γ for Sc but several electron pockets around X and K (M) for V for the different types of substitution. This difference indicates the importance of the band shapes and explains the high value of the measured electrical conductivity for the Sc substituted compound compared to the measured low values for V substitution. It is also clear that the Seebeck coefficient will not follow the simple approximation of the Mott equation [209, 160] where it depends only on the change of the number of carriers through the logarithmic derivative of the density of states at ϵ_F.

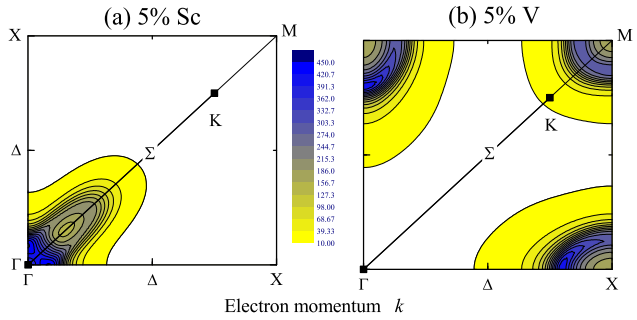

Figure 8.12: Cut through the Fermi surfaces of $CoTi_{0.95}M_{0.05}Sb$ for M = Sc (a) and V (b) in the (001) plane obtained from KKR-CPA calculations. The color (gray) scale corresponds to the number of states crossing the Fermi energy.

The Seebeck coefficient was additionally calculated in VCA for different substitution as described in Section 8.4. Figure 8.13 compares the measured and calculated Seebeck coefficients of Sc and V substituted CoTiSb at T = 300 K. The calculated Seebeck coefficient of CoTiSb is positive, whereas it is negative in the measurements. This

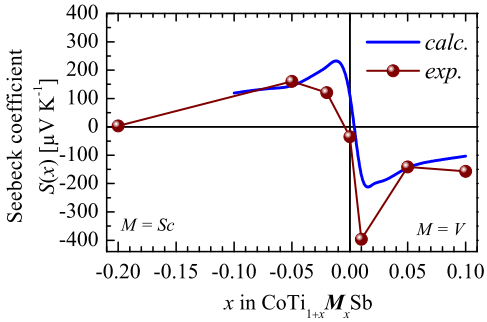

Figure 8.13: Calculated and measured Seebeck coefficient $S(T)$ of electron and hole doped CoTiSb. The values are given for $T = 300\ K$. The calculations were performed by Boltztrap using the results of the VCA electronic structure.

difference in the sign is a direct consequence of the observed in-gap states that are not included in the calculations. For the substituted compounds the general variation agrees qualitatively with the calculation. For 5% Ti substitution by Sc as well as V, the size and sign of the measured Seebeck coefficient agree well with the calculated values. This demonstrates that the influence of the in-gap states on the thermoelectric properties can be neglected at high substitution level.

8.8 Summary

The Heusler compound CoTiSb was synthesized and investigated by experiments and first-principles calculations. The optical properties of CoTiSb were measured and compared to ab-initio calculations. The complex permittivity shows a strong absorption peak at 1.83 eV that is in perfect agreement with the calculated size of the direct band gap at the Γ point. The optical absorption quickly drops to zero at lower energies, as expected for semiconductors when the photon energies become smaller than the gap size. The wide-range infrared reflectivity measurements exhibit strong absorption at a photon energy of 34 meV and weakly at 28 meV. These energies are in well agreements to the calculated energy of the optical phonons at the Γ point. The calculated vibrational and mechanical properties of CoTiSb prove the mechanical stability of the compound in the cubic $C1_b$ structure.

Furthermore, the properties of the solid solution series $CoTi_{1-x}M_xSb$ (M = Sc, V) were systematically studied. The thermal conductivity of the substituted compounds is effectively depressed (about 30%) by substitution of Ti by Sc or V. A 5% Sc substitution resulted in a *p-type* behavior with a high Seebeck coefficient of +177.8 μV/K at 350 K This value is in well agreements to the calculations. The fully relativistic Korringa-Kohn-Rostoker (KKR) method in combination with the coherent potential ap-

proximation (CPA) was used to calculate the Fermi surface of $CoTi_{0.95}M_{0.05}Sb$ (M = Sc, V). The results showed that it is dominated by hole pockets a the Γ point for Sc and electron pockets at the X and K points for V substitution. These differences are responsible for the change of the transport properties of the compound for different type of substitution. A relatively high magnetoresistance of about 27% at 2 K was observed for $CoTi_{0.95}Sc_{0.05}Sb$. This makes these compounds promising candidates not only for thermoelectric applications, but also for spintronics or multi-functional devices.

9 Pt-Based Gapless Heusler Compounds with $C1_b$ Structure: Electronic Structure, Transport and Optical Properties

9.1 Introduction

Ternary Heusler compounds with 1:1:1 stoichiometry ($C1_b$ structure with $F\bar{4}3m$ symmetry) [31] and 18 valence electrons per primitive cell (VEC) are reported to be semimetals or semiconductors [33]. Due to their tunable band gap size from narrow band gap semiconductors [33] to *zero* band gap insulators [39], this 18 VEC-systems show multifarious physical properties. Especially, ternary compounds based on *heavy* metals (Pd, Pt) have been extensively studied, including crystalline structure [210, 211], heavy fermion behavior [212, 213], magnetism [214], superconductivity [215], and thermoelectricity [216, 217].

Recently several band structure computations [39, 218] on ternary Heusler compounds based on *heavy* metals have been carried out. Those state-of-the-art materials were predicted to be topological insulators, due to their insulating nature in the bulk, generated by strong spin orbit coupling and topologically protected metallic surface states. In particular, PtYSb is found to be a borderline compound, between trivial and topological insulator [39]. Such topological states have been investigated on binary systems like HgTe and $Bi_{1-x}Sb_x$ [219]. Those systems exhibit extraordinary thermoelectric properties. Similar promising properties were predicted for *heavy* metal containing ternary Heusler compounds such as PtYSb [219, 220, 221].

The peculiarities of the topological surface states are originating from the inversion of bulk bands, therefore it is needed to explain the bulk electronic structure what was done here by the use of hard X-ray photoelectron spectroscopy (HAXPES) as bulk sensitive method.

To identify the existence of the zero band gap behavior and topological states in Heusler compounds a convenient experiment has to be carried out. HAXPES has emerged as a powerful tool to investigate the bulk electronic structure of materials in a variety of applied fields such chemistry, physics, materials science and industrial applications [54]. The use of high-brilliance high-flux X-rays from the third-generation synchrotron radiation sources results in the emission of electrons having high kinetic energies, in turn leading to a high probing depth because of the increased electron mean free path [55]. Recently, several studies using high-resolution HAXPES have been realized. The electronic structure of solids like valence transitions in bulk systems [56, 57] as well as multilayer systems [55] and the valence band of buried thin films [58] have been investigated.

In the first part of this present study, the electronic structure of the Heusler compounds PtYSb, PtLaBi, and PtLuSb was determined by all-electron *ab initio* calculations. The valence states of the compounds were investigated by means of HAXPES and compared

to the calculation.

Furthermore,the study of the optical properties were reported as useful method to investigate the band gap of some Heusler compounds [222, 223] but are applied rarely. Up to now, no optical investigation on gapless Heusler compounds were carried out. The second and third part of this chapter reports on the optical and transport properties of the Heusler compound PtYSb. The details of the sample production and characterization are reported in chapter 5.

9.2 Results and Discussion

Powder X-ray diffraction revealed single phases with $C1_b$ structure for all compounds. The lattice parameters were determined to be 6.5256 Å and 6.8298 Å for PtYSb and PtLaBi, respectively. The observed values are in good agreement with those reported previously [210, 224]. The ingots were cut to sticks with a size of $(2 \times 2 \times 10)$ mm^3 for further investigations of the thermoelectric properties and electronic structure.

9.2.1 Electronic structure

The electronic structure of the compounds was calculated by means of WIEN2k [103]. Spin-orbit coupling was respected in all calculations. Further details of the calculations are the same as reported in [8] for other $C1_b$ compounds.

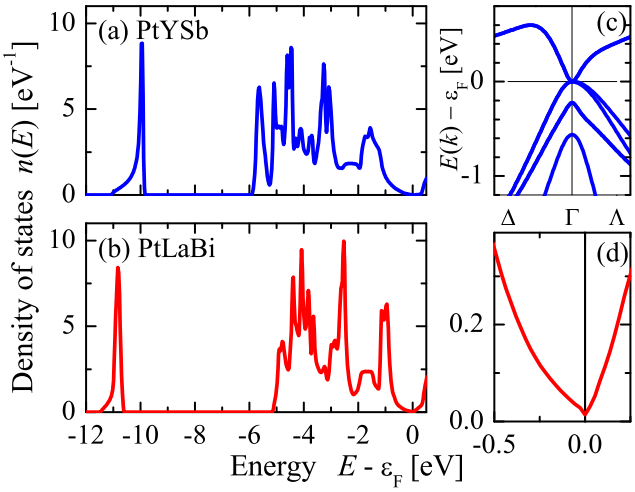

Figure 9.1: Calculated Density of states of PtYSb (a) and PtLaBi (b).
(c) shows part of the band structure of PtYSb close to ϵ_F in the 4-fold Δ $(\Gamma - X)$ and 3-fold Λ $(\Gamma - L)$ directions, and (d) shows the density of states of PtLaBi in the vicinity of the Fermi energy.

The calculated DOS of PtYSb and PtLaBi is compared in Fig. 9.1. Fig. 9.1(c) shows a part of the band structure of PtYSb close to the Γ point around the Fermi energy

(ϵ_F). The first unoccupied band touches the topmost occupied band and the result is the *zero band gap* type electronic structure [225].

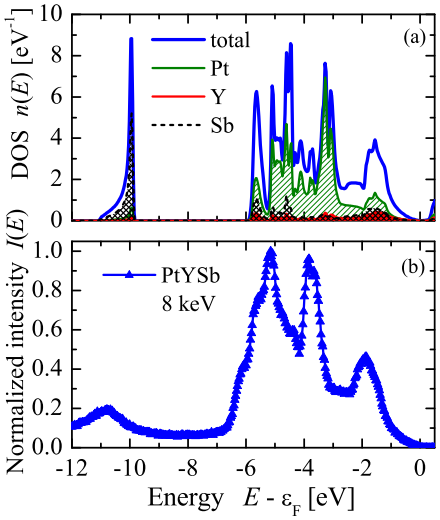

Figure 9.2: Total and partial density of states (a) and valence band HAXPES spectra (b) of PtYSb. Spectra are taken at $h\nu = 5.9533$ keV

The electronic structure of the compounds was investigated by HAXPES. Fig. 9.2 compares the calculated electronic structure of PtYSb to the measured valence band spectra. The structures in the valence band are clearly resolved and in well agreement to the calculated DOS.

The low lying maximum at -11 eV arises from the *s* states localized at the main group element Sb. These states as well as the characteristic Heusler *sp* hybridization gap - separating *s* from *p* states localized at the main group element - are clearly resolved. The higher lying valence band (above -7 eV) of the compound shows clearly a structure with three major maxima and some shoulders. The first maximum at about -1.7 eV below ϵ_F emerges from *d*-states distributed at Pt as well as Y whereas the second, sharp doublet feature maximum at about -3.9 eV arises from *d* states that are strongly localized at the Pt atoms only. The part of the valence band spectra below -4 eV appears smeared out. This energy region contains a mixture of *s*, *p*, and *d* states that contribute with different cross sections and therefore can not be easily related to the DOS. It is also stronger effected by life time broadening compared to energies close to ϵ_F. The effect of the photohole electron correlation leads also to a shift of the observed intensity maxima to lower energies compared to the corresponding maxima of DOS. This shift is in average 0.3 eV at the first and 0.5 eV at the second maximum. This kind of shifts were also found in narrow bandwidth valence band spectra of various materials [65].

Fig. 9.3 compares the measured valence band spectra of PtYSb (a) and PtLaBi (b). The spectra were taken with an excitation energy of about 5.9 keV. The maximum of the *s* states is shifted from about -10.7 eV to -11.6 eV when comparing the Y and the La containing compounds. The observed shift to lower energies when changing the

composition is in well agreement to the calculations of the density of states shown in Fig. 9.1. The width of the valence band exhibits the changes as expected from the calculated DOS (cf. Fig. 9.1). It is most narrow in PtLaBi and about 1 eV wider in PtYSb.

Most interesting is the behavior of the spectra close to ϵ_F as shown in Fig. 9.3(c and d). The intensities of PtYSb (9.3(c)) and PtLaBi (9.3(d)) exhibit a course as expected for a zero band gap insulator. Both, PtYSb and PtLaBi, exhibit a nearly linear behavior of the spectra and calculated DOS, as is expected for a Dirac-cone type density appearing for linear dispersing bands (see Figure 9.1(c). A bend of the DOS appears at the onset of the next lower valence bands at about -0.2 eV (compare Fig. 9.1c).

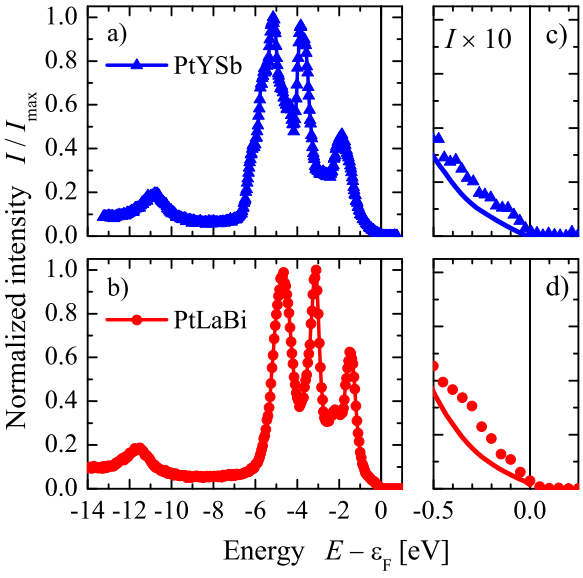

Figure 9.3: Valence band spectra of PtYSb and PtLaBi.
Panels c) and d) show the region close to the Fermi energy on an enlarged scale. The lines correspond to the DOS normalized to the maximum.

Figure 9.4(a) compares the measured valence band spectra of PtYSb and PtLuSb. The spectra were taken with an excitation energy of 5.950 keV. Both compounds exhibit the typical low lying maximum at about -11 eV that arises from the s states localized at the main group element Sb. This maximum is shifted by about 0.34 eV to low energies for the Lu compound. These states as well as the characteristic Heusler *sp* hybridization gap separating *s* from *p* states localized at the Sb are clearly resolved. Most interesting are the states inside of the hybridization gap. In the Lu ($4f^{14}$) containing compound, the $4f$ states appear as prominent doublet with maximum intensities at - 9.30 eV and -7.83 eV corresponding to a spin-orbit splitting of $\Delta_{SO} = 1.47$ eV. Those states are absent in the Y ($4f^0$) containing compound, due to the localization of the f states in the conducting band. The higher lying valence band (above -7 eV) of both compounds shows clearly a structure with three major peaks.

Figure 9.4(b) compares the valence band spectra of PtLuSb taken at two different excitation energies (5.949 keV and 3.238 keV). In case of the lower excitation energy (3.238 keV), the s as well as the d state intensities are reduced, where as the f states of Lu are strongly enhanced. The observed strong changes in the intensities are caused by the differences of the cross section for s, d and f electrons while changing the excitation energy.

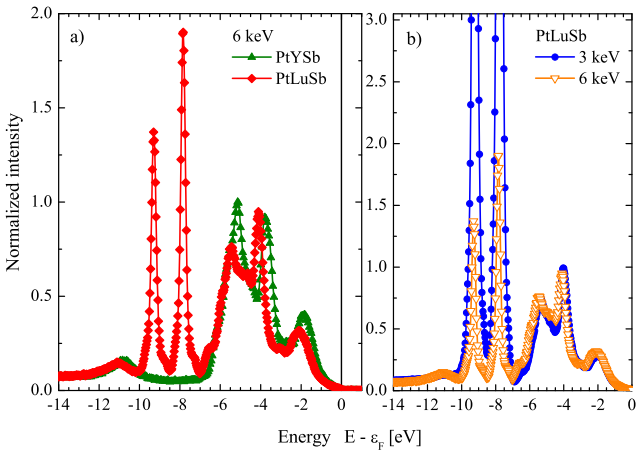

Figure 9.4: Valence band spectra of PtYSb and PtLuSb.
a) Photoemission spectra from valence electron states of PtYSb and PtLuSb taken at 5.949 keV. b) comparison of valence electron spectra of PtLuSb taken at difference excitation energies.

9.2.2 Optical properties

The optical properties of PtYSb are presented in Figure 9.5 that shows in (a) the complex permittivity $\varepsilon = \varepsilon_r + i\varepsilon_i$. ε_r is related to ε_i by the Kramers-Kronig relations. Hence, the features discussed for ε_i are reflected also in the behavior of ε_r. The dominant, unusual feature is a roughly linear increase of the optical absorption ε_i. This is related to the conical shape of the electronic structure in the vicinity of the Fermi energy. This feature ends at about 2.5 eV, corresponding to the border of the conical shape of the electronic structure and the onset of weakly dispersing, flat bands. The experimentally determined optical properties are compared to ab-initio calculations. The key features in the ab-initio calculations, namely a roughly linear increase of the absorption, are well reproduced. However, the peaks of the optical absorption at higher photon energies, that is for the weakly dispersing flat bands, are predicted at lower frequencies compared to the experimental data. This gives a hint that the final state bands in the conduction band are not described well by calculations using the generalized gradient approximation (GGA). This difference can be caused by the fact that GGA allows to calculate only the fundamental states.

The wide-range infrared reflectivity measurement is presented in Fig. 9.5(b), measured

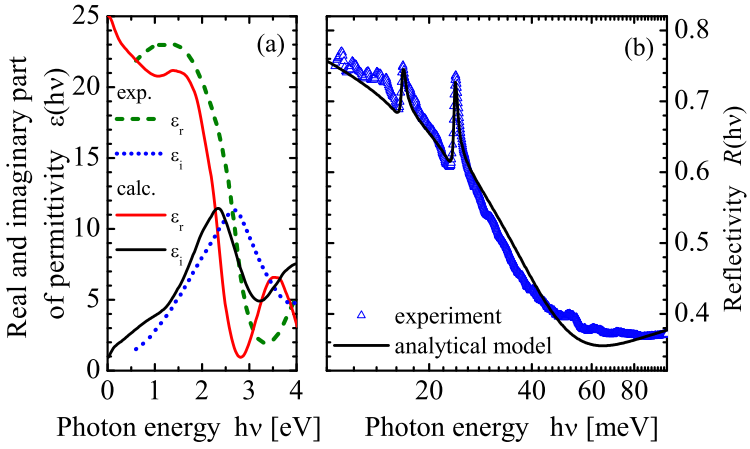

Figure 9.5: Optical properties of PtYSb.
a) Real ε_r and imaginary ε_i part of the permittivity. Experimental data (dashed lines) and ab-initio calculations (solid lines). b) Infrared reflectivity.

from 10 meV (far-infrared) to 1 eV (near- infrared). The reflectivity is nearly constant in the range from 60 meV to 1 eV and increases below 60 meV. The increase of the reflectivity for small photon energies is a typical feature of free-electron conductivity, the so-called Drude term. Furthermore, the reflectivity contains two sharp peaks at photon energies of 16.7 and 23.8 meV, probably originating from absorption of optical phonons.

In order to describe the reflectivity, the following contributions to the permittivity tensor are used: $\varepsilon = \varepsilon_{\mathrm{dru}} + \varepsilon_{\mathrm{TS}} + \varepsilon_{\mathrm{lor1}} + \varepsilon_{\mathrm{lor2}} + \varepsilon_{r,\infty}$ where $\varepsilon_{\mathrm{dru}}$ is the Drude contribution describing the contribution of free electrons to the optical properties, $\varepsilon_{\mathrm{dru}}(E) = E_D^2/(-E^2 - i\gamma E)$, where E_D, γ are plasma and damping energies, respectively. $\varepsilon_{\mathrm{TS}}$ is a contribution originating from the conical shape of the electronic structure. As can be seen in the ellipsometry results, for energies smaller than ≈ 2.5 eV, the absorption can be expressed by a linear function, $\Im(\varepsilon_{\mathrm{TS}}(E)) = aE$. Using the Kramers-Kronig relation, the real part is found to be $\Re(\varepsilon_{\mathrm{TS}}(E)) = \frac{2a}{\pi}(A + \frac{1}{2}E \ln \frac{A-E}{A+E})$, where A is the energy up to which the absorption is described by the linear approximation. The real parameter $\varepsilon_{r,\infty} > 1$ accounts for all other absorption contributions at higher frequencies, as well as the vacuum permittivity. The parameters describing ε_{TS} can be determined solely from the permittivity found by ellipsometry providing $A = 2.5$ eV, $\varepsilon_{r,\infty} = 13$ and $a = 5.5$ eV^{-1}. The remaining description of the Drude contribution is found by a fit to the reflectivity providing $E_D = 230$ meV and $\gamma = 47$ meV. Those values provide a quasi static conductivity of $\sigma = (E_D^2\varepsilon_0)/(\gamma\hbar)$=16.7 10^3 Sm^{-1} (ε_0 is the vacuum permittivity and $\hbar$ is Planck's constant). The last two contributions to the permittivity are Lorentzian contributions $\varepsilon_{\mathrm{lor},i}(E) = E_{L,i}^2/(E_{0,i}^2 - E^2 - i\gamma_i E)$, where $E_{L,i}$, $E_{0,i}$ and γ_i describe strength, position, and damping of the Lorentzian oscillator, respectively. The agreement between the experimental data and the simple model shows a reasonable

agreement (see Figure 9.5(b)).

9.2.3 Transport properties

Figure 9.6 (a) shows the temperature dependence of total κ_{tot}, electronic κ_e and lattice κ_L thermal conductivity of PtYSb. The electronic contribution $\kappa_e(T)$ was calculated using the Wiedemann-Franz law [41]. The overall shape of κ_{tot} is similarly to other Heusler systems [226]. κ_{tot} exhibits a maximum at about 30 K that indicates a perfect order of the crystal lattice. As shown in Figure 9.6 (b), the Seebeck coefficient is positive in the whole measured temperature range and increases with increasing temperature, reaching a maximum value of 142 μV/K at 350 K. This value is considerably higher than the one recently reported for this material in Reference [224]. This higher value is probably due to the high crystalline order of the crystal. The positive sign of $S(T)$ indicates the dominant role of the hole type conductivity.

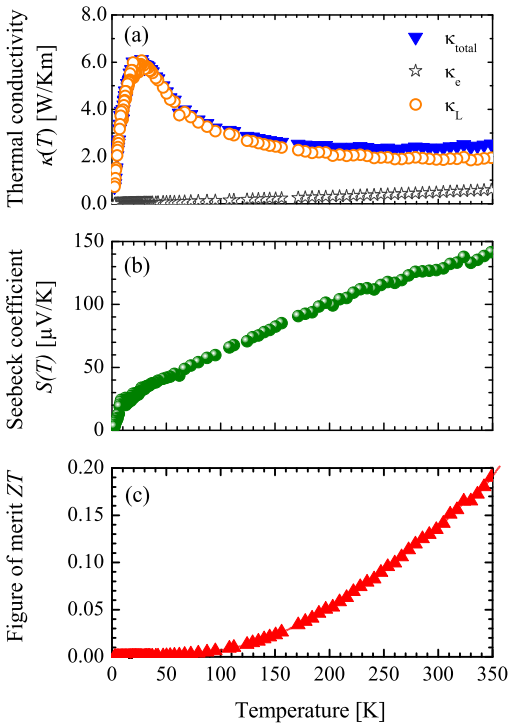

Figure 9.6: Temperature dependence of thermal conductivity $\kappa(T)$, Seebeck coefficient $S(T)$ and figure of merit ZT of PtYSb.

The temperature-dependent electrical resistivity $\rho(T)$ is shown in Figure 9.7(a) in the range from 2 K to 350 K. It exhibits clearly a semiconducting-type behavior. A value of 14 $\mu\Omega$m is obtained at 350 K, which is in the same order of magnitude as the previously reported values for other Heusler compounds containing *heavy* metals (Pd, Pt) [216, 224, 226]. Due to the large Seebeck coefficient, the relatively low thermal

conductivity, and electrical resistivity, the PtYSb compound reaches a high figure of merit ZT (0.2 at 350 K) as is shown in Figure 9.6 (c). The accompanied Peltier and Thompson coefficients are $\Pi(350\text{K}) = 51$ mV and $\tau(350\text{K}) = 90$ μV/K, respectively.

The Hall effect of the compound was measured in the temperature range from 5 K to 400 K in magnetic induction fields from -5 T to +5 T. The Hall coefficient was calculated from the slope of R_H. The Hall mobility $\mu_h = R_H/\rho$ and the carrier concentration $n = 1/eR_H$ were extracted from R_H using a single band model [41] (e is the elementary electric charge). As shown in figure 9.7(b), the Hall mobility μ_h of PtYSb exhibits a $T^{-3/2}$ temperature dependence. This is typical for *gapless* semiconductors [227]. μ_h reaches a value of 300 cm^2/Vs at 350 K, which is the highest value found for Heusler compounds up to now. At low temperatures up to about 150 K the carrier concentration has a constant value of about $n \approx 4.8{\times}10^{18}$ cm^{-3}. Above 150 K, the carrier concentration increases linearly with an order of 2×10^{16} cm^{-3}/K up to $n = 10^{19}$ cm^{-3} at 400 K. All electronic quantities show deviations for temperatures below 25 K where the maximum of the thermal conductivity appears. This hints on an influence by differences in the electron-phonon scattering.

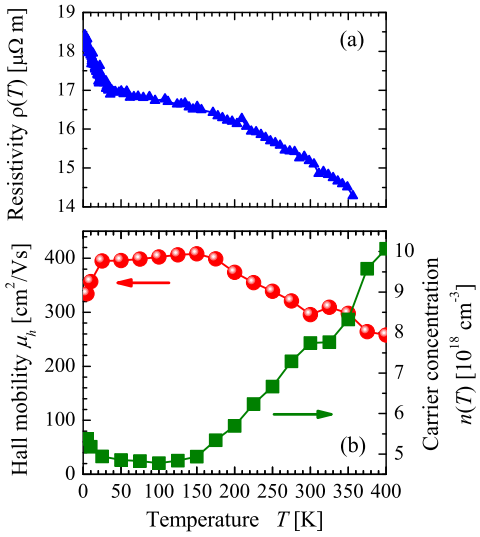

Figure 9.7: Temperature dependencies of electrical resistivity $\rho(T)$ (a), Hall mobility μ_h (left scale) (b), and carrier concentration n (right scale) (b) of PtYSb.

9.3 Summary

In this chapter, the electronic structure of the Heusler compounds PtYSb, PtLaBi, and PtLuSb was investigated by bulk sensitive HAXPES. The electronic structures in the measured valence band are clearly resolved and in well agreement to the calculated DOS. The comparison of the experimental results to first principles calculations gives clear

evidence for the zero band gap state of the compounds PtYSb and PtLaBi. Close to ϵ_F, the linear behavior of the measured spectra at high excitation energy where influences of the surface can be neglected proves the bulk origin of the Dirac-cone type density of states.

Furthermore, the optical properties of PtYSb were investigated. The complex permittivity was measured and compared to ab- initio calculations. A linear increase with photon energy is observed, which is related to a conical shape of the electronic structure in the vicinity of the Fermi energy [208]. This observed behavior is in perfect agreement to the calculations where the conical shape arises from nearly linearly dispersing bands for both valence and conduction electrons. The wide-range infrared reflectivity measurements show two sharp peaks at photon energies of 16.7 and 23.9 meV originating from absorption of phonons.

As expected for topological Heusler compounds, PtYSb exhibits promising thermoelectric properties. The Hall mobility μ_h showed a $T^{-3/2}$ temperature dependence, which is typical for gapless semiconductors. This is in perfect agreement to the measured and calculated optical properties. μ_h reaches a high value of 300 cm^2/Vs at 350 K. PtYSb exhibits excellent thermoelectric properties with a high figure of merit ZT of 0.2 at 350 K. All those promising properties of PtYSb open a high potential for new technological applications.

10 Linear Dichroism in Hard X-Ray Photoelectron Spectroscopy

10.1 Introduction

Photoelectron spectroscopy is of great importance in many fields of research because of its numerous advantageous properties [65, 80, 228]. Among its various applications, in particular, it is used to investigate the symmetries of the electronic structure of various materials. However, thus far, such studies have been restricted to atoms, molecules, adsorbates, and surfaces because low-energy (< 1 keV) electrons have limited probing depths. This is disadvantageous in that three-dimensional (3D) bulk states cannot be studied. This work demonstrate that this drawback can be eliminated by using hard X-rays with variable polarization for excitation. In this study, this issue was investigated using several Heusler compounds.

In the present work, a combination of the LDAD with the bulk-sensitive HAXPES technique was used to investigate the symmetry of the valence states of non-magnetized, polycrystalline Heusler compounds for the first time. The valence electronic structure of the Heusler compounds is easily changed by varying the composition. The compounds $NiTi_{0.9}Sc_{0.1}Sn$ and NiMnSb were selected in this study. The comparison of those allows to follow the change of the d valence bands when Mn-d^5 is replaced by Ti-d^2 (in practice $(Ti_{0.9}Sc_{0.1})$-$d^{1.9}$). NiMnSb was suggested to be a halfmetallic ferromagnet [35]. The samples used for the HAXPES measurements were in the virgin state. NiTiSn is supposed to be a semiconductor [200]; therefore, this sample was heavily hole doped by Ti↔Sc substitution with a composition of $NiTi_{0.9}Sc_{0.1}Sn$. This ensures that the Fermi energy clearly lies in the valence band and it suppresses unwanted *in-gap* states that were reported previously [50]. The details of the sample production and characterization are reported in section 7.2. The HAXPES experiment was performed using the beamline BL47XU at SPring-8 (Japan) [54].

The use of the phase retarder for s polarized light considerably decreases the overall intensity because of the absorptivity of the diamond crystal. The integration of the count rate over the valence band of $NiTi_{0.9}Sc_{0.1}Sn$ results in a ratio of $I^p/I^s \approx 20$ when p polarization without the phase retarder is compared with s polarization with the retarder. Therefore, the spectra were normalized to the secondary background at energies below the valence band (see section 3.3.3).

10.2 Results and discussion

10.2.1 Electronic structure calculations

The electronic structure of NiMnSb was calculated by the full potential linearized augmented plane wave (FLAPW) method as implemented in WIEN2k [103].

According to the results from X-ray diffraction, the $C1_b$ structure with space group $F\overline{4}3m$ was assumed for both compounds. The Ni atoms were placed on Wyckoff position 4a, Ti or Mn on 4c, and Sn or Sb on 4d. The 4b Wyckoff position stayed vacant. Relaxed lattice parameters were used in the calculations, the optimization of the volume resulted in $a = 5.9534$ Å for NiTiSn and $a = 5.9171$ Å for NiMnSb.

The electronic structure calculation of the substitutionally disordered $NiTi_{0.9}Sc_{0.1}Sn$ was performed by means of the virtual crystal approximation (VCA). The substitution of Ti by 10% Sc results in a reduction by 0.1 e^- because the difference in the valence electrons of those atoms is 1. Therefore, the charge and number of electrons at the Ti site (4c) of NiTiSn was set to 21.9 e^- to model the $NiTi_{0.9}Sc_{0.1}Sn$ solid solution. The resulting band structure is an approximation as it is absent in real solid solutions with random site occupation and thus a missing periodicity of the crystal structure.

Further, the electronic structure calculation of $NiTi_{0.9}Sc_{0.1}Sn$ has been performed by means of the fully relativistic Korringa-Kohn-Rostoker (KKR) method in combination with the coherent potential approximation (CPA) as implemented in the MUNICH - SPRKKR program package [89].

10.2.2 Photoelectron cross sections

The partial cross sections and angular asymmetry parameters were calculated in the dipole-length approximation by solving the Dirac-Hartree-Fock equations for bound and free electrons of free atoms. The program is based on a modified accurate fully relativistic Dirac-equation-solver developed by Salvat and Mayol [90, 91]. Due to the fast oscillating final state wave functions at 8 keV kinetic energy ($\lambda_{el} = 0.137$ Å), a very fine radial mesh (about 10^3 points per Å on a logarithmic mesh) had to be used for the integration of the radial matrix elements and calculation of the phases. The partial cross sections σ_{nlj} and angular asymmetry parameters β_{nlj} for the dipole length approximation are given in Tables 10.1 and 10.2 for the constituents of $NiTi_{0.9}Sc_{0.1}Sn$ and NiMnSb. The results for a photon energy of $h\nu = 8$ keV fit well into the energy dependent scheme of previously published values in the non-relativistic [92] and relativistic [93, 94] approaches. All β-parameters for s states are close to 2, as expected. For all transition metals the cross sections of the d-states are clearly lower than those of the s states. This concerns also the s valence states of the main group elements that are considerably higher than the d state cross sections of the $3d$ transition metals. This fact leads at high photon energies to an enhancement of the intensities of the low lying s bands compared to the d bands.

10.2.3 LDAD valence band of Heusler compounds with $C1_b$ structure

Figure 10.1 compares the valence band spectra and calculated electronic structure of $NiTi_{0.9}Sc_{0.1}Sn$. The density of states (DOS) exhibits a typical 4-peak structure in the energy range of the d states as well as the split-off s band with a_1 symmetry. These structures can be clearly observed in the photoelectron spectra. The sum of the polarization-resolved spectra corresponds to a spectrum with unpolarized photons. The width of the d-part of the density of states ($0 \ldots -5$ eV) corresponds to the width of the measured

Table 10.1: Partial cross sections and angular asymmetry parameters β_{nlj} of atomic Sc, Ti, Mn, and Ni valence electrons at $h\nu = 8$ keV.

Atom	State nlj	σ_{nlj} [MBarn]	β_{nlj}
Sc	$3d_{3/2}$	0.000009	1.2909
	$3d_{5/2}$	0.000013	1.3502
	$4s_{1/2}$	0.001175	1.9995
Ti	$3d_{3/2}$	0.000022	1.2500
	$3d_{5/2}$	0.000032	1.3114
	$4s_{1/2}$	0.001261	1.9994
Mn	$3d_{3/2}$	0.000097	1.2165
	$3d_{5/2}$	0.000139	1.2798
	$4s_{1/2}$	0.001758	1.9992
Ni	$3d_{3/2}$	0.000284	1.1619
	$3d_{5/2}$	0.000404	1.2293
	$4s_{1/2}$	0.002310	1.9989

Table 10.2: Partial cross sections and angular asymmetry parameters β_{nlj} of the atomic Sn and Sb valence electrons at $h\nu = 8$ keV.

Atom	State nlj	σ_{nlj} [MBarn]	β_{nlj}
Sn	$5s_{1/2}$	0.00483	1.9923
	$5p_{1/2}$	0.00205	0.5069
	$5p_{3/2}$	0.00339	1.4189
Sb	$5s_{1/2}$	0.00575	1.9917
	$5p_{1/2}$	0.00269	0.4931
	$5p_{3/2}$	0.00445	1.4357

spectra. The spectrum exhibits a rather high intensity in the s-part below -7 eV that is caused by the higher cross section for s states as compared to that for d states at a high excitation energy. The intensity of the d states is governed by the states localized at the Ni atoms. Dirac-Fock calculations for the photoexcitation of Ni, Ti, and Sc valence electrons indicate that at $h\nu = 8$ keV, the cross section for Ni $3d$ states is 20 times higher than that for light $3d$ transition metals.

It is evident that striking differences appear in the spectra if the polarization is changed from p to s. The spectra shown in Figure 10.1 indicate that the s states have a higher intensity for p polarization and the s polarization results in a higher intensity in the energy range of the d states. In particular, the intensity of the Ni $3d$ states at -2 eV is enhanced and the structure of the d states becomes better resolved under illumination with s polarized photons.

With a change from $NiTi_{0.9}Sc_{0.1}Sn$ to NiMnSb, and thus, from Ti $3d^2$ to Mn $3d^5$, one expects a change in the spectra in the energy range of the d states. Figure 10.2 shows a comparison of the valence band spectra and the electronic structure of NiMnSb.

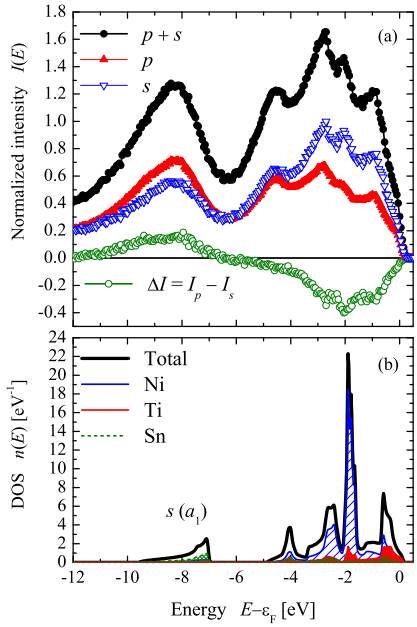

Figure 10.1: Electronic structure and polarization-dependent photoelectron spectra of $NiTi_{0.9}Sc_{0.1}Sn$.
(a) HAXPES Spectra obtained with s and p polarized light together with the sum and difference and (b) calculated total and partial density of states (DOS). Note that the Sc substitution creates holes, its d-states appear in the unoccupied part above the band gap.

The DOS exhibits a 5-peak structure in the range of the d states that is not completely resolved in the spectra. A pronounced maximum appears at approximately -3 eV in the DOS and spectra. It emerges from the Mn t_2 states that are responsible for the localized magnetic moment in NiMnSb. The changes in the spectra while changing the polarization are the same as those observed for $NiTi_{0.9}Sc_{0.1}Sn$. Again, the intensity of the Ni $3d$ states at -2 eV is noticeably enhanced for s polarized photons. The intensity of the Mn $3d$ states is enhanced in a similar manner.

Neglecting an incomplete polarization, in the geometry used, the angular asymmetry parameter $\beta_0 = 2$ (see chapter 3.3.3) should lead to a vanishing intensity for excitation of the s states by s polarized photons; however, this is clearly not the case. In the solid with T_d symmetry, however, the photoexcitation of the s band is better described by a $a_1 \rightarrow t_2$ transition as compared to an atom in which one simply has transitions into final p states [85, 98]. Restricting the partial waves of the initial a_1 state to $l = 0$ will allow already for direct transitions into partial waves with $l' = 1, 2$ of the final t_2 state (see also section 3.3.3) and the β parameter becomes [229]

$$\beta_{a_1,l=0} = \frac{2D^2_{t_2,l'=1} - 6/7D^2_{t_2,l'=2}}{D^2_{t_2,l'=1} + D^2_{t_2,l'=2}}, \tag{10.1}$$

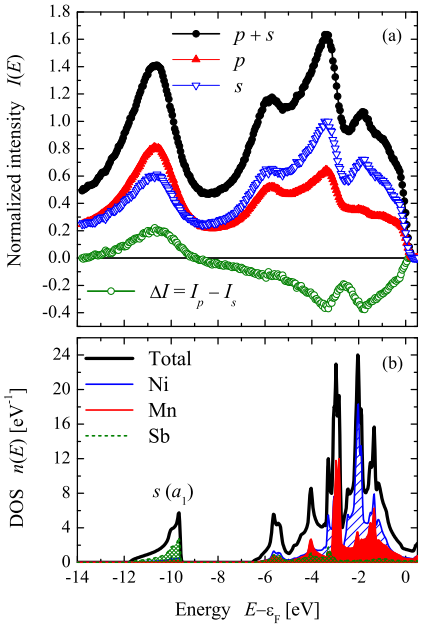

Figure 10.2: Electronic structure and polarization-dependent photoelectron spectra of NiMnSb.
(a) HAXPES Spectra obtained with s and p polarized light together with the sum and difference and (b) calculated total and partial density of states (DOS).

where D are the radial matrix elements. The additional $D_{t_2,l'=2}$ term immediately allows for $\beta_{a_1,l=0} < 2$.

Generally, the angular dependence of the final state contains contributions from much higher l' values that are compatible with the irreducible representations of the T_d symmetry group. Indeed, because of polycrystalline samples without preferential crystallographic directions, a rather uniform contribution is expected. This affects not only the angular distribution of the emission from the initial a_1 states but also that of the e and t_2 states.

From the enhancement of the intensity from the d states with s polarized light, one would expect negative β_{3d} parameters because the restriction on the nondipole parameter to $\delta \leq 1 - \beta/2$ (for $\beta > 0$) [230] does not allow for I^s_{3d} to become larger than I^p_{3d}, at least for direct emission. The calculated atomic-type β_{3d} parameters for Ni and Mn are in the range of 1.16 to 1.28, but they are not negative. Assuming more complete $e \rightarrow (t_1, t_2)$ and $t_2 \rightarrow (a_1, e, t_1, t_2)$ dipole transitions, the differences become obvious. The equation for $\beta_{e,l=2}$ and $\beta_{t_2,l=2}$, however, cannot be given as easily as above for $\beta_{a_1,l=0}$ without accounting for the contributions of l other than the 2 that are present in the initial e and t_2 states. In NiMnSb, the Mn states at -3 eV have a nearly pure t_2 character, whereas the Ni d states of both compounds at -2 eV have t_2 as well as e characters. A detailed analysis reveals that the relative change in the intensity in

NiMnSb is clearly higher at -2 eV ($\approx 30\%$) as compared to that at -3 eV ($\approx 20\%$), even without any background subtraction. Similarly, in $NiTi_{0.9}Sc_{0.1}Sn$, the relative change is slightly higher at approximately -1 eV. At -1 eV, most states have e character whereas at -3 eV, the states mainly have t_2 character. The variation of the relative changes for both compounds with differences observed over the entire valence band clearly indicates a symmetry dependence of the angular asymmetry parameters.

10.3 Summary and conclusions

In the present study, LDAD in hard X-ray photoelectron spectroscopy was used to study the angular asymmetry in photoemission from the valence states of polycrystalline Heusler compounds. The polarization-dependent measurements reveal that even high energies and polycrystalline samples do not yield a one-to-one correspondence of measured photoemission spectra and calculated density of states. This is mainly because there not only exist differences in the partial cross sections but there also exists the symmetry dependence of the angular asymmetry parameters. It was shown that the change in the linear polarization allows for different states of the valence band of complex materials to be easily distinguished. The polarization-dependent HAXPES experiments can clearly be applied not only to valence states but also to core states. Overall, the high bulk sensitivity of HAXPES combined with linearly polarized photons will have a major impact on the study of the electronic structure of bulk materials, thin films, deeply buried materials, and interfaces.

11 Summary and Outlook

The major aim of the present work was to investigate the electronic structure and physical properties of Heusler compounds for thermoelectric and spintronic applications.

In the first part, the half-metallic ferromagnet Co_2MnGe has been studied in detail. The crystalline structure of Co_2MnGe was investigated by XRD, EXAFS and anomalous XRD and it was found that the compound exhibits the $L2_1$ structure typical for well ordered Heusler compounds. Band structure calculations based on the $L2_1$ structure result in a half-metallic ferromagnetic ground state. The compound is a localized magnetic moment system with a ground state magnetic moment of 5 μ_B in the primitive cell. This is in excellent agreement to the SQUID measurement that revealed a magnetic moment of 4.98 μ_B at 5 K. Thus, Co_2MnGe fulfills the requirement for half-metallicity according to the Slater-Pauling rule. The bulk sensitivity of HAXPES was used to explore the core levels as well as the valence band electronic structure of polycrystalline Co_2MnGe. The measured valence band spectra are clearly resolved and in well agreement to the first-principles calculations of the electronic structure. The spin-orbit splitting as well as the exchange splitting of the core levels are explored in detail. Multiplet calculations of $2p$ and $3s$ core-levels were performed for Mn in 2+ and 3+ ionic states in order to determine the importance of the many-electron contributions to the core level photoelectron spectra of the compound. The comparison of the calculation to the experiment revealed that the Mn can not be attributed to be in a definite ionic state. The transport measurement shows the expected metallic behavior with a resistivity of 0.48 $\mu\Omega$m and a Seebeck coefficient of - 16 μVK^{-1} at room temperature. The temperature independence of the resistivity below 50 K supports the occurrence of half-metallic ferromagnetism in this compound. The vibrational and mechanical properties of the compound were calculated. The comparison of observed and calculated mechanical properties approve a covalent-like bonding of Co_2MnGe.

The second part of this thesis focuses on thermoelectric materials based on Heusler compounds. The efficiency of a thermoelectric device used for energy generation or refrigeration is determined by the materials used to build the device. In order to achieve the best performance of thermoelectric modules the n- and p-type materials should be designed to exhibit similar chemical and physical properties. The latter requirement can easily be fulfilled using element substitution in order to tune the electronic properties to the desired values in a controlled way. In this work, an isoelectronic as well as hole and electron substitutions in Heusler compounds have been investigated for further optimization of the thermoelectric performance. Two kinds of substituted compounds have been created. In NiTiSn an isoelectronic substitution of Ti by the heavy elements Zr and Hf was used to reduce the thermal conductivity. On the other hand, substitution of Ti in NiTiSn as well as in CoTiSb by Sc or V, results in hole or electron doping, respectively.

The electronic structure and transport properties of the series $NiTi_{1-x}M_xSn$ (M = Sc,

V) were measured in detail and compared to all-electron ab-initio density functional calculations. According to the XRD measurements, all compounds of the series crystallize in the $C1_b$ structure type. Substitution of Ti by V or Sc leads to a linear change of the lattice parameter according to Vegards law. A swap of about 5% Ti into the vacant site was found from the diffraction data of pure NiTiSn. Calculations as well as PES revealed that this type of anti-site disorder is responsible for the occurrence of *"in gap"* states that result in the favorable thermoelectric properties of the pure compound. The electronic structure of the compounds was studied using bulk sensitive HAXPES. The observed *in gap* states prove that the electronic states close to the Fermi edge play a key role to control the thermoelectric properties. The observed shifts of the valence states agree with the calculated shift of the Fermi energy when substituting Ti by Sc or V. The transport properties of the series were investigated by measuring thermal conductivity, electrical resistivity, and Seebeck coefficient in the low temperature range up to room temperature. In general, the change of measured transport properties with composition agree qualitatively with the calculations.

The reduction of the thermal conductivity in $NiTi_{1-x}M_xSn$ (M = Sc, V) compounds is achieved by substitution of Ti and independent of the type of doping (Sc or V). Therefore, the impact of the lowered thermal conductivity on the figure of merit is nearly the same. The sign of the Seebeck coefficient switches by Sc substitution from n- to p-type. This is related to the appearance and the dominant contribution of free holes to the intermetallic semiconductor conductivity. The n-type behavior of the pure compound is provided by the *"in gap"* states. Sc substitution of Ti leads to p-type behavior and suppression of the *"in gap"* states. The observed behavior of the resistivity of both types of substituted materials is explained by the calculations respecting disorder scattering. In order to create high efficient thermoelectric materials, it is necessary not only to improve the figure of merit but also to achieve a high power factor. The power factors found in calculation and experiment reveal clearly a different behavior for both types of substitution. Different from n-type substitution, which exhibits the highest power factor, the p-type still has rather low values. This difference is caused by the different behavior of the conductivity when the carriers are from either the valence or the conduction band. The major distinction appears through the fact that p-type doping (Sc) creates holes in the triply degenerate valence band at Γ whereas n-type doping (V) fills electrons in the single conduction band above the indirect gap at X. This behavior is typical for the semiconducting transition-metal based Heusler compounds with $C1_b$ structure that all exhibit similar band structures rather independent on the composition.

On the other hand, the two kinds of substitution described above were used in one compound to enhance the thermoelectric figure of merit of p-type NiTiSn-based Heusler compounds. A series of Sc substituted alloy $NiTi_{0.3-x}Sc_xZr_{0.35}Hf_{0.35}Sn$ was synthesized and investigated with respect to electronic structure and transport properties. Indeed, it was shown that the thermal conductivity of the compounds is effectively lowered when substituting Ti by Sc. The Sc substitution leads at once to an increase of the power factor and switches the system to p-type behavior. A maximum value of 0.63 $mW/(K^2m)$ for the p-type material is obtained at 350 K and a Sc content of $x = 0.05$. Similar to NiTiSn, the HAXPES investigation showed *in gap* states close to the Fermi energy, which play a

key role on the behavior of the transport properties.

The narrow band gap Heusler compound CoTiSb was also investigated by first principles calculations and experiments. The measured optical properties explored by the complex permittivity. The compound exhibits a direct band gap of 1.83 eV that is in perfect agreement with the calculated size of the direct band gap at the Γ point. The wide-range infrared reflectivity measurements exhibit strong absorption at a photon energy of 34 meV and weakly at 28 meV. These energies are in good agreement with the calculated energy of the optical phonons at Γ. Likewise NiTiSn, CoTiSb exhibits *in gap* states close to the Fermi energy. Those state are responsible for the measured high electrical conductivity. Furthermore, the properties of the solid solution series $CoTi_{1-x}M_xSb$ (M = Sc, V) were systematically studied. Similar to NiTiSn based compounds, a *p*-type behavior was achieved in the CoTiSb based Heusler compounds by Sc substitution. The thermal conductivity of the substituted compounds are effectively depressed (about 30%) by substitution of Ti by Sc or V. A 5% Sc substitution resulted in a *p-type* behavior with a maximal Seebeck coefficient of +177.8 μV/K (350 K). This value is in good agreement with the calculations.

The open challenge to theory and experiment is to find new concepts that depress the thermal conductivity and, at the same time, improve the electric conductivity at low *p*-type doping of Heusler compounds. The presented systematic study of the solid solution series based on NiTiSn and CoTiSb shows the possibility to create *n*-type and $p-$type thermoelectric materials within one compound series.

Going from narrow band gap to gapless Heusler compounds, the next step are the so called topological insulators. That are Pt-based Heusler compounds with $C1_b$ structure. Those state-of-the-art materials were predicted to be topological insulators, due to their insulating nature in the bulk, generated by strong spin orbit coupling and topologically protected metallic surface states. Promising properties were predicted for this class of compounds. In this work, the three Pt-based compounds PtYSb, PtLaBi and PtLuSb were investigated with respect to their electronic structure. Bulk sensitive HAXPES was measured with an excitation energy of about 6 keV. The measured valence bands are clearly resolved and in well agreement to the calculated DOS. The comparison of the experimental results to first principles calculations show linear dispersing bands close to the Fermi edge as expected for a Dirac-cone type density.

In particular, PtYSb is found to be a borderline compound, between trivial and topological insulator. This compound was investigated with respect to optical and transport properties. The complex permittivity was measured and compared to ab-initio calculations. A linear increase with increasing photon energy was observed, indicating a conical shape of the electronic structure in the vicinity of the Fermi energy. This observed behavior is in good agreement to the calculations where the conical shape arises from nearly linearly dispersing bands for both valence and conduction electrons. The wide-range infrared reflectivity measurements show two sharp peaks at photon energies of 14.8 and 21.0 meV originating from absorption of phonons. The Hall mobility μ_h showed a $T^{-3/2}$ temperature dependence, which is typical for gapless semiconductors. This is in perfect agreement to the measured and calculated optical properties. μ_h reaches a high value of 300 cm^2/Vs at 350 K. PtYSb exhibits excellent thermoelectric properties with a high

figure of merit ZT of 0.2 at 350 K. All those promising properties of PtYSb open a high potential for new technological applications.

In the last part of this thesis, linear dichroism in hard X-ray photoelectron spectroscopy was used to study the angular asymmetry in photoemission from the valence states of two kinds of polycrystalline Heusler compounds, NiTiSn (semiconductor) and NiMnSb (halfmetallic ferromagnet). The polarization dependent measurements reveal that even high energies and polycrystalline samples do not yield a one-to-one correspondence of photoemission spectra and density of states. This is mainly because there not only exist differences in the partial cross sections but there also exists the symmetry dependence of the angular asymmetry parameters. It was shown that the change in the linear polarization allows to distinguish different states of the valence band of complex materials easily. The polarization dependent HAXPES experiments can clearly be applied not only to valence states but also to core states. Overall, the high bulk sensitivity of HAXPES combined with linearly polarized photons will have a major impact on the study of the electronic structure of bulk materials, thin films, deeply buried materials, and interfaces.

Overall, this thesis shows that the combination of first-principle calculations, transport measurements and high resolution high energy photoelectron spectroscopy analysis is a very powerful tool for the design and development of new materials for a wide range of applications from spintronic applications to thermoelectric applications.

12 Acknowledgement

13 Zusammenfassung

Die vorliegende Arbeit beschäftigt sich mit der Synthese sowie Untersuchungen der elektronischen Struktur und Eigenschaften von Heusler-Verbindungen für Spintronik und thermoelektrische Anwendungen. Der erste Teil berichtet über die elektronische und kristalline Struktur sowie die mechanischen, magnetischen und Transport Eigenschaften der polykristallinen Heusler Verbindung Co_2MnGe. Die kristalline Struktur wurde ausfhrlich mit erweiterter Röntgen Absorptions-Feinstruktur Spektroskopie (EXAFS) und anomaler Röntgenbeugung untersucht. Das magnetische Moment stimmt mit der Slater-Pauling Regel überein und deutet auf einen halb-metallischen ferromagnetischen Zustand hin der durch ab-initio Rechnungen vorhergesagt wurde. Transportmessungen und harte Röntgen-Photoelektronen-Spektroskopie (HAXPES) wurden durchgeführt, um die elektronische Struktur der Verbindung zu erklären.

Ein groer Teil der Arbeit beschäftigt sich mit der systematischen Untersuchung von Heusler Verbindungen fr thermoelektrische Anwendungen und insbesondere der Suche nach neuen p-leitenden Heusler Verbindungen mit hoher thermoelektrischer Effizienz. Die Substitutionsserien $NiTi_{1-x}M_xSn$ und $CoTi_{1-x}M_xSb$ (M = Sc, V und $0 \leq x \leq 0.2$) wurden synthetisiert und in Bezug auf elektronische Struktur und Transporteigenschaften theoretisch und experimentell untersucht. Die Ergebnisse zeigen die Möglichkeit n-leitende und p-leitende Verbindungen aus der gleichen Heusler Verbindung herzustellen. Die reinen Verbindungen zeigten n-leitendes Verhalten, während unter Sc Substitution das System ein p-leitendes Verhalten aufweist. Ein maximaler Seebeck-Koeffizient von +230 μV/K (bei 350 K) wurde für $NiTi_{0.3-x}Sc_xZr_{0.35}Hf_{0.35}Sn$ erreicht. HAXPES Valenzband Messungen deuten auf massive $in-gap$ Zustände in den Stammverbindungen NiTiSn und CoTiSb hin. Dies zeigt, dass die elektronischen Zustände an der Fermi-Kante eine wichtige Rolle für das Verhalten der Transport Eigenschaften haben. Weiterhin wurde die elektronische Struktur der *gapless* Heusler-Verbindungen PtYSb, PtLaBi und PtLuSb mit HAXPES untersucht. Das lineare Verhalten der Spektren in der Nähe von ϵ_F weist auf eine konus-artige Bandstruktur mit linearer Dispersion. Weiterhin wurden die optischen und Transport Eigenschaften von PtYSb vorgestellt. Die Verbindung zeigt vielversprechende thermoelektrische Eigenschaften mit einem hohen Gütefaktor (ZT = 0,2) und einer Hall-Beweglichkeit von 300 cm^2/Vs bei 350 K. Der letzte experimentelle Teil, beschäftigt sich mit dem Linear Dichroismus in der Winkelverteilung der Photoelektronen in Kombination mit HAXPES. Ein deutlicher Lineardichroismus wurde in den Valenzbndern von NiTiSn und NiMnSb beobachtet. Dies ermglicht einer Analyse der Symmetrie der Zustnde. Der beobachtete Unterschied in den Spektren ist durch die Symmetrieabhängigkeit des Winkel-Asymmetrie Parameters erklärt. Die Kombination aus Bandstruktur Berechnungen, harter Rntgen-Photoelektronenspektroskopie und Messungen der Transporteigenschaften ist eine leistungsfähige Methode zur Entwicklung neuer Materialien für Spintronik und thermoelektrische Anwendungen.

List of Figures

List of Tables

List of Abbreviations

a	Lattice Parameter
A_e	Elastic Anisotropy
a_B	Bohr's Radius: $a_B = 0.5291772$ Å
aXRD	Anomalous X-Ray Powder Diffraction
B	Bulk modulus
$C(T)$	Specific Heat
$C(T)_e$	Electronic Specific heat
$C(T)_L$	Lattice Specific Heat
c_{ij}	Elastic Constants
CDAD	Circular Dichroism in the Angular Distribution
CPA	Coherent Potential Approximation
DOS	Density of States
ΔT	Temperature Gradient
ΔV	Electric Potential
E	Youngs Modulus
EV-GGA	Engel-Vosko Generalized Gradient Approximation
EXAFS	Extended x-Ray Absorption Fine-structure Spectroscopy
fcc	Face-entered Cubic
FLAPW	Full Potential Linearized Augmented Plane Wave Method
j	Total Angular Momentum
G	Rigidity Modulus
GGA	Generalized Gradient Approximation
HAXPES	Hard X-Ray Photoelectron Spectroscopy
HMF	Half-Metallic Ferromagnet
HV1	Vickers Hardness
KKR	Korringa-Kohn-Rostoker
L	Lorenz Number
l	Orbital Angular Momentum
LDAD	Linear Dichroism in the Angular Distribution
MDAD	Magnetic Dichroism in the Angular Distribution
MR	Magnetoresistance
MTJs	Magnetic Tunnel Junctions
N_v	Valence Electrons Number per Formula Unit
n	Main Quantum Number
O_h	Octahedral Symmetry
PBE	Perdew-Burke-Enzerhof
PES	Photoelectron Spectroscopy

PF	Power Factor
PPMS	Physical Properties Measurement System
Q	Heat Flux
RT	Room Temperature
Ry	Rydberg (1 Ry = 13.605692 eV)
S	Seebeck Coefficient
SQUID	Superconducting Quantum Interference Device
SPRKKR	Spin Polarized Korringa-Kohn-Rostoker
T_d	Tetrahedral Symmetry
TE	Thermoelectric
TMR	Tunneling Magnetoresistance
TTO	Thermal Transport Option
UHV	Ultra-High Vacuum
V_c	Vacancy Site
UPS	Ultraviolet Photoelectron Spectroscopy
VEC	Valence Electron Concentration per Formula Unit
XMCD	X-ray Magnetic Circular Dichroism
XAS	X-ray Absorption Spectroscopy
XPS	X-ray Photoemission Spectroscopy
XRD	X-ray Powder Diffraction
z_{eff}	Effective Probing Depth
ZT	Thermoelectric Figure of Merit
β_κ	Angular Asymmetry Parameter
Δ_{SO}	Spin-Orbit Splitting
Δ_{EX}	Exchange Splitting
Δ_{MS}	Metallic Satellites
ϵ_F	Fermi Energy
$h\nu$	Photon energy
κ	Thermal Conductivity
κ_e	Electronic Thermal Conductivity
κ_L	Lattice Thermal Conductivity
$\lambda(E)$	Electron Mean Free Path
μ_B	Bohr Magneton
$h\nu(q)$	Phonon Dispersion
$\rho(T)$	Electric Resistivity
σ	Electrical Conductivity
σ_{nl}	Partial Cross Sections
σ_{eff}	Effective Cross Section
Θ_D	Debye Temperature

Bibliography

[1] Fr. Heusler. *Verh. d. DPG*, 5:219, 1903.

[2] R. A. de Groot, F. M. Müller, P. G. van Engen, and K. H. J. Buschow. *Phys. Rev. Lett.*, 50:2024, 1983.

[3] C. Felser, B. Heitkamp, F. Kronast, D. Schmitz, S. Cramm, H. A. Dürr, H.-J. Elmers, G. H. Fecher, S. Wurmehl, T. Block, D. Valdaitsev, S. A. Nepijko, A. Gloskovskii, G. Jakob, G. Schönhense, and W. Eberhardt. *J. Phys.: Condens. Matter*, 15:7019 – 7027, 2003.

[4] C. Felser, G. H. Fecher, and B. Balke. *Angew. Chem. Int. Ed.*, 46:668 – 699, 2007.

[5] D. Kieven, R. Klenk, S. Naghavi, C. Felser, and T. Gruhn. *Phys. Rev. B*, 81(7):075208, 2010.

[6] J. Winterlik, G. H. Fecher, and C. Felser. *Solid State Comm.*, 145:475 – 478, 2008.

[7] C. F. G. Blum, S. Ouardi, G. H. Fecher, B. Balke, X. Kozina, G. Stryganyuk, S. Ueda, K. Kobayashi, C. Felser, S. Wurmehl, and B. B$\breve{}$chner. *Appl. Phys. Lett.*, 98:252501, 2011.

[8] S. Ouardi, G. H. Fecher, B. Balke, X. Kozina, G. Stryganyuk, C. Felser, S. Lowitzer, D. Ködderitzsch, H. Ebert, and E. Ikenaga. *Phys. Rev. B*, 82:085108, 2010.

[9] Fr. Heusler. *Z. Anorg. Allg. Chem.*, 161:159 – 160, 1927.

[10] J. Kübler, A. R. Williams, and C. B. Sommers. *Phys. Rev. B*, 28:1745, 1983.

[11] T. Ishikawa, S. Hakamata, K.-i. Matsuda, T. Uemura, and M. Yamamoto. *J. Appl. Phys.*, 103:07A919, 2008.

[12] N. Tezuka, N. Ikeda, F. Mitsuhashi, and S. Sugimoto. *Appl. Phys. Lett.*, 94:162504, 2009.

[13] T. Ishikawa, H.-x. Liu, T. Taira, K.-i. Matsuda, T. Uemura, and M. Yamamoto. *Appl. Phys. Lett.*, 95:232512, 2009.

[14] M. P. Raphael, B. Ravel, Q. Huang, M. A. Willard, S. F. Cheng, B. N. Das, R. M. Stroud, K. M. Bussmann, J. H. Claessen, and V. G. Harris. *Phys. Rev. B*, 66:104429, 2002.

[15] W. H. Wang, M. Przybylski, W. Kuch, L. I. Chelaru, J. Wang, F. Lu, J. Barthel, H. L. Meyerheim, and J. Kirschner. *Phys. Rev. B*, 71:144416, 2005.

[16] Y. Sakuraba, M. Hattori, M. Oogane, Y. Ando, H. Kato, A. Sakuma, T. Miyazaki, and H. Kubota. *Appl. Phys. Lett.*, 88:192508, 2006.

[17] S. Tsunegi, Y. Sakuraba, M. Oogane, K. Takanashi, and Y. Ando. *Appl. Phys. Lett.*, 93:112506, 2008.

[18] P. J. Webster. *J. Phys. Chem. Solids*, 32:1221–1231, 1971.

[19] G. H. Fecher, H. C. Kandpal, S. Wurmehl, C. Felser, and G. Schönhense. *J. Appl. Phys.*, 99:08J106, 2006.

[20] P. K. Muduli, W. C. Rice, L. He, and F. Tsui. *J. Magn. Magn. Mater.*, 320(23):L141–L143, 2008.

[21] P. K. Muduli, W. Rice, C. L. He, B. A. Collins, Y. S. Chu, and F. Tsui. *J. Phys. Cond. Mat.*, 21:296005, 2009.

[22] G. H. Fecher, H. C. Kandpal, S. Wurmehl, J. Morais, H.-J. Lin, H.-J. Elmers, G. Schönhense, and C. Felser. *J. Phys. Condens. Matter*, 17:7237 – 7252, 2005.

[23] G. H. Fecher and C. Felser. *J. Phys. D: Appl. Phys.*, 40:1582 – 1586, 2007.

[24] T. Block, C. Felser, G. Jakob, J. Ensling, B. Mühling, P. Gütlich, V. Beaumont, F. Studer, and R. J. Cava. *J. Solid State Chem.*, 176:646 – 651, 2003.

[25] T. Block, S. Wurmehl, C. Felser, and J. Windeln. *Appl. Phys. Lett.*, 88:202504, 2006.

[26] K. Inomata, N. Tezuka, S. Okamura, H. Kurebayashi, and A. Hirohata. *J. Appl. Phys.*, 95:7234, 2004.

[27] K. Inomata, S. Okamura, A. Miyazaki, M. Kikuchi, N. Tezuka, M. Wojcik, and E. Jedryka. *J. Phys. D: Appl. Phys.*, 39:816 – 823, 2006.

[28] K. Inomata, M. Wojcik, E. Jedryka, N. Ikeda, and N. Tezuka. *Phys. Rev. B*, 77:214425, 2008.

[29] H. J. Elmers, S. Wurmehl, G. H. Fecher, G. Jakob, C. Felser, and G. Schönhense. *Appl. Phys. A*, 79:557 –563, 2004.

[30] H. J. Elmers, S. Wurmehl, G. H. Fecher, G. Jakob, C. Felser, and G. Schönhense. *J. Magn. Magn. Mater.*, 272-276:758 – 759, 2004.

[31] W. Jeitschko. *Metall. Mater. Trans. B*, 1:3159, 1970.

[32] H. C. Kandpal, C. Felser, and R. Seshadri. *J Phys. D: Appl. Phys.*, 39(5):776, 2006.

[33] J. Tobola, J. Pierre, S. Kaprzyk, R. V. Skolozdra, and M. A. Kouacou. *J. Phys.: Condens. Matter*, 10:1013 – 1032, 1998.

[34] J. Tobola and J. Pierre. *J. All. Comp.*, 296:243 – 252, 2000.

[35] R .A. de Groot, F. M. Müller, P. G. van Engen, and K. H. J. Buschow. *Phys. Rev. Lett.*, 50:2024, 1983.

[36] J. R. Sootsman, D. Y. Chung, and M. G. Kanatzidis. *Angew. Chem.*, 48(46):8616–8639, 2009.

[37] S. Ouardi, G. H. Fecher, B. Balke, M. Schwall, X. Kozina, G. Stryganyuk, C. Felser, E. Ikenaga, Y. Yamashita, S. Ueda, and K. Kobayashi. *Appl. Phys. Lett.*, 97:252113, 2010.

[38] X.L. Wang, X.S. Dou, and C. Zhang. *NPG Asia Mater.*, 2(1):31, 2010.

[39] S. Chadov, X. Qi, J. Kübler, G.H. Fecher, C. Felser, and S.C. Zhang. *Nat Mater*, 9(7):541–545, 2010.

[40] J. E. Moore. *Nature*, 464:194–198, 2010.

[41] D. M. Rowe. *Thermoelectrics Handbook: Macro to Nano*. CRC/Taylor & Francis, Boca Raton, fl edition, 2006.

[42] S. R. Clup, S. J. Poon, N. Hickman, T. M. Tritt, and J. Blumm. *Appl. Phys. Lett.*, 88(4):042106, 2006.

[43] D. Y. Jung, K. Kurosaki, C. E. Kim, H. Muta, and S. Yamanaka. *J. Alloys Compd.*, 489(2):328–331, 2010.

[44] F.J. DiSalvo. *Science*, 285:703, 1999.

[45] D. Nemir and J. Beck. *J. Electron. Mater.*, 39:1897, 2010.

[46] Xiao Yan, Giri Joshi, Weishu Liu, Yucheng Lan, Hui Wang, Sangyeop Lee, J. W. Simonson, S. J. Poon, T. M. Tritt, Gang Chen, and Z. F. Ren. *Nano Lett.*, 11(2):556–560, 2011.

[47] S. Sakurada and N. Shutoh. *Appl. Phys. Lett.*, 86(8):082105, 2005.

[48] S. Bhattacharya. *Phys. Rev. B*, 77(18):184203–184300, 2008.

[49] J. Yang, H. Li, T. Wu, W. Zhang, L. Chen, and J. Yang. *Adv. Funct. Mater.*, 18(19):2880–2888, 2008.

[50] K. Miyamoto, K. Kimura, K. Sakamoto, M. Ye, Y. Cui, K. Shimada, H. Namatame, M. Taniguchi, S. I. Fujimori, Y. Saitoh, E. Ikenaga, K. Kobayashi, J. Tadano, and T. Kanomata. *Appl. Phys. Expr.*, 1:081901, 2008.

[51] A. Einstein. *Ann. Phys.*, 17:549, 1905.

[52] I. Lindau, P. Pianetta, S. Doniach, and W. E. Spicer. *Nature*, 250:214, 1974.

[53] K. Kobayashi, M. Yabashi, Y. Takata, T. Tokushima, S. Shin, K. Tamasaku, D. Miwa, T. Ishikawa, H. Nohira, T. Hattori, Y. Sugita, O. Nakatsuka, A. Sakai, and S. Zaima. *Appl. Phys. Lett.*, 83:1005, 2003.

[54] K. Kobayashi. *Nucl. Instr. Meth. Phys. Res. A*, 601:32 – 47, 2009.

[55] C. Dallera, L. Duo, L. Braicovich, G. Panaccione, G. Paolicelli, B. Cowie, and J. Zegenhagen. *Appl. Phys. Lett.*, 85:4532, 2004.

[56] G. Panaccione, M. Sacchi, P. Torelli, F. Offid, G. Cautero, R. Sergo, A. Fondacaro, C. Henriquet, S. Huotari, G. Monacof, and L. Paolasini. *J. Electron Spectrosc. Relat. Phenom.*, 156-158:64 – 67, 2007.

[57] M. Ye, A. Kimura, Y. Miura, M. Shirai, Y. T. Cui, K. Shimada, H. Namatame, M. Taniguchi, S. Ueda, K. Kobayashi, R. Kainuma, T. Shishido, K. Fukushima, and T. Kanomata. *Phys. Rev. Lett.*, 104(17):176401, 2010.

[58] G. H. Fecher, B. Balke, A. Gloskowskii, S. Ouardi, C. Felser, T. Ishikawa, M. Yamamoto, Y. Yamashita, H. Yoshikawa, S. Ueda, and K. Kobayashi. *Appl. Phys. Lett.*, 92:193513, 2008.

[59] H. Sato, K. Shimada, M. Arita, Y. Takeda, M. Sawada, M. Nakatake, K. Yoshikawa, H. Namatame, Y. Takata, K. Kobayashi, E. Ikenaga, S. Shin, M. Yabashi, D. Miwa, Y. Nishino, K. Tamasaku, T. Ishikawa, K. Hiraoka, K. Kojima, and M. Taniguchi. *Physica B*, 351:298 – 300, 2004.

[60] V. V. Kuznetsov, N. A. Cherepkov, G. H. Fecher, and G. Schönhense. *J. Chem. Phys.*, 110:9997, 1999.

[61] G. Panaccione, G. Cautero, M. Cautero, A. Fondacaro, M. Grioni, P. Lacovig, G. Monaco, F. Offi, G. Paolicelli, M. Sacchi, N. Stojic, G. Stefani, R. Tommasini, and P. Torelli. *J. Phys.: Condens. Matter*, 17:2671 – 2679, 2005.

[62] A. Sekiyama, J. Yamaguchi, A. Higashia, M. Obara, H. Sugiyama, M. Y. Kimura, S. Suga, S. Imada, I. A. Nekrasov, M. Yabashi, K. Tamasaku, and T. Ishikawa. *New Journal of Physics*, 12:043045, 2010.

[63] I. Vartanyants, T.-L. Lee, S. Thiess, and J. Zegenhagen. *Nucl. Instrum. Methods Phys. Res. A*, 547:196 – 207, 2005.

[64] S. Döring, F. Schönbohm, U. Berges, R. Schreiber, D. E. Bürgler, C. M. Schneider, M. Gorgoi, F. Schäfers, C. Papp, B. Balke, C. S. Fadley, and C. Westphal. *Phys. Rev. B*, 83(16):165444, 2011.

[65] K. Kobayashi. *Nucl. Instr. Meth. Phys. Res. A*, 547:98 – 112, 2005.

[66] B. Balke, G. H. Fecher, H. C. Kandpal, C. Felser, K. Kobayashi, E. Ikenaga, J.-J. Kim, and S. Ueda. *Phys. Rev. B*, 74:104405, 2006.

[67] G. H. Fecher, B. Balke, S. Ouardi, C. Felser, G. Schönhense, E. Ikenaga, J. J Kim, S. Ueda, and K. Kobayashi. *J. Phys. D: Appl. Phys.*, 40:1576, 2007.

[68] S. Ouardi, B. Balke, A. Gloskovskii, G. H. Fecher, C. Felser, G. Schnhense, T. Ishikawa, T. Uemura, M. Yamamoto, H. Sukegawa, W. Wang, K. Inomata, Y. Yamashita, H.Yoshikawa, S. Ueda, and K. Kobayashi. *J Phys. D: Appl. Phys.*, 42:084010, 2009.

[69] S. Ouardi, A. Gloskovskii, B. Balke, C. A. Jenkins, J. Barth, G. H. Fecher, C. Felser, M. Gorgoi, M. Mertin, F. Schfers, E. Ikenaga, K. Yang, K. Kobayashi, T. Kubota, Oogane, M., and Y. Ando. *J Phys. D*, 42:084011, 2009.

[70] S. Tanuma, C. J. Powell, and D. R. Penn. *Surf. Interf. Anal.*, 21:165, 1993.

[71] A. Oelsner, G. H. Fecher, Ch. Ostertag, Th. Jentzsch, and G. Schönhense. *Surf. Sci.*, 331-333:349 – 354, 1995.

[72] T. Matsushita, S. Imada, H. Daimon, T. Okuda, K. Yamaguchi, H. Miyagi, and S. Suga. *Phys. Rev. B*, 56:7687, 1997.

[73] G. H. Fecher, A. Oelsner, M. Schicketanz, and G. Schönhense. *J. Electron Spectrosc. Relat. Phenom.*, 88-91:185 – 190, 1998.

[74] A. Oelsner, G. H. Fecher, M. Schicketanz, and G. Schönhense. *Surf. Sci.*, 433435:5357, 1999.

[75] N. A. Cherepkov and G. Schönhense. *Europhys. Lett.*, 24:79, 1993.

[76] R. J. Smith, J. Anderson, and G. J. Lapeyre. *Phys. Rev. Lett.*, 37:1081, 1976.

[77] N. M. Kabachnik. *J. Electron Spectrosc. Relat. Phenom.*, 79:269 – 274, 1996.

[78] N. A. Cherepkov and G. Raseev. *J. Chem. Phys.*, 103:8238, 1995.

[79] Ch. Ostertag, J. Bansmann, Ch. Grünewald, Th. Jentzsch, A. Oelsner, G. H. Fecher, and G. Schönhense. *Surf. Sci.*, 331-333:1197 – 1202, 1995.

[80] C. S. Fadley. *Nucl. Instrum. Methods Phys. Res. A*, 647:24 – 41, 2005.

[81] J. Cooper and R. N. Zare. *J. Chem. Phys.*, 48:942, 1968.

[82] M. Born and E. Wolf. *Electromagnetic Theory of Propagation, Interference, and Diffraction of Light*, volume 7th Ed. of *Principles of Optics*. Cambridge University Press, Cambridge, UK, 2000.

[83] B. Ritchie. *Phys. Rev. A*, 12:567, 1975.

[84] N. A. Cherepkov and V. V. Kuznetsov. *Z. Phys. D*, 7(3):271, 1987.

[85] V. V. Kuznetsov, N. A. Cherepkov, G. H. Fecher, and G. Schönhense. *J. Chem. Phys.*, 117:7180, 2002.

[86] N.A. Cherepkov, V.V. Kuznetsov, and V.A. Verbitskii. *J. Phys. B: At. Mol. Opt. Phys.*, 28:1221 – 1239, 1995.

[87] B. Norden. *Appl. Spectr. Rev.*, 14(2):158–248, 1978.

[88] Ch. Roth, F. U. Hillebrecht, H. B. Rose, and E. Kisker. *Phys. Rev. Lett.*, 70:3479, 1993.

[89] H. Ebert. Fully relativistic band structure calculations for magnetic solids formalism and application. In H. Dreysee, editor, *Electronic Structure and Physical Properties of Solids. The Use of the LMTO Method*, volume 535, pages 191–246. Springer-Verlag, Berlin, Heidelberg, 1999.

[90] F. Salvat and R. Mayol. *Comp. Phys. Commun.*, 62:65.

[91] F. Salvat and R. Mayol. *Comp. Phys. Commun.*, 74:358.

[92] J.J. Yeh and I. Lindau. *Atom. Data Nucl. Data*, 32:1–155, 1985.

[93] M.B. Trzhaskovoskaya, Nefedov. V.I., and V.G. Yarzhemsky. *Atom Data Nucl Data*, 77:97, 2001.

[94] M.B. Trzhaskovoskaya, Nefedov. V.I., and V.G. Yarzhemsky. *Atom Data Nucl Data*, 82:257, 2002.

[95] D. A. Shirley. *Phys. Rev. B*, 5(12):4709–4714, 1972.

[96] S. Suga, A. Sekiyama, H. Fujiwara, Y. Nakatsu, T. Miyamachi, S. Imada, P. Baltzer, S. Niitaka, H. Takagi, K. Yoshimura, M. Yabashi, K. Tamasaku, A. Higashiya, and T. Ishikawa. *N. J. Phys.*, 11:073025, 2009.

[97] J. W. Cooper. *Phys. Rev. A*, 42:6942, 1990.

[98] G. H. Fecher, V. V. Kuznetsov, N. A. Cherepkov, and G. Schönhense. *J. Electron Spectrosc. Relat. Phenom.*, 122:157, 2002.

[99] W. Eberhardt and F. J. Himpsel. *Phys. Rev. B*, 21:5572, 1980.

[100] G. Borstel, M. Neumann, and M. Wöhlecke. *Phys. Rev. B*, 23:3121, 1981.

[101] S. L. Altmann and A. P. Cracknell. *Rev. Mod. Phys.*, 37:19, 1965.

[102] Z. Hussain, E. Umbach, J. J. Barton, J. G. Tobin, and D. A. Shirley. *Phys. Rev. B*, 25:672, 1982.

[103] P. Blaha, K. Schwarz, G. K. H. Madsen, D. Kvasnicka, and J. Luitz. *WIEN2k, An Augmented Plane Wave + Local Orbitals Program for Calculating Crystal Properties.* Karlheinz Schwarz, Techn. Universitt Wien, Wien, Austria, 2001.

[104] G. K. H. Madsen and D. J. Singh. *Comput. Phys. Commun.*, 175(1):67–71, 2006.

[105] T. Graf, G. H. Fecher, J. Barth, J. Winterlik, and C. Felser. *J. Phys. D: Appl. Phys.*, 42:084003, 2009.

[106] J. Barth, G. H. Fecher, B. Balke, S. Ouardi, T. Graf, C. Felser, A. Shkabko, A. Weidenkaff, P. Klaer, H. J. Elmers, H. Yoshikawa, S. Ueda, and K. Kobayashi. *Phys. Rev. B*, 81:064404, 2010.

[107] J. P. Perdew, K. Burke, and M. Ernzerhof. *Phys. Rev. Lett.*, 77:3865, 1996.

[108] H. Ebert, D. Ködderitzsch, and Minar. *Rep. Prog. Phys*, 74(9):096501, 2011.

[109] P. Weinberger. *Electron Scattering Theory for Ordered and Disordered Matter.* Clarendon Press, Oxford, 1990.

[110] W. H. Butler. *Phys. Rev. B*, 31:3260, 1985.

[111] J. P. Perdew, A. Ruzsinszky, L. A. Constantin, J. Sun, and G. I. Csonka. *J. Chem. Theory Comput.*, 5:902, 2009.

[112] E. Engel and S. H. Vosko. *Phys. Rev. B*, 47:13164, 1993.

[113] A. D. Becke. *J. Chem. Phys.*, 98:5648, 1993.

[114] J. P. Perdew and Y. Wang. *Phys. Rev. B*, 45:13244, 1992.

[115] J. P. Perdew, A. Ruzsinszky, G. I. Csonka, O. A. Vydrov, G. E. Scuseria, L. A. Constantin, X. Zhou, and K. Burke. *Phys. Rev. Lett.*, 100:136406, 2008.

[116] F. D. Murnaghan. *Proc. Natl. Acad. Sci. U. S. A.*, 30(9):244247, 1944.

[117] F. Birch. *J. Geophys. Res.*, 57:227–286, 1952.

[118] M. Born and K. Huang. *Dynamical Theory of Crystal Lattices.* Clarendon Press, Oxford, 1956.

[119] J. F. Nye. *Physical Properties of Crystals.* Oxford Science Publications, Oxford, 1985.

[120] J. Wang, S. Vip, S. R. Phillpot, and D. Wolf. *Phys. Rev. Lett.*, 71:4182, 1993.

[121] K. Parlinski, Z. Q. Li, and Y. Kawazoe. *Phys. Rev. Lett.*, 78:4063–4066, 1997.

[122] F. F. Ferreira, E. Granado, W. Carvalho, S. W. Kycia, D. Bruno, and R. Droppa. *J. Synchrotron Rad.*, 13:46, 2006.

[123] H. C. N. Tolentino, A. Y. Ramos, M. C. M. Alves, R. A. Barrea, E. Tamura, J. C. Cezar, and N. Watanabe. *J. Synchrotron Rad.*, 8(3):1040–1046, 2001.

[124] S. Ueda, Y. Katsuya, M. Tanaka, H. Yoshikawa, Y. Yamashita, S. Ishimaru, Y. Matsushita, and K. Kobayashi. *AIP Conf. Proc.*, 1234(1):403–406, 2010.

[125] M. Suzuki, N. Kawamura, M. Mizukami, A. Urata, H. Maruyama, S. Goto, and T. Ishikawa. *Jpn. J. Appl. Phys.*, 37:L1488, 1998.

[126] T. Graf, C. Felser, and S. S. P. Parkin. *Prog. Solid State Chem.*, 39(1):1–50, 2011.

[127] T. Ambrose, J.J. Krebs, and G.A. Prinz. *Appl. Phys. Lett.*, 76(22):3280, 2000.

[128] T. Ishikawa, T. Marukame, K. i Matsuda, T. Uemura, M. Arita, and M. Yamamoto. *J. Appl. Phys.*, 99(3):08J110, 2006.

[129] S. Hakamata, T. Ishikawa, T. Marukame, K. i Matsuda, T. Uemura, M. Arita, and M. Yamamoto. *J. Appl. Phys.*, 101(2):09J513, 2007.

[130] D. T. Cromer. *J. Appl. Cryst.*, 16:437, 1983.

[131] W. Kraus and G. Nolze. *J. Appl. Cryst.*, 29:301–303, 1996.

[132] J. Laugier and B. Bochu. http://www.ccp14.ac.uk/tutorial/lmgp/scatfac.htm.

[133] D. Koningsberger and R. Prins. *X-ray Absorption: Principles, applications and techniques of EXAFS, SEXAFS and XANES in Chemical Analysis, Chemical Analysis.*, volume 92. John Wiley & Sons: New York, 1988.

[134] M. Newville. *J. Synchrotron Rad.*, 8(2):322, 2001.

[135] S. I. Zabinsky, J. J. Rehr, A. Ankudinov, R. C. Albers, and M. J. Eller. *Phys. Rev. B*, 52(4):2995, 1995.

[136] I. Galanakis and P.H. Dederichs. *Phys. Rev. B*, 66:174429, 2002.

[137] K. Miyamoto, K. Iori, A. Kimura, T. Xie, M. Taniguchi, S. Qiao, and K. Tsuchiya. *Solid State Commun.*, 128(5):163–166, 2003.

[138] K. Miyamoto, A. Kimura, K. Iori, K. Sakamoto, T. Xie, T. Moko, S. Qiao, M. Taniguchi, and K. Tsuchiya. *J. Phys.: Condens. Matter*, 16(48):5797–S5800, 2004.

[139] V. N. Antonov, O. Jepsen, A. N. Yaresko, and A. P. Shpak. *J. Appl. Phys.*, 100(4):043711, 2006.

[140] P. Klaer, T. Bos, M. Kallmayer, C. G. F. Blum, T. Graf, J. Barth, B. Balke, G. H. Fecher, C. Felser, and H. J. Elmers. *Phys. Rev. B*, 82:104410, 2010.

[141] C. S. Fadley and D. A. Shirly. *Phys. Rev. A*, 2:1109, 1970.

[142] R. D. Cowan. *The Theory of Atomic Structure and Spectra*. California Press, Berkeley, 1981.

[143] G. van der Laan. *J. Phys.: Condens. Matter*, 3(38):7443, 1991.

[144] F. de Groot. *Coordin. Chem. Rev.*, 249:31, 2005.

[145] F. de Groot and A. Kotani. *Core Level Spectroscopy of Solids*. CRC Press, 2008.

[146] P. S. Bagus, R. Broer, de Jong W. A., and W. C. Nieuwpoort. *Phys. Rev. Lett.*, 84:2259, 2000.

[147] E. Stavitski and F. M. F. de Groot. *Micron*, 41(7):687–694, 2010.

[148] R. G. Cavell, S. P. Kowalczyk, L. Ley, R. A. Pollak, B. Mills, D. A. Shirley, and W. Perry. *Phys. Rev. B*, 7(12):5313, 1973.

[149] P. S. Wehner, J. Stöhr, G. Apai, F. R. Mc Feely, R. S. Williams, and D. A. Shirley. *Phys. Rev. B*, 14(6):2411, 1976.

[150] O. L. Anderson. *J. Phys. Chem. Solids*, 24:909 – 917, 1963.

[151] G. Chin. *Trans. Am. Cryst. Assoc.*, 11:1, 1975.

[152] J. J. Gilman. *Hardness - A Strength Microprobe*. The Science of Hardness Testing and Its Research Applications. Amer. Soc. Metals , Metals Park, Ohio, 1973.

[153] John J. Gilman. *Chemistry and physics of mechanical hardness*. Wiley, Hoboken, NJ, 2009.

[154] D. Tabor. *The Hardness of Metals*. Clarendon Press, Oxford, UK, 1951.

[155] J. L. F. Fraga, D. E. Brandao, and J. G. Sereni. *J. Magn. Magn. Mater.*, 102:199–207, 1991.

[156] E. Sevillano, H. Meuth, and J. J. Rehr. *Phys. Rev. B*, 20(12):4980, 1979.

[157] M. J. Otto, R. A. M. van Woerden, P. J. van der Valk, J. Wijngaard, C.F. van Bruggen, and C. Haas. *J. Phys. Cond. Mat.*, 1(13):2351, 1989.

[158] C. G. F. Blum, C. A. Jenkins, J. Barth, C. Felser, S. Wurmehl, G. Friemel, C. Hess, G. Behr, B. B"chner, A. Reller, S. Riegg, S. G. Ebbinghaus, T. Ellis, P. J. Jacobs, J. T. Kohlhepp, and H. J. M. Swagten. *Appl. Phys. Lett.*, 95:161903, 2009.

[159] B. Balke, S. Ouardi, T. Graf, J. Barth, C. G. F. Blum, G. H. Fecher, A. Shkabko, A. Weidenkaff, and C. Felser. *Solid State Commun.*, 150(11-12):529–532, 2010.

[160] J. M. Ziman. *Electrons and Phonons*. Oxford University Press, Oxford, 1960.

[161] Y. Kimura, H. Ueno, and Y. Mishima. *J. Electron. Mater.*, 38(7):934–939, 2009.

[162] N. Shutoh and S. Sakurada. *J. Alloys Compd.*, 389(1-2):204–208, 2005.

[163] T. Katayama, S. W. Kim, Y. Kimura, and Y. Mishima. *J. Electron. Mater.*, 32(11):1160–1165, 2003.

[164] Q. Shen, L. Chen, T. Goto, T. Hirai, J. Yang, G. P. Meisner, and C. Uher. *Appl. Phys. Lett.*, 79(25):4165–4167, 2001.

[165] J. Yang, G. P. Meisner, and L. Chen. *Appl. Phys. Lett.*, 85(7):1140–1142, 2004.

[166] S. Katsuyama, R. Matsuo, and M. Ito. *J. Alloys Compd.*, 428(1-2):262–267, 2007.

[167] T. Wu, W. Jiang, X. Li, S. Bai, S. Liufu, and L. Chen. *J. Alloys Compd.*, 467(1-2):590–594, 2009.

[168] S. R. Culp, W. J. Simonson, S. J. Poon, V. Ponnambalam, J. Edwards, and T.M. Tritt. *Appl. Phys. Lett.*, 93(4):022105, 2008.

[169] A. Horyn, O. Bodak, L. Romaka, Y. Gorelenko, A. Tkachuk, V. Davydov, and Y. Stadnyk. *J. Alloys Compd.*, 363:10–14, 2004.

[170] L. L. Wang. *J Phys. D: Appl. Phys.*, 105(1):013709, 2009.

[171] M. Onoue, F. Isshii, and T. Oguchi. *J. Phys. Soc. Jpn.*, 77:054706, 2008.

[172] K. Kroth, B. Balke, G. H. Fecher, V. Ksenofontov, C. Felser, and H. J Lin. *Appl. Phys. Lett.*, 89:202509, 2006.

[173] B. Balke, G. H. Fecher, A. Gloskovskii, J. Barth, K. Kroth, C. Felser, R. Robert, and A. Weidenkaff. *Phys. Rev. B*, 77:045209, 2008.

[174] J. Pierre. *J. Magn. Magn. Mater*, 134(1):95, 1994.

[175] L. Romaka, Y. Stadnyk, A. Horyn, M.G. Shelyapina, V.S. Kasperovich, D. Fruchart, E.K. Hlil, and P. Wolfers. *J. Alloys Compd.*, 396(1-2):64–68, 2005.

[176] T. Stopa. *J. Phys. Condens. Matter*, 18(27):6379–6390, 2006.

[177] L. Chaput, J. Tobola, P. Pecheur, and H. Scherrer. *Phys. Rev. B*, 73:045121, 2006.

[178] V. Romaka, M. Shelyapina, Yu Gorelenko, D. Fruchart, Yu Stadnyk, L. Romaka, and V. Chekurin. *Semiconductors*, 40(6):655–661, 2006.

[179] W. J. Simonson and S. J. Poon. *J. Phys.: Condens. Matter*, 20:255220, 2008.

[180] M. Schwall and B. Balke. *Appl. Phys. Lett.*, 98:042106, 2011.

[181] M. A. Kouacou, J. Pierre, and R. V. Skolozdra. *J. Phys.: Condens. Matter*, 7:7373 – 7385, 1995.

[182] J. Pierre, R. V. Skolozdra, J. Tobola, S. Kaprzyk, C. Hordequin, M. A. Kouacou, I. Karla, R. Currat, and E. Lelievre-Berna. *J. All. Comp.*, 262-263:101 – 107, 1997.

[183] L. P. Romaka, M. G. Shelyapina, Y. V. Stadnyk, D. Fruchart, E. K. Hlil, and V. A. Romaka. *J. All. Comp.*, 416:46 – 50, 2006.

[184] G. H. Fecher, A. Gloskovskii, K. Kroth, J. Barth, B. Balke, C. Felser, F. Schäfers, M. Mertin, W. Eberhardt, S. Mähl, and O. Schaff. *J. Electron Spectrosc. Relat. Phenom.*, 156-158:97 – 101, 2007.

[185] P. Amornpitoksuk and S. Suwanboon. *J. All. Comp.*, 462:267, 2008.

[186] J. Tobola, L. Jodin, P. Pecheur, and G. Venturini. *J. Alloys Compd.*, 383(1-2):328–333, 2004.

[187] T. Sekimoto, K. Kurosaki, H. Muta, and S. Yamanaka. *J. All. Comp.*, 394:122 – 125, 2005.

[188] V. A. Romaka, Y. V. Stadnyk, P. Rogl, L.G. Akselrud, V.N. Davydov, V.V. Romaka, Y.K. Gorelenko, and A.M. Horyn. *Ukr. J. Phys.*, 53(2):157, 2008.

[189] C. S. Lue, C. F. Chen, F.-K. Chiang, and M.-W. Chu. *Phys. Rev. B*, 80:174202, 2009.

[190] B. Balke, K. Kroth, G. H. Fecher, and C. Felser. *J. Appl. Phys.*, 103:07D115, 2008.

[191] Y. Xia, V. Ponnambalam, S. Bhattacharya, A. L. Pope, S. J. Poon, and T. M. Tritt. *J. Phys.: Condens. Matter*, 13:77 – 89, 2001.

[192] Y. Kawaharada, K. Kurosaki, H. Muta, M. Uno, and S. Yamanaka. *J. All. Comp.*, 384:308 – 311, 2004.

[193] N. Tareuchi, K. Gosho, M. Hiroi, and M. Kawakami. *Physica B*, 359 - 361:1183 – 1185, 2005.

[194] T. Sekimoto, K. Kurosaki, H. Muta, and S. Yamanaka. *J. Alloys Compd.*, 407(1-2):326–329, 2006.

[195] T. Sekimoto, K. Kurasaki, H. Muta, and S. Yamanaka. *Jpn. J. Appl. Phys.*, 46:L673, 2007.

[196] T. Wu, W. Jiang, X. Li, Y. Zhou, and L. Chen. *J. Appl. Phys.*, 102:103705, 2007.

[197] M. Zhou, L. Chen, C. Feng, D. Wang, and J.-F. Li. *J. Appl. Phys.*, 101:113714, 2007.

[198] P. Qiu, X. Huang, X. Chen, and L. Chen. *J. Appl. Phys.*, 106:103703, 2009.

[199] B. Balke, J. Barth, M. Schwall, G. H. Fecher, and C. Felser. *J. Electron Mater*, 40:702, 2011.

[200] F. G. Aliev. *Physica B*, 171:199, 1991.

[201] S. Ouardi, G. H. Fecher, C. Felser, J. Hamrle, K. Postava, and J. Pistora. *Appl. Phys. Lett.*, 99:211904, 2011.

[202] S. Ouardi, G. H. Fecher, B. Balke, A. Beleanu, X. Kozina, G. Stryganyuk, C. Felser, W. Kloss, H. Schrader, F. Bernardi, J. Morais, E. Ikenaga, Y. Yamashita, S. Ueda, and K. Kobayashi. *Phys. Rev. B*, 84:155122, 2011.

[203] B. Kong, X. R. Chen, J. X. Yu, and C. L. Cai. *J. All. Comp.*, 509(5):2611–2616, 2011.

[204] B. Kong, B. Zhu, Y. Cheng, L. Zhang, Q. X. Zeng, and X. W. Sun. *Physica B*, 406:3003–3010, 2011.

[205] G. K. H. Madsen and D. J. Singh. *Comp. Phys. Comm.*, 175:67, 2006.

[206] R. Brendel and D. Bormann. *J. Appl. Phys.*, 71:1, 1992.

[207] S. Ouardi, G. H. Fecher, C. Felser, C. F. G. Blum, D. Bombor, C. Hess, S. Wurmehl, B. Büchner, and E. Ikenaga. *Appl. Phys. Lett.*, 99:152112, 2011.

[208] S. Ouardi, C. Shekhar, G. H. Fecher, X. Kozina, G. Stryganyuk, C. Felser, S. Ueda, and K. Kobayashi. *Appl. Phys. Lett.*, 98(21):211901, 2011.

[209] N. F. Mott and H. Jones. *The Theory of the Properties of Metals and Alloys.* Clarendon Press, Oxford, 1936.

[210] M. G. Haase, T. Schmidt, C. G. Richter, H. Block, and W. Jeitschko. *J. Solid State Chem.*, 168(1):18, 2002.

[211] T. Harmening, H. Eckert, and R. Pöttgen. *Solid State Sci.*, 11(4):900–906, 2009.

[212] P. C. Canfield, J. D. Thompson, W. P. Beyermann, A. Lacerda, M. F. Hundley, E. Peterson, , Z. Fisk, and H. R. Ott. *J. Appl. Phys.*, 70:5800, 1991.

[213] Y. Bando, T. Suemitsu, K. Takagi, H. Tokushima, Y. Echizen, K. Katoh, K. Umeo, Y. Maedab, and T. Takabatakeb. *J. Alloy Compd.*, 313:1, 2000.

[214] S. K. Malik and D. T. Adroja. *J. Magn. Magn. Mat.*, 102(1-2):42–46, 1991.

[215] G. Goll, M. Marz, A. Hamann, T. Tomanic, K. Grube, T. Yoshino, and T. Takabatake. *Physica B*, 403(5-9):1065–1067, 2008.

[216] M. H. Jung, T. Yoshino, S. Kawasaki, T. Pietrus, Y. Bando, T. Suemitsu, M. Sera, , and T. Takabatake. *J. Appl. Phys.*, 89:7631, 2001.

[217] K. Gofryk, D. Kaczorowski, T. Plackowski, A. Leithe-Jasper, and Y. Grin. *Phys. Rev. B*, 84:035208, 2011.

[218] D. Xiao, Y. Yao, W. Feng, J. Wen, W. Zhu, X.-Q. Chen, G. M. Stocks, and Z. Zhang. *Phys. Rev. Let.*, 105(9):096404, 2010.

[219] Y. Xia, D. Qian, D. Hsieh, L. Wray, A. Pal, H. Lin, A. Bansil, D. Grauer, Y. S. Hor, R. J. Cava, and M. Z. Hasan. *Nat. Phys.*, 5:398, 2009.

[220] W. Al-Sawai, Hsin Lin, R. S. Markiewicz, L. A. Wray, Y. Xia, S. Y. Xu, M. Z. Hasan, and A. Bansil. *Phys. Rev. B*, 82(12):125208, 2010.

[221] H. Lin, L. A. Wray, Y. Xia, S. Xu, S. Jia, R. J. Cava, A. Bansil, and M. Z. Hasan. *Nat Mater*, 9(7):546–549, 2010.

[222] H. Okamura, J. Kawahara, T. Nanba, S. Kimura, K. Soda, U. Mizutani, Y. Nishino, M. Kato, I. Shimoyama, H. Miura, K. Fukui, K. Nakagawa, H. Nakagawa, and T. Kinoshita. 84(16):3674, 2000.

[223] B. Xu and L. Yi. *J.Phys. D.: Appl. Phys.*, 41:095404, 2008.

[224] J. Oestreich, U. Probst, F. Richardt, , and E Bucher. *J. Phys.: Condens. Matter*, 15:635, 2003.

[225] X. L. Wang. *Phys. Rev. Lett.*, 100(15):156404, 2008.

[226] K. Gofryk, D. Kaczorowski, T. Plackowski, J. Mucha, A. Leithe-Jasper, W. Schnelle, and Yu Grin. *Phys. Rev. B*, 75(22):224426, 2007.

[227] I. M. Tsidilkovski. *Electron Spectrum of Gapless Semiconductors*, volume 116 of *Springer Series in Solid-State Sciences*. Springer, 1996.

[228] K. Siegbahn. *Nucl. Instrum. Methods Phys. Res. A*, 547:2005, 2005.

[229] N. Chandra. *J. Phys. B: At. Mol. Phys.*, 20:3417, 1987.

[230] O. Hemmers, R. Guillemin, and D. W. Lindle. *Rad. Phys. Chem.*, 70:123, 2004.